



UNIVERSITY OF
BIRMINGHAM

**Thermophoretic manipulation of the
mechanical properties of biomaterials in
microfluidics**

by

Alexandros Kosmidis-Papadimitriou

*A thesis submitted to the University of Birmingham for the degree of
DOCTOR OF PHILOSOPHY*

School of Chemical engineering

College of Engineering and Physical Sciences

University of Birmingham

August 2020

UNIVERSITY OF
BIRMINGHAM

University of Birmingham Research Archive

e-theses repository

This unpublished thesis/dissertation is copyright of the author and/or third parties. The intellectual property rights of the author or third parties in respect of this work are as defined by The Copyright Designs and Patents Act 1988 or as modified by any successor legislation.

Any use made of information contained in this thesis/dissertation must be in accordance with that legislation and must be properly acknowledged. Further distribution or reproduction in any format is prohibited without the permission of the copyright holder.

Abstract

The optimization of cell-substrate and cell-cell interactions is a central objective in tissue engineering applications. There is great potential to modulate and improve such interactions using extra cellular matrices that exhibit a gradient of mechanical properties that mimic accurately the in vivo tissue microenvironment and modulate cell behavior especially at the microscale. Here we show that by applying temperature gradients across a microfluidic channel and exploiting thermophoretic transport effects, it is possible to fabricate biocompatible hydrogels with controllable stiffness and porosity gradients. The elasticity of the hydrogels was evaluated locally by Atomic Force Microscopy revealing values between 20-100 kPa. The hydrogel microstructure was investigated by Scanning Electron Microscopy after supercritical drying and confirms the concentration gradient induced by thermophoresis. Moreover, we show that the stiffness gradient of the biomaterials can be effectively modulated by regulating the temperature difference across the microfluidic device and altering the concentration of gellan gum. Furthermore, the proliferation and level of mineralization of MC3T3 osteoblasts, seeded on the surface of the biomaterial, was monitored over time at different stiffness areas and time points, using live/dead assays and X-Ray Fluorescence technique. Cells show a preferential migration and proliferation towards the stiffer side where they also produce a higher mineralization (i.e., phosphorus and calcium deposits). Taken together, these results establish a new route to controlling the microstructure of cell culture matrices.

Acknowledgements

The work presented in this thesis was carried out and internally funded by the School of Chemical Engineering at the University of Birmingham.

At first, I would like to thank my supervisor Dr. Daniele Vigolo, who provided guidance to my research project and helped me to develop my communication and academic writing skills. He was more of a friend to me than just a PI to my project, who always had time to help me. I wish him all the best and to always be happy with his family.

I would also like to thank my co-supervisor Prof. Liam Grover who gave us valuable feedback on the generated results and his point of view as an expert on biomaterials. He also granted us access to the Biochemical engineering department and later to the Healthcare Technologies Institute for conducting all the biological experiments. He really helped us tackle a lot of issues with the cell cultures and the presentation of data to a more bio-related audience.

Secondly, I would like to thank all three master students, Rowan Liddle, Wenbin Shi and Hanzhen Xu, who worked hard to produce valuable results that were presented both in this thesis and their master dissertation. I wish them all the best on their career.

Furthermore, I want to acknowledge the SEM and supercritical drying work on the fibers that was conducted by Dr. Yi Shen at the Department of Chemistry of the University of Cambridge. I want to thank her for her contribution to both the experimental work and the writing of a publication based on this research project.

I would like to acknowledge past and present members of the Vigolo group for their advices, trainings and of course for their humor during the meetings and the long lab experiment sessions.

On a personal note, I want to thank my partner Zoi who endured my concerns and gave me the courage to move on during those 3.5 years. In addition, a big thanks to my closest friends Alberto, (A)Ioannis, Erick and Luis. We supported each other during our PhD and had so much fun the past few years.

Finally, my warm thanks goes to my family and my parents who supported me and encouraged me to begin this wonderful journey from Greece to the UK which was full of life experiences and happy moments that I shall remember for a lifetime.

CONTENTS

INTRODUCTION.....	1
LITERATURE REVIEW	3
EXTRACELLULAR MATRIX (ECM).....	3
TISSUE ENGINEERING	5
RECENT ADVANCES IN TISSUE ENGINEERING	7
HYDROGELS	9
GRADIENT ECMS.....	11
CONTEMPORARY STRATEGIES OF ECM FABRICATION	15
GELLAN GUM	16
SODIUM ALGINATE	19
MICROFLUIDIC FABRICATION	21
THERMOPHORESIS	26
TECHNIQUES.....	32
MICROFLUIDIC DEVICE FABRICATION.....	32
ATOMIC FORCE MICROSCOPY (AFM).....	37
SCANNING ELECTRON MICROSCOPY (SEM)	40
MICRO-COMPRESSION RIG.....	42
CONFOCAL LASER SCANNING MICROSCOPY (CLSM).....	44
X-RAY FLUORESCENCE (XRF).....	45
MATERIALS AND METHODS	49
MATERIALS.....	49
PROTOCOLS.....	50
1. <i>Device fabrication</i>	50
2. <i>Biomaterial fabrication process</i>	57
A. Gellan gum	57
B. Sodium Alginate.....	61
3. <i>Material storage</i>	63
MATERIAL CHARACTERIZATION	65
1. <i>Atomic force microscopy (AFM)</i>	65
A. Cantilever selection	65

B. Young's Modulus evaluation.....	67
2. <i>Scanning electron microscopy (SEM)</i>	72
A. Sample preparation.....	72
B. Supercritical CO ₂ and SEM imaging.....	73
BIOLOGICAL EXPERIMENTS	74
1. <i>Mammalian cell cultures</i>	74
A. Cell culture preparation	74
B. Cell counting and splitting.....	76
C. Cell storage.....	78
D. Material Preparation and seeding	79
2. <i>Live dead assay</i>	81
A. Osteogenic cell culture medium preparation	81
3. <i>X-ray Fluorescence (XRF)</i>	82
RESULTS	84
SODIUM ALGINATE EXPERIMENTS.....	84
1. <i>Microfluidic setup</i>	84
2. <i>Preliminary results</i>	89
GELLAN GUM EXPERIMENTS.....	95
1. <i>Microfluidic setup</i>	95
2. <i>Preliminary results</i>	100
3. <i>Main results</i>	104
SEM IMAGING.....	106
1. <i>Material preparation</i>	107
2. <i>SEM measurements</i>	108
MANIPULATION OF THE MECHANICAL PROPERTIES.....	111
1. <i>Effect of GG concentration</i>	111
2. <i>Effect of temperature gradient</i>	113
3. <i>Effect of residence time</i>	115
4. <i>Reproducibility of the method</i>	117
EXPLORING A NEW TYPE OF GRADIENT.....	119
BIOLOGICAL EXPERIMENTS	122
1. <i>Material sterilization</i>	125
2. <i>Biocompatibility optimization</i>	128

3. <i>MC3T3 cell cultures in vitro.</i>	132
A. Cell seeding density.....	133
B. Live/dead staining.....	136
C. Cell migration.....	139
D. Cell behavior over time	141
BIO-FUNCTIONALITY OF MC3T3S.....	143
1. <i>XRF experiments</i>	145
A. 15 days of culture	147
B. 30 days of culture	150
CONCLUSIONS	153
FUTURE WORK	158
REFERENCES	161

Table of Figures

<i>Figure 1: Matrix elasticity effect on cell behavior, Cell morphology, proliferation, spreading and adhesion increase as matrix stiffness increases.</i> ^[52]	8
<i>Figure 2: Cell movement mechanism through the extension of lamellipodia, adhesion with the substrate (focal adhesions), translocation of the cell body and de-adhesion of the local focal adhesions previously created.</i> ^[94]	13
<i>Figure 3: Suitable matrix stiffness range for different cell type families, from softer brain tissue to stiffer muscle and bone tissues ranging from 0.1 to 100 kPa.</i> ^[100]	14
<i>Figure 4: Low acyl gellan gum chemical structure.</i> ^[116]	17
<i>Figure 5: Chemical formula of: a) mannuronic (M) and guluronic (G) alginate monomers, b) blocks of single or alternating M and G residues.</i> ^[123, 124]	19
<i>Figure 6: a) 3-D schematic of the pattern stamp created at the microfluidic device, b) fluorescent image of two types of patterned cells, Human bladder cancer cells (ECVs) labelled in green with 5-chloromethylfluorescein diacetate (CMFDA) and Bovine adrenal capillary endothelial cells (BCEs) labelled in red using DiI-conjugated acetylated low density lipoprotein. c) and d) phase contrast images of the two different cell types that were patterned.</i> ^[144]	23
<i>Figure 7: a) Picture of the microfluidic chip used by Berejnov et al. (scale bar of 15 mm) to study multiphase transport through porous media, b) Network of channels (pores) developed at the middle of the microfluidic channel with width varying from 10 to 80 μm to better understand how multiphase flows diffuse through the pore-network.</i>	25
<i>Figure 8: a) Schematic of the PDMS microfluidic device exhibiting an array of channels used for the generation of gradients, b) schematic of a microfluidic gradient generator. Different fluid streams are introduced from the top inlets, then mixed and recombined to a concentration gradient at the outlet channel.</i> ^[160]	26
<i>Figure 9: a) Schematic of a microfluidic device that induces a temperature gradient by flowing hot and cold water to the side channels, b) alternative design using a silver-epoxy resistive Joule heater for the hot channel, c) device similar to (b) but with a different design introducing a longer path.</i> ^[161]	27
<i>Figure 10: Schematic of thermophoretic transport of a solute or particles in a solution exposed to a temperature gradient. A concentration gradient is generated towards the cold side of the temperature gradient as a result of the application of the thermophoretic force to the particles/solute dispersed in the solution.</i>	29
<i>Figure 11: Standard photolithography and PDMS molding technique for fabricating microfluidic devices. The photoresist is cured using a photomask at specific regions of interest, the wafer is then filled with PDMS and cured. The PDMS is then peeled off the wafer and sealed using a microscope glass slide</i> ^[186]	34
<i>Figure 12: Corona discharge treatment used for sealing microfluidic devices by bonding PDMS with glass.</i> ^[193]	36
<i>Figure 13: Picture of a peltier thermoelectric module used as a heat pump. The dimensions of the module are 40x40 mm.</i>	37
<i>Figure 14: Schematic illustration of the principles of atomic force microscopy.</i> ^[208]	38

<i>Figure 15: Schematic of an AFM force curve and cantilever bending.....</i>	<i>40</i>
<i>Figure 16: a) Schematic of a scanning electron microscope, b) beam-sample interactions.^[220]</i>	<i>42</i>
<i>Figure 17: Working principle of Confocal Laser Scanning Microscopy.^[231]</i>	<i>45</i>
<i>Figure 18: a) Principles of the electron excitation and the emission of fluorescence radiation, b) Schematic of an X-ray fluorescence equipment and its working principles.^[94]</i>	<i>47</i>
<i>Figure 19: a) Picture of the microfluidic device used for the gellan gum, b) Schematic of the channel's arrangement in the microfluidic device, c) Picture of the assembly of the device with the Peltier module.</i>	<i>53</i>
<i>Figure 20: a) Schematic of the two-layer device. Top part is used for the manipulation of the mechanical properties of biomaterials, middle part is a PDMS oil and gas permeable membrane and bottom part is used for the polymerization of NaALG in the main microchannel by the infusion of an acidic oil to reduce the pH of the solution. (b) Picture of the 8cm long microfluidic device.^[246]</i>	<i>56</i>
<i>Figure 21: Low-alcyl gellan gum viscosity change as a function of temperature for a solution of 1% w/v GG.^[247]</i>	<i>58</i>
<i>Figure 22: Picture of the microfluidic device setup for the gellan gum case. A syringe pump is used to flow the cold tap water on the "cold" channel, a power supply controls the current (and subsequently the temperature) of the peltier module and the Joule heater.</i>	<i>59</i>
<i>Figure 23: Picture of the sodium alginate (sandwich like) microfluidic device. The power supply controls the current of the Joule heater, the "cold" channel is supplied by a syringe pump, thermocouples monitor the hot and cold channel temperatures.</i>	<i>62</i>
<i>Figure 24: a) 4 spots across the 600 μm wide fiber of local AFM indentation measurements, b) Area (20x20 μm) of each spot containing 25 contact points.</i>	<i>69</i>
<i>Figure 25: Force - displacement curve fitting on the JPK nanowizard software. Green colour curve represents the Hertz model fit, red curve represents the approach and purple one the retract movement of the piezo at the substrate.</i>	<i>70</i>
<i>Figure 26: Microfluidic device design, with 200 μm thick PDMS walls between the channels and 600 μm wide main channel. Hot and cold side channels are highlighted in red and blue respectively</i>	<i>85</i>
<i>Figure 27: Picture of the microfluidic device from with the two thermocouple holes next to the side channels (marked with red). They serve as receptors for the thermocouples.</i>	<i>86</i>
<i>Figure 28: Schematic of the temperature distribution across the device and its electrical analogy in terms of thermal resistances.</i>	<i>86</i>
<i>Figure 29: Picture of the microfluidic device with an incorporated thermocouple hole to the Joule heater (in red). The hole is directly above the joule heater and the thermocouple is inserted and is in direct contact with the low melting point alloy.</i>	<i>88</i>
<i>Figure 30: Dispersion of nano-CaCO_3 particles at the NaAlg solution inside the microfluidic device. Pictures before and after the application of sonication and organic solvent. A fully transparent channel with a thin white line underneath is noticed before whereas a white transparent line across the whole channel is observed after.....</i>	<i>92</i>
<i>Figure 31: NaALG 1% stiffness gradient profile across the width of the material. Error bars represent standard error. Exponential fit was used for creating the trendline. Each point is the average of 3 areas on the same width position across the length of the same fiber.....</i>	<i>93</i>

Figure 32: Picture of the microfluidic setup consisting of the device the pelier module and the 3 thermocouples mounted at the a) LMPA, b) cold water outlet and c) between the device and the peltier module.	96
Figure 33: Effect of the CaCl_2 cross-linker concentration to the stiffness of uniform 1% GG materials. Error bars represent standard error. Each point is the average of 3 areas randomly selected on the same uniform stiffness fiber.	98
Figure 34: Effect of the GG concentration to the stiffness of uniform surfaces with 5 mM of cross-linker added. Error bars represent standard error. Each point is the average of 3 areas randomly selected on the same uniform stiffness fiber.	99
Figure 35: Gellan gum 1% stiffness gradient profile across the width of the fiber. Error bars represent standard error. Exponential fit was used for creating the trendline. Each point is the average of 3 areas on the same width position across the length of the same fiber.....	101
Figure 36: Effect of 200nm polystyrene particles on the stiffness of uniform 1% GG substrates. Error bars represent standard error. Each point is the average of 3 areas randomly selected on the same uniform stiffness fiber.	102
Figure 37: Stiffness gradient profile across the width of two Gellan gum 1% fibers, with the blue line representing the sample prepared with PS particles and the red line representing the sample prepared without the addition of PS particles. Error bars represent standard error. Exponential fit was used for creating the trendline. Each point is the average of 3 areas on the same width position across the length of the same fiber and each trendline represents a single sample.	103
Figure 38: Young's modulus values for the stiffness gradient GG fiber (left axis) and the corresponding local concentration (right axis). The dashed line is an exponential fit. In the inset the Young's modulus for different GG concentrations obtained from uniform substrates used to calibrate the main curve. Error bars represent standard error. Each point is the average of 3 areas on the same width position across the length of the same fiber.....	105
Figure 39: SEM images on 4 different areas to demonstrate porosity change across the width of the fiber.	109
Figure 40: Pore size distribution versus Young's modulus data across the width of the material. Blue line represents the pore size and red line represents the stiffness of a single gradient GG fiber. Polynomial fit was used for creating both trendlines. Each stiffness point is the average of 3 areas on the same width position across the length of the same fiber. Each pore size point is the average pore size of a $2 \times 2 \mu\text{m}$ area across the width of the same fiber. Error bars represent standard error.....	110
Figure 41: Effect of GG concentration on the stiffness gradient profile across the width of each material. Three different concentration GG fibers are represented each with a colored line (red 0,8%, blue 1% and yellow 1.5%). Each point is the average of 3 areas on the same width position across the length of the same fiber and each trendline represents the stiffness profile across the width of a single sample. Error bars represent standard error. Exponential fit was used for creating each trendline.....	112
Figure 42: Effect of temperature gradient (applied at the microfluidic device) on the stiffness gradient profile across the width of the 1% GG fibers. Three different GG fibers were fabricated at various temperature gradients represented each with a colored line (red $3.6 \text{ }^\circ\text{C mm}^{-1}$, blue $4.5 \text{ }^\circ\text{C mm}^{-1}$ and yellow $5.4 \text{ }^\circ\text{C mm}^{-1}$). Each point is the average of 3 areas on the	

same width position across the length of the same fiber and each trendline represents the stiffness profile across the width of a single sample. Error bars represent standard error. Exponential fit was used for creating each trendline. 114

Figure 43: Effect of residence time (in the microfluidic device) on the stiffness gradient profile across the width of 1% GG fibers. Error bars represent standard error. Three different GG fibers were fabricated each with a different residence time in the device are represented 3 colored lines (red 23 min, blue 25 min and yellow 28 min). Each point is the average of 3 areas on the same width position across the length of the same fiber and each trendline represents the stiffness profile across the width of a single sample. Exponential fit was used for creating each trendline. 116

Figure 44: Schematic of the procedure followed during the x-axis stiffness gradient formation. A syringe pump is slowly filling the beaker containing the gradient GG fiber which is placed at a vertical position. 120

Figure 45: Two-dimensional stiffness gradient towards the length and the width of the material. Position along the width is exhibited on X-axis, Young's modulus on Y-axis and position across the length of the material is illustrated with curves of different color for each individual area. The position along the length of the material was approximated every 0.5 cm with the softest area to be the red curve, followed by the blue, the yellow and the (stiffer) green one. Error bars represent standard error. Exponential fit was used for creating each trendline. Each point represents the average of a 20x20 μm area with 25 contact points.... 121

Figure 46: UV effect on the stiffness gradient of 1% GG fibers before and after its application. Error bars represent standard error. Exponential fit was used for creating each trendline. Each point is the average of 3 areas on the same width position across the length of the same fiber..... 127

Figure 47: GG 1% w/v supplemented with α -MEM stiffness gradient. Error bars represent standard error. Exponential fit was used for creating each trendline. Each point is the average of 3 areas on the same width position across the length of the same fiber..... 129

Figure 48: Visual inspection for the determination of the biocompatibility of different substrates seeded with MC3T3s and stained with calcein AM and propidium iodide on day 3. The substrates exhibit uniform stiffness. a) Material made with deionized water, b) Material with FBS coating, c) Material made with α -MEM on day 1, d) Material made with α -MEM. Yellow lines highlight the boundaries of the uniform GG fibers. 131

Figure 49: Different cell seeding densities of MC3T3s across the GG fibers exhibiting uniform stiffness with a seeding density of: a) 200 b) 1000 and c) 2000 cells/ mm^2 . Calcein AM and propidium iodide were the selected cell stains. Yellow lines highlight the boundaries of the uniform GG fibers. 135

Figure 50: Optimal cell seeding density of 850 cells/ mm^2 deposited on the surface of the uniform stiffness GG fibers after a) 1 and b) 7 days. Calcein AM and propidium iodide were the selected cell stains. Yellow lines highlight the boundaries of the GG fibers. 135

Figure 51: Migration and proliferation of osteoblasts (MC3T3) over 7 days of culture onto the stiffness gradient 1% GG fibers. Day 7 control sample is exhibiting uniform stiffness. Day 1, 3 and 7 were selected as the time markers for confocal imaging. Calcein AM and propidium iodide were the selected cell stains. Yellow lines highlight the boundaries of the GG fibers..... 137

Figure 52: Migration and proliferation of osteoblasts (MC3T3) on the stiffness gradient 1% GG fibers. Confocal images of the PKH stained MC3T3 cells were captured at different time markers up to 7 days of culture. Scale bars represent 100 μm . Stiffer side at the top and softer one at the bottom of each picture. Yellow lines highlight the boundaries of the GG fibers. . 140

Figure 53: a) Live/dead staining of MC3T3 osteoblasts, on the surface of 1% GG stiffness gradient fibers after 7 days of culture, b) cell viability , c) cell spreading and d) cell density for the 2 different stiffness areas of the material. Error bars represent standard error. Each plot is generated from the extracted data of picture (a) and corresponds to a single stiffness gradient fiber loaded with MC3T3s. Calcein AM and propidium iodide were the selected cell stains. Yellow lines highlight the boundaries of the uniform GG fibers. 142

Figure 54: Schematic representation of osteoblast activity on the substrate over time. 144

Figure 55: a) Microscope image as well as calcium and phosphorus XRF pictures of stiffness gradient gellan gum fibers loaded with MC3T3 cells across their surface, b) Calcium and phosphorus deposits after 15 days of culture in normal and osteogenic medium. Yellow lines highlight the boundaries of the uniform GG fibers. Each point is the average of 3 areas located at the same width position for 3 different samples exhibiting similar stiffness gradient. 147

Figure 56: Example of the spectrum of elements obtained upon the X-Ray scanning of the sample. 149

Figure 57: Schematic of the different areas measured across the MC3T3 cell loaded and gradient GG fibers used for the quantification of each element across the width of the material from the XRF images. Averages of each area were later plotted in a similar way as the AFM plots. 150

Figure 58: a) Microscope, actual, calcium and phosphorus XRF pictures of 1% stiffness gradient gellan gum fibers loaded with MC3T3 cells across their surface, b) Calcium and phosphorus deposits after 30 days of culture in both normal and osteogenic medium. Yellow lines highlight the boundaries of the uniform GG fibers. Each point is the average of 3 areas located at the same width position for 3 different samples exhibiting similar stiffness gradient. 151

Table of tables

<i>Table 1: Elasticity across the width of 4 independent samples that were prepared under the same conditions to test the reproducibility of the method. Four samples were prepared in total at the same microfluidic device, out of a 1% GG solution, at 27 minutes and 4.5 °C/mm temperature gradient. The YM values are the average of three measurements per sample, prepared in quadruplicate for the areas located on the same width position, followed by the standard error. The stiffness gradient is also averaged from the 4 independent samples and is expressed at Pa per μm across the width of the fiber.</i>	<i>118</i>
<i>Table 2: Cell density difference of MC3T3s (expressed in %) between the soft and the stiff area of 3 independent stiffness gradient fibers that were incubated for 1,3 or 7 days. Control sample is a uniform stiffness fiber cultured for 7 days. The average difference is calculated from 3 independent samples that were prepared for each day of culture (3 data sets of images similar to Figure 51), with the errors reported as standard error.</i>	<i>138</i>
<i>Table 3: XRF experiments on 1% GG fibers loaded with MC3T3 osteoblasts.</i>	<i>146</i>

Introduction

In recent years, the scientific area of biomaterials has been extensively studied to solve several tissue engineering and healthcare problems.^[1,2] The overall goal is to replace or restore damaged tissues by accurately mimicking the complex structures of human tissue. In mammals there is a variety of different types of cells that interact with themselves and the substrate they are found on.^[3] However, for keeping these cell types functional, it is often required an alteration to a series of parameters which is found in nature in the form of gradients that ensure a smooth transition from one cell type to another.^[4] Therefore, the accurate representation of human or animal tissues often requires manipulating the raw materials found in nature to develop novel synthetic biomaterials that exhibit unique properties which make them a friendly environment for several different cell types. Several methods have been developed over the years with microfluidic techniques to be considered as one of the most efficient.^[5] Their high-throughput and low-cost characteristics have enabled us to screen multiple types of biomaterials that could potentially steer biomedical research towards new pathways for solving several tissue engineering problems.^[6] Though, there are few techniques that allow us to accurately mimic human tissues by manipulating different types of biomaterials to control cell behavior and especially at the microscale.^[7,8] The main aim of this project is the development of a non-toxic technique that would enable us to fabricate biomaterials exhibiting gradients of mechanical properties that can be tuned according to the specific cell requirements. For achieving that goal, we combined the area of microfluidics with heat transport phenomena to develop a novel technique which could serve that purpose. We validated the produced biomaterials by characterizing their structure and their mechanical properties which gave us valuable information for the optimization of the technique. Furthermore, we exposed the

modified biomaterials to mammalian cell cultures for monitoring their activity over time and investigating their bio-functionality on the substrate. Since the materials are exhibiting a different magnitude of their mechanical properties across their surface it was expected to trigger a different cell behavior and functionality locally for each area.^[9-11] By performing a live dead assay for the cultured cells we were able to image the cell population on the substrate and obtain valuable information on cell density, viability, migration and spreading which revealed the promising potential of the fabricated biomaterials. The cells were responding according to the stiffness gradient with their activity being dictated by the elasticity of the substrate. Furthermore, we investigated cell bio-functionality of bone cells by looking at the deposition of minerals which consist the basic building blocks for the formation of bone tissue. We observed a gradient of minerals across the material's surface which followed the gradient of mechanical properties that the biomaterials exhibited. These results indicated the manipulation of cell activity and functionality by the gradient biomaterials which stems from the novel technique that was previously established in this project. Finally, this novel technique has set the foundations for further exploration towards the manipulation of the biomaterial's mechanical properties at the microscale using temperature gradients and heat transport phenomena, towards more complex structures that might potentially serve as future implants or patches for wound healing or tissue scarring applications.

Literature review

Extracellular matrix (ECM)

Tissue engineering is an emerging scientific field with a broad range of applications which mainly focuses on replacing or repairing biological tissues.^[12] A common approach to achieve that goal is the combination of biocompatible materials, sometimes assembled in complex structures, with cells and bioactive molecules into functional tissues that mimic the real tissue.^[12] An extracellular matrix (ECM) is the non-cellular component which not only provides a physical support for the cultured cells but also commences important biochemical and biomechanical cues required for tissue homeostasis, differentiation and morphogenesis.^{[13,}
^{14]} Chemical composition and assembly (in 2-D or 3-D) depend on the tissue or organ type as well as its function.^[15] For example, high levels of fibrillar proteins such as collagen are found in soft tissues, cartilage is high in hyaluronic acid which gives its shock absorbing properties and bone tissues are rigid due to the increased concentration of calcium phosphate in the fibrillar matrix.^[16] There are significant variations of the ECM composition though even on the same tissue. In particular, within a single cartilage tissue proteoglycan composition varies upon the distance from a joint where the bones meet and laminins exhibit heterogeneity in different areas across the skin basement membrane.^[17] Such microenvironment involves cell-substrate and cell-cell interactions but also a series of physicochemical parameters such as temperature, pH, CO₂ and oxygen levels all of which influence cellular activity.^[18] Our understanding of these interactions and how the ECM influences cell behavior is considered one of the key research areas in tissue and biomedical engineering and has been improved thanks to the various novel techniques.

In general, there are 3 major therapeutic strategies for repairing damaged tissues in patients: 1) direct implantation of cells, 2) implantation of a fully grown tissue consisted of cells and scaffolds, 3) in situ tissue regeneration.^[19] The first case involves the extraction of the cells or their aggregates from the patient or a compatible donor to either inject them right away or implant them upon in vitro combination with a biodegradable scaffold. For the second strategy, a complete 3-D tissue is required which is previously grown in vitro and is consisted of a scaffold and the appropriate cells.^[20] The difference here is that the tissue will be implanted once it forms a complete cellular network and reaches a maturation stage. For instance, Meinel et al. have developed novel porous silk fibroin scaffolds that were loaded with bone marrow derived stem cells which were cultured for up to 5 weeks in osteogenic conditions before being implanted into critical size calvarial defects in mice.^[21] In this way, the slowly degradation of the protein matrix controlled the hydroxyapatite deposition and formed a trabecular-like bone matrix which promoted advanced bone formation and demonstrated its use in bone tissue regeneration.^[21] As for the in situ regeneration, a scaffold which stimulates the cells in the patient's body to promote a local tissue repair is implanted directly into the damaged tissue.^[22] Landa et al. developed such a scaffold out of calcium crosslinked alginate hydrogels and injected it into an rat heart 7 days after the myocardial infarction to prevent adverse left ventricular failure.^[23] The presence of the implant in situ, provided mechanical and physical support to the heart but also stabilized the infarct preventing a potential expansion before eventually biodegrading over time.^[23]

Tissue engineering

In the early stages of tissue engineering research, several skin and cartilage ECMs were developed and then successfully commercialized.^[24] During the 1990-2000 decade the main goal was to evaluate different types of biomaterials that would be biocompatible, biodegradable and would also promote the cellular activity.^[25] Collagen, polylactides and polyglycolide are namely just a few of the materials employed in the synthesis of 3D scaffolds in the past.^[1] The fabrication of a matrix with the ability to degrade at a controlled rate proportional to the growth rate of the specific cells seeded in it but also its potential to not elicit a detectable foreign body reaction was one of the major challenges at that time.^[25] For example, Bruin et al. in 1990, developed a new polyglycolide material to construct a macroporous two-layer artificial skin in order to investigate its degradation and diffusion rate.^[26] They fabricated and cross-linked the polymeric membranes which were then attached via a polyurethane adhesive, with a mean pore size of 90-250 μm similar to the dermal tissue. Upon implanting this artificial tissue in guinea pigs they discovered that the new material allows rapid cell growth, does not evoke any adverse tissue reaction and degrades completely after 4 to 8 weeks.^[26] At that time, the combination of cells and matrix on skin or even cartilage was quite effective due to the fact that the targeted tissues did not require any significant or complicated processes, such as vascularization.^[27]

In early 2000s, researchers started working towards more complex tissues and different cell types incorporated in 3D structures, as technology bloomed with the development of novel fabrication techniques (such as electrospinning),^[28] the automation of processes and the research drive towards micro and nano technology.^[29] For example, Flaim et al. created an ECM microarray platform using a robotic DNA spotter to study the differentiation of mouse embryonic stem cells.^[30] The main advantages of this platform were the parallel study of

multiple microenvironments and the use of up to 1000 times less proteins than the existing conventional means at that time, used for investigating cell-matrix interactions.^[30]

Later on, the extensive study of single stem cells, a quite promising biological area, had a significant impact on the development of clinical solutions for several complex tissues.^[31] Stem cells have the extraordinary ability to develop into several different cell types during their early stages of growth.^[32] During stem cell division, each newly created cell has the potential to either remain in the current condition or differentiate into another specialized cell type, such as muscle, bone or even brain cell.^[33] As a result, in tissues they sometimes serve as an internal repair system, dividing essentially into a specified cell type without limit to replenish the damaged tissue with a fresh one.^[34] Stem cells are different from the other cell types as they exhibit two unique characteristics. Firstly, they are unspecialized cells capable of expanding their population through cell division, even after long periods of inactivity.^[35] Secondly, they have the ability to differentiate into tissue or organ specific cells under certain physiologic or experimental conditions.^[35] In some tissues, such as bone marrow, stem cells frequently split up to restore and replenish worn or even fractured tissues.^[36]

Recent advances in the field of biomaterials and the development of novel 3D scaffolds that present unique solutions in wound healing and tissue repair problems, have emerged in regenerative medicine.^[37, 38] Kolesky et al. have developed a novel 3-D bioprinting technique to create micro-engineered environments that could potentially broaden the horizons of drug screening and fundamental studies of wound healing, angiogenesis, as well as stem-cell niches.^[39] Using a custom-made 3-D printer with four independently controlled printheads, they have precisely co-printed vasculature, ECM and other cell types to create on demand vascularized heterogenous tissue constructs.^[39] This technique has opened new avenues in the manufacturing of functional 3-D tissues and organs.

However, the impact of tissue engineering in patient treatment remains relatively low. Skin grafts,^[40] artificial arteries,^[41] cartilage and heart implants are just a few examples of the materials that have been implanted in patients but most of these procedures are still experimental and costly.^[42] On the other hand, using these tissues for other research purposes such as drug development or cancer invasion could be beneficial.^[43, 44] For example, creating a fully functional lab grown human tissue to speed up the screening of potential drug candidates with low cost compared to conventional methods and without using laboratory animals for this purpose.^[45, 46]

Recent advances in tissue engineering

Biological tissues are complex assemblies of cells and extracellular matrices (ECM) which are, often but not only, consisted of collagen and other polysaccharides.^[47] Cell activity is mainly influenced by the surface characteristics and the properties of the substrate they are cultivated on.^[48] Therefore, the design of scaffolds that offer topographical guidance to the cells and mimic accurately the tissue microenvironment presents a great challenge in tissue engineering.^[49] In the past few years several techniques have been established to tackle this problem but the need for continuous optimization on existing practices as well as the generation of new ones is crucial for numerous biomedical applications.^[50] For instance, the design of ECMs that promote durotaxis, offer a great opportunity for applications in wound healing and tissue scarring. In 2003, Wong et al. developed polyacrylamide gradient substrates that dictated vascular smooth muscle cell migration which was considered to be essential for future vascular tissue engineering applications, such as the control of restenosis.^[51]

Nowadays, it is widely known that factors such as ECM stiffness, adhesion and ligand topography regulate cell activity in different cell types.^[52] Specifically, the mechanical properties of ECM namely, shear and tension stresses regulate cell adhesion,^[53] proliferation,^[54] migration and differentiation.^[55-57] Changes in substrate stiffness as well as transcription factors trigger different responses in stem cell populations.^[58, 59] Though, in particular, stiffness has a great effect in mesenchymal stem cells (MSCs) differentiation where bone formation is promoted on stiffer substrates (< 25 kPa) and in softer ones (0.1 – 15 kPa) neurogenic and myogenic differentiation takes place.^[56, 58] Recent studies on MSCs differentiation have revealed that stem cells cultured on a rigid substrate coated with a softer hydrogel of varying thickness, can sense and deform the overlaid substrate up to 5 μm and 15 μm depth respectively.^[60, 61]

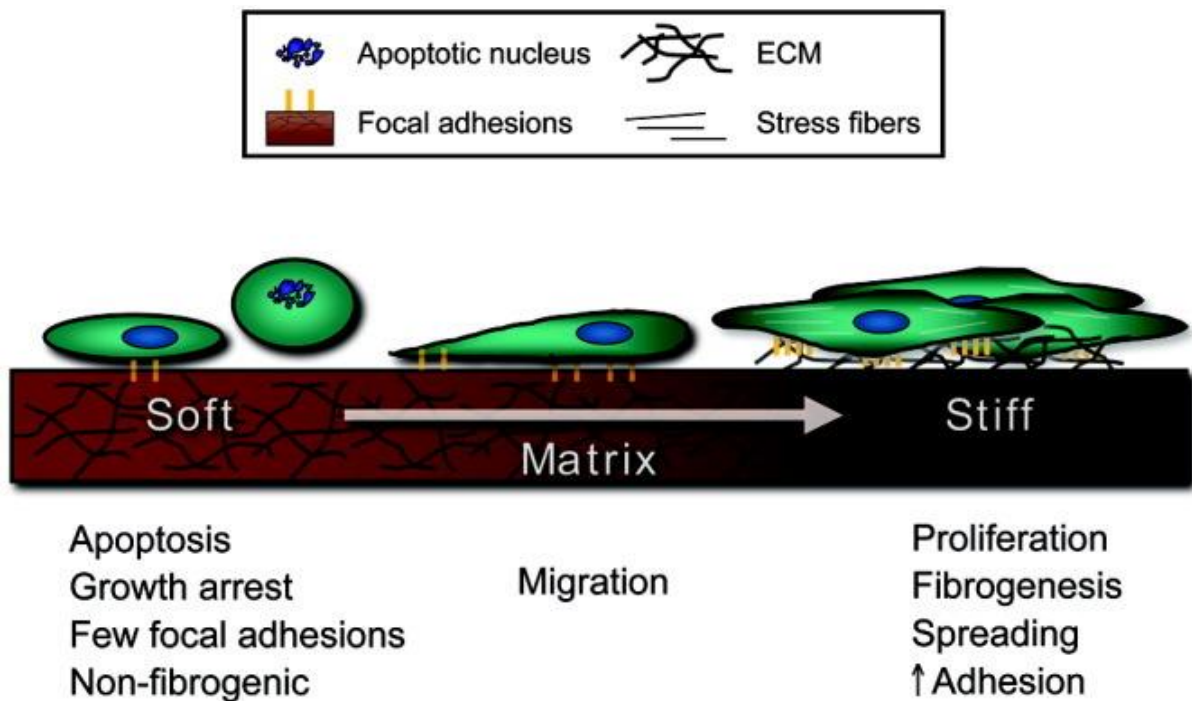


Figure 1: Matrix elasticity effect on cell behavior, Cell morphology, proliferation, spreading and adhesion increase as matrix stiffness increases.^[52]

Hydrogels

Hydrogels are soft solid materials consisted of three-dimensional networks of hydrophilic chains with interconnected pores that can retain high amounts of water while holding their structure due to the physical or chemical cross-linking of the chains.^[62] For a material to be considered as a hydrogel, by definition, it should contain at least 30% of water.^[62, 63] They are generally flexible materials because of their considerable water content.^[62, 64] Hydrogels, exhibit a hydrophilic nature due to the presence of hydrophilic groups across their network, such as -COOH, -NH₂, -OH etc.^[65] In response to several physical and chemical stimuli, they undergo a sol to gel phase transition.^[66] The term physical stimuli can refer to temperature, light intensity, pressure while the chemical stimuli refer to pH, ions, and biochemical compositions.^[66, 67] Though, most commonly those volume phase transitions are reversible with hydrogels being able to return to their original state upon a reaction once the stimuli is removed.^[67, 68]

Hydrogels for biological applications are usually developed (but not limited to) from biopolymers or polysaccharides.^[69, 70] As previously mentioned, they can be classified into physical, chemical, or biochemical materials.^[62] The physical gels go through a liquid to gel transition due to the alteration of the environmental conditions like pH, ionic concentration, temperature, or even a two component mixing.^[66] Chemical ones are characterized by mechanical integrity and degradation resistance which stems from the covalent bonding between the chains.^[62] In the case of biochemical gels, enzymes or amino acids are taking part in the gelation process.^[62]

ECM fabrication processes include the use of 3-D solid scaffolds, hydrogels, and other biocompatible materials.^[71] Hydrogels are most commonly used as the basic building blocks

of an ECM.^[72] They are considered as excellent candidates for ECMs in tissue engineering but also in other applications such as biosensors and drug delivery platforms due to their porous structure which allows the transport of nutrients, gases and other substances and their flexible nature which resembles the one of natural tissue.^[73]

At first the hydrogel chains that are dispersed in an aqueous solution, at the presence of cations they progressively cross-link increasing the average molecular weight up to the gelling point where the 3-D solid network appears.^[64] The structure of this physical network of junctions between the chains varies. These junctions may be formed due to hydrogen bonding between the side groups of macromolecules,^[74, 75] ionic bonding or even the interaction between single or double helices.^[76] Homopolymers for example are consisted by one type of monomer which might have a cross-linked structure depending on the nature of it and the polymerization technique, while copolymeric hydrogels contain two types of monomers with hydrophilic nature.^[66] In some cases, the junctions result from segments of macromolecules that do not dissolve in the presence of common solvents (e.g. aqueous solutions) or they are formed by large and rigid crystallinities that prevent the reversible degradation of gels.^[77, 78]

Regarding the formation thermodynamics of the gels, they can be one or two phase systems as well as systems exhibiting an incomplete phase separation.^[79] With a temperature change, their network junctions can be formed or melted usually upon cooling and heating respectively.^[80] For example, liquid polydimethylcarbosiloxane-silocane (PDMCS) converts into a gel when temperature increases at 80-160 °C.^[81] This transition stems from the unfolding of the PDMCS macromolecule followed by the rearrangement of intramolecular into intermolecular hydrogen bonds which leads to an extended configuration when temperature increases and it's the basis of the gel network.^[80] The properties, structure and formation process of physical gels greatly differs depending on the nature of their three dimensional

network, although they are all considered as a soft solid material that contains a liquid in a substantial quantity.^[78]

Gradient ECMs

In nature there are multiple complex materials and components that could potentially lead us to the design of new bioinspired materials with unique properties.^[82] Therefore, it is really important to engineering biomaterials that mimic the in vivo tissue microenvironment and modulate cell activity. Several ECM properties, such as porosity or stiffness, are often found in nature in the form of gradients with some of them playing an important role at a wide variety of tissues.^[83] For example, at the osteochondral interface there are two diverse types of tissue (bone and articular cartilage) exhibiting different mechanical, structural, electrical and other properties.^[4] For that reason, the design of a gradient scaffold which will ensure a smooth transition from articular cartilage to the subchondral bone is essential.^[4]

In general, gradients in the concentration of solutions or in the properties of surfaces are important in both biological and chemical processes.^[84, 85] Cells are extremely sensitive to environmental differences such as substrate stiffness or chemoattractant concentrations.^[86] Hence, the generation of gradient properties becomes more puzzling as a high resolution is required for having effective spatial control.^[87]

The generation of well-defined and tunable gradients remains a huge challenge especially in cell biology where cell interactions are being studied at the microscale.^[88] Cell migration, for example, one of the key aspects of cell behavior, is a spatiotemporally regulated bioprocess.^[89] The cell extends its protrusions by polymerizing actin microfilaments using

proteins such as profilin, cofilin and Arp2/3.^[90] These lamellipodia or filopodia form focal adhesions to the ligands of the ECM through transmembrane proteins (integrins).^[91] Upon adhesion and intracellular polarity is established and proteins known as GTPases and myosin II generate forces to relocate the polarized cell towards the actin microfilament network.^[92] At the same time, the adhesions at the other edge of the cell are disassembled to allow the cell to slowly migrate.^[93]

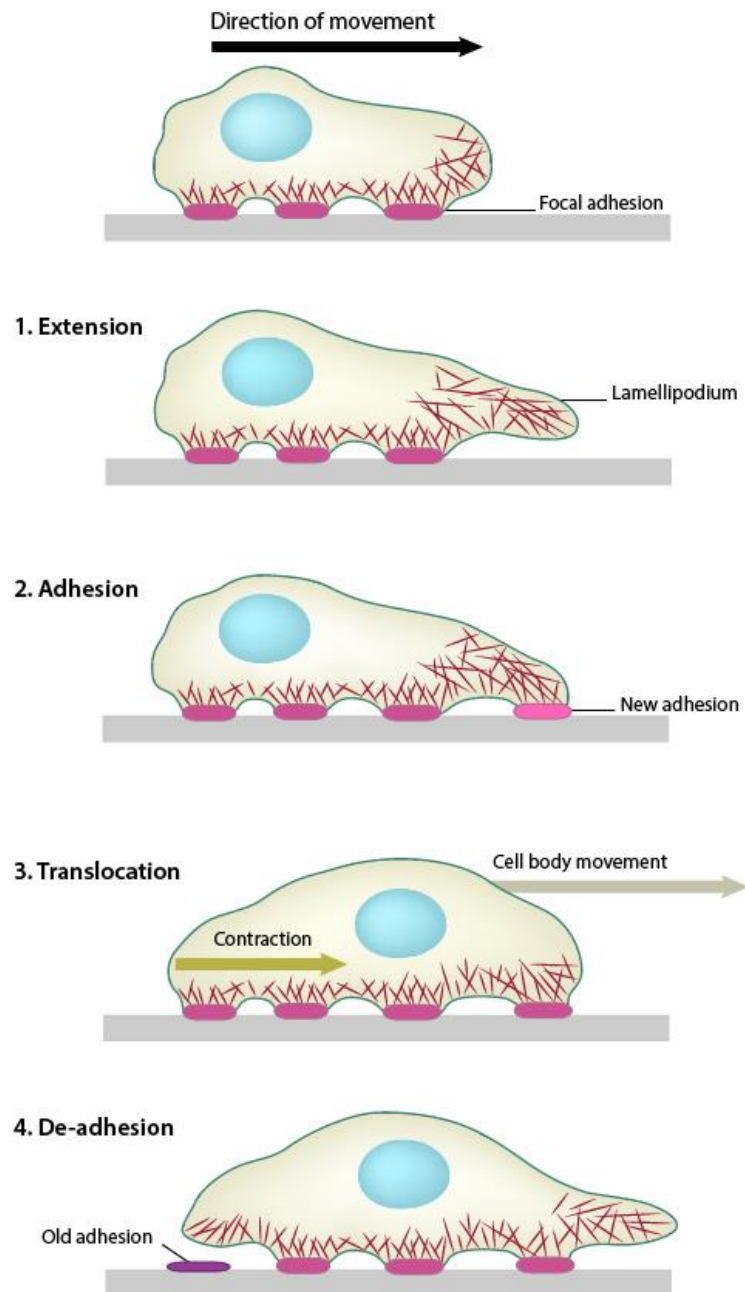


Figure 2: Cell movement mechanism through the extension of lamellipodia, adhesion with the substrate (focal adhesions), translocation of the cell body and de-adhesion of the local focal adhesions previously created.^[94]

Cells remodel the ECM proteins through secreted proteases to induce prolific locomotion.^[95] This mobility of the cells is in accordance with the physical properties of the ECM environment.^[96] For example, durotaxis is the term used for directional cell locomotion which is induced by stiffness gradients at the cell-substrate interface.^[97] Cells tend to migrate

at the rigidity gradients towards the greater stiffness area as they sense the environment they are cultured on, process the mechanical stimuli and respond accordingly.^[9, 98] Consequently, applications such as tissue repair and wound healing could potentially be improved using scaffolds that exhibit a stiffness gradient and as a result, they induce durotaxis to the specified areas of interest. However, there are numerous different cell types that respond to the matrix changes only within their preferred range of stiffness. For example, soft tissue brain cells are found at lower stiffness ranges (0.1-1 kPa), muscle cells prefer slightly stiffer substrate (8-20 kPa) whereas bone cells become functional when found at much harder tissue microenvironments (40-100 kPa).^[99]

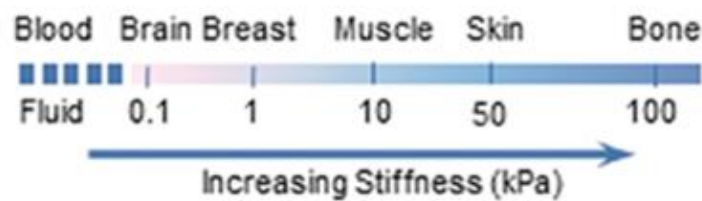


Figure 3: Suitable matrix stiffness range for different cell type families, from softer brain tissue to stiffer muscle and bone tissues ranging from 0.1 to 100 kPa.^[100]

In the past few years, many techniques were developed to generate rigidity gradients on biocompatible and other types of materials. These include microfluidic photopolymerization,^[7] sliding mask photopolymerization,^[11] controlled sinking in cross-linker solution,^[10] altering the height of the polymer,^[101] etc. One interesting approach to mimic the tendon to bone region was introduced by Li et al. in 2010. They exploited the technique of electrospinning to generate a continuous nanofibers with a calcium phosphate bone-like coating.^[102] Electrospinning is a well-defined technique to fabricate electrospun nanofibers which can be usually folded in 3-D scaffolds for tissue engineering applications.^[103] By using this technique and controlling the

immersion of the material on the calcium phosphate solution they produced fibers exhibiting a gradient of mineral deposition along the long axis of the substrate.^[102]

Another method to produce gradient biomaterials was introduced by Sunyer et al. and involved the gradual photopolymerization of PAA hydrogels. The polymer containing a certain amount of photoinitiator was irradiated by a UV light source. An opaque mask moving at a controlled speed slowly uncovering the gel solution was used to form and control the stiffness gradient which was induced by the polymerization degree of the hydrogel. However, new limitations occurred mostly related to cell viability due to toxic residual monomers, photoinitiators and chemical cross-linkers.^[104, 105] The addition of excess photoinitiators is impeding cell growth due to the fact that some residues of the toxic substance have been “trapped” in the matrix. Also, the use of UV light averts the creation of a 3D-Scaffold as cells could not be embedded in the substrate. This is due to the fact that UV is fatal to the cells and as a result, they cannot be mixed with the hydrogel before polymerization.

Contemporary strategies of ECM fabrication

Currently, biomaterials are fabricated using natural or synthetic polymers which are modified with growth factors and peptides to provide support and scaffolding for cell growth.^[2] ECMs are designed in a way where reciprocity between the cells and the matrix occurs that offers the right biological cues and signals for influencing cell morphology and phenotype.^[2] Synthetic biomaterials offer the ability to control several key properties such as rigidity, structure and degradation rate, whereas naturally occurring materials embed structural and functional molecules that make the substrate cell friendly.^[2] A number of biocompatible and biodegradable materials such as polyethylene glycol (PEG),^[106] gelatin methacrylate

(GelMA),^[107] collagen,^[108] hyaluronic acid (HA),^[109] etc. have been utilized for therapeutic and medical purposes to optimize cell-substrate interactions and control cell activity. For example, Leipzig et al. have developed a methacrylamide chitosan scaffold and varied the solvent concentration to control the stiffness of the resulting hydrogels in order to study neural stem cell behavior. They tested different substrates from soft to stiffer tissue ranging from 1 to 30 kPa to determine the optimal hydrogel stiffness for neural stem cell proliferation and differentiation. Schneider et al. applied a more chemical approach to design composite 3D polymeric matrices. They fabricated elastic PolyLysine-Hyaluronan films using various crosslinking densities to investigate the adhesion of human chondrosarcoma cells on the substrate. Ranging from 3 kPa all the way up to 400 kPa they discovered that cells attach better on the substrate as Young's Modulus increases up to 300 kPa which was the optimal stiffness for the specific cell type.^[110]

Gellan gum

Gellan gum (GG) is an extracellular polysaccharide composed by repeating units of 1,3- β -D-glucose, 1,4- β -D-glucuronic acid, 1,4- β -D-glucose and 1,4- α -L-rhamnose.^[111] It is produced during the aerobic fermentation of *Sphingomonas elodea* bacteria and it is widely known in the food industry for its use as a thickening and stabilizer agent,^[112] while its medical application up to date is more focused towards targeted drug delivery and tissue engineering applications.^[113, 114] Gellan gum is often found in two types, high and low acyl GG. The low acyl form produces firm non elastic gels whereas the high one softer and more elastic hydrogels.^[115] The use of high acyl GG is limited as the low acyl one is preferred due to its ability to form strong 3-D gels and withstand higher temperatures up to 140 °C once

crosslinked.^[116] Low acyl GG is often featured at multiple scientific articles mostly at food or biomedical related journals. When dissolved at a high temperature (< 70 °C) aqueous solution, the polysaccharide is found as disordered coils which self-assemble into double helix structures when the solution starts to cool down below the gelling point (~50 °C).^[114] However, the true gel network formation relies on the aggregation of helical sequences which form oriented bundles known as junction zones.^[117] These zones are then cross-linked, in the presence of monovalent or divalent cations, resulting in the formation of a three-dimensional network which give rise to the hydrogel.^[118] GG forms strong 3D gels when cross-linked with monovalent and divalent cations such as Na⁺ and Ca²⁺. Though, divalent cations form stronger bonds between the GG chains resulting in more firm gels than the ones cross-linked with monovalent ones.^[114]

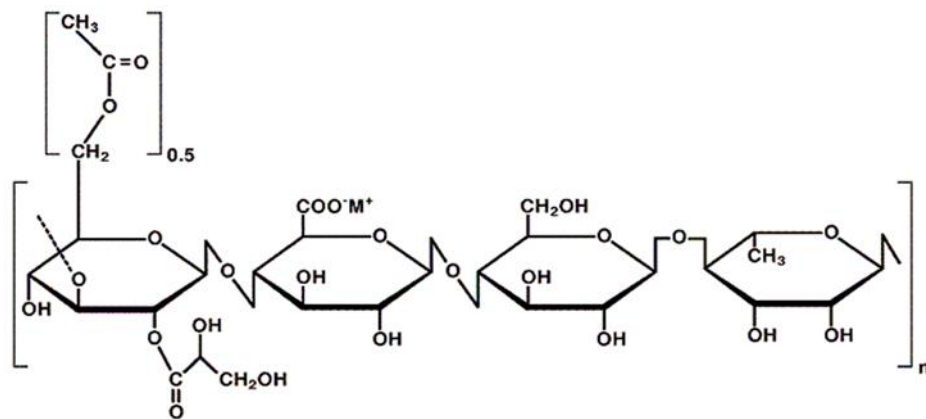


Figure 4: Low acyl gellan gum chemical structure.^[116]

It is a biocompatible material which does not require the presence of UV light, photoinitiators or other (toxic) chemical residues but relies on self-assembly mechanisms upon the decrease of the solution temperature. As seen on the recent work published by Jeon et al. GG modified scaffolds have been used for investigating Chondrocyte cell proliferation and mRNA expression.^[119] They fabricated saponin GG scaffolds by altering the concentration of

Sa and Calcium cross-linker which resulted in different ligand concentrations on the biomaterial. The next step was to seed cells on the hydrogels and evaluate their adhesion, proliferation and viability over 1, 2 and 3 weeks' time. They observed that cells behaved differently as the biological cues were increasing from one material to another, but reached a plateau or even decreased upon a certain amount of Sa.^[119] Another study presented by Vieira et al. shows the bioactive properties and the self-mineralization capacity of calcium enriched methacrylated GG beads.^[120] They demonstrate the mineralizing and drug delivery potential of the calcium loaded Me-GG beads by investigating the metabolic activity of human adipose stem cells over time and observing the release profile of model drug molecules.^[120] In addition, the bioactivity was tested in vivo by implanting the beads onto mice which after 2-weeks yielded positive results on the mineralization of the Me-GG substrate and an overall osteogenesis potential.^[120] All the above were achieved by switching from thermal gelation of GG that was previously used to an ionic crosslinking using CaCl₂.^[120] We can therefore evidently see that GG is a suitable and easy to use candidate for manipulating its mechanical properties and studying the impact of this microenvironment on cell cultures.

Sodium alginate

Another material extensively used for the creation of novel three-dimensional ECMs is Sodium Alginate (NaAlg). Alginates are polysaccharide polymers found in nature typically extracted from brown seaweed. The extraction occurs when an alkaline solution is used to dilute and solubilize the alginic acid contained. The alginic acid is then obtained from the resulting thick mass and its converted into salts one of which is sodium alginate. Alginic acid is consisted by repeated units of L-guluronic and D-mannuronic acid residues in a linear polymer chain. Alginates can undergo hydrolysis which depends on time, pH and temperature and leads to the formation of an acid gel with high viscosity as a result of intermolecular binding.^[121] Upon gelation the water molecules are trapped in the alginic matrix due to capillary forces but they don't remain immobilized. This water molecule migration is of great importance in cell encapsulation and drug delivery applications.^[122] In the presence of divalent and multivalent cations, alginate forms gels or precipitates. Alginates with a high content of guluronic acid blocks produce higher strength gels as they exhibit a robust attraction for divalent ions compared to the ones rich in mannuronic (Figure 5).^[121]

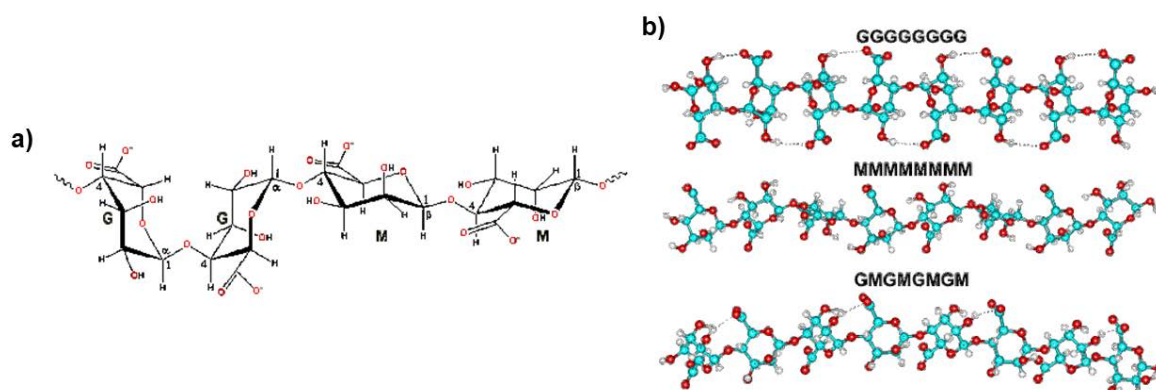


Figure 5: Chemical formula of: a) mannuronic (M) and guluronic (G) alginate monomers, b) blocks of single or alternating M and G residues.^[123, 124]

Alginate gels exhibit properties such as swelling, viscoelasticity and permeability which lay the foundation for several biomaterial research projects ranging from ECM development to 3D bioprinting. Recently Valentin et al. published an article about 3D bioprinting of alginate hydrogels for directing collective cell migration.^[125] They tuned the degradation kinetics of the gels by tuning the cross-linker concentrations during the deposition of the gels in the 3D printing process.^[125] Alginates have also been used for implants in porous ceramic scaffolds to improve cell seeding and to control better the release of growth factors.^[126] The development of porous ceramic composite alginate materials was first introduced by Florczyk et al. who fabricated a bone tissue engineering construct in order to control BMP-2 growth factor release in vitro and improve the osteogenesis of osteoblasts.^[126] Additionally, they later implanted these alginate scaffolds loaded with MSCs in ectopic locations in rats to assess in vivo the bone formation. The alginate ceramic composites exhibited greater cell seeding efficiency and cell retention within the scaffold but also controlled release of bone tissue growth factors and enhanced osteogenic activity in vivo. Hence, we can conclude that NaAlg is a biocompatible material suitable for cell cultures and tissue engineering applications.

Most of the studies though, use different substrates with different but uniform stiffness across their surface, which provide us with limited information regarding cell-matrix and cell-cell interactions.^[127] In most cases, a substrate is prepared exhibiting uniform stiffness across its surface which often results from a certain polymer or cross-linker concentration that is being used. Afterwards, cells are seeded on each one of the ECMs with different stiffness and their activity is monitored over time. However, these studies can be considered preliminary as there are limited interactions between cells and matrix as well as cells on different conditions. The prospect of a technique that manipulates the properties of biomaterials independently from the polymerization part, could potentially tackle these limitations and yield single component

gradient materials with an increased biocompatibility level. In addition, natural tissue often exhibits a gradient of mechanical properties (e.g. osteotendinous interface) which is impossible to accurately mimic using a uniform stiffness substrate with a limited stiffness range.

Over the years, various methods have been developed to generate gradients on both 2-D and 3-D surfaces and especially on hydrogels due to their multiple applications and particularly in tissue engineering.^[128, 129] Photo-cross-linking, prepolymer concentration gradient and surface bound gradient methods have been developed to fabricate composite materials that exhibit certain (desired) properties of two or more components.^[128, 130, 131] Though, low cost and high-throughput approaches were needed to accelerate the screening of novel composite materials with a reduced cost.^[132] Currently, the optimal methods to design and synthesize new biocompatible materials use microarrays or microchannels to fabricate or analyze several different combinations of materials on microscope glass slides or titer plates.^[133-135] These methods were able to swiftly screen cell-material interactions from a pool of material candidates to identify and later develop the optimal biomaterials which offer control over cell activity and functionality.^[132, 135]

Microfluidic fabrication

Microfluidics is the science of manipulating small amounts (micro and nano litres) of liquids using microchannels with dimensions of a few micrometers only. There are multiple advantages in microfluidic devices. At first the ability to use small quantities of reagents as well as the disposable, easy to make devices, minimize the cost of the experiments and as a result studies in the microscale are now more accessible to lower budget research groups.^[136] Another key aspect of microfluidics are short experimental times, which gives us the possibility

of conducting multiple different experiments in just a few seconds time.^[137] Also, microfluidic devices offer fast and accurate separation of liquids which yields high sensitivity and resolution.^[5] We can therefore conclude that it is a powerful tool that offers unlimited capabilities in the control of molecular concentrations and flows in spatiotemporal studies.

On the other hand, some of the disadvantages of microfluidics involve the difficulty of scaling up and often the extensive experimental setup which requires the use of external pumps, valves pressure controllers etc. In addition, one of the major drawbacks comes from the physics of microfluidics and relates to mixing of different components. In the microscale, the dominant forces are different from the ones at the macroscale thus microfluidic mixing greatly differs from conventional mixing. The Peclet number (Pe) is a dimensionless number which is defined as the ratio of advective transport rate to diffusive transport rate in both mass and heat transfer. Due to the (small) geometry of the microfluidic channels we often have a low Peclet number which at laminar flow (low flow rates), indicates that mixing mostly occurs via diffusion. Diffusion is a quite slow phenomenon which makes the mixing of two components in a microchannel a quite difficult and tricky process. However, there are several ways to tackle these limitations and enhance the mixing process such as the design of ridges and grooves,^[138] the use of microstirrers,^[139] thermal or electrical mixing,^[140, 141] acoustic waves etc.^[142, 143]

One of the first to exploit microfluidic devices for patterning different types of cells, were Chiu et al.^[144] They fabricated a three dimensional microfluidic device to pattern mammalian cells and proteins onto complex structure surfaces, for tissue engineering applications and the development of biosensors (Figure 6). A powerful technique which allowed the deposition of multiple different cell types in close proximity and complex structures that could potentially enable us to study the molecular interactions between cell types at processes such as embryonic

morphogenesis or tumor angiogenesis. The layers were made from PDMS, deposited on a two-plane silicon wafer followed by alignment and sealing to create a 3-D structured microfluidic device. They then patterned on petri dishes proteins such as BSA and fibrinogen and also two types of cells, Bovine adrenal capillary endothelial cells (BCEs) and Human bladder cancer cells (ECVs). Once the cells were fully grown, they peeled of the device from the dish to allow the cell pattern to grow.

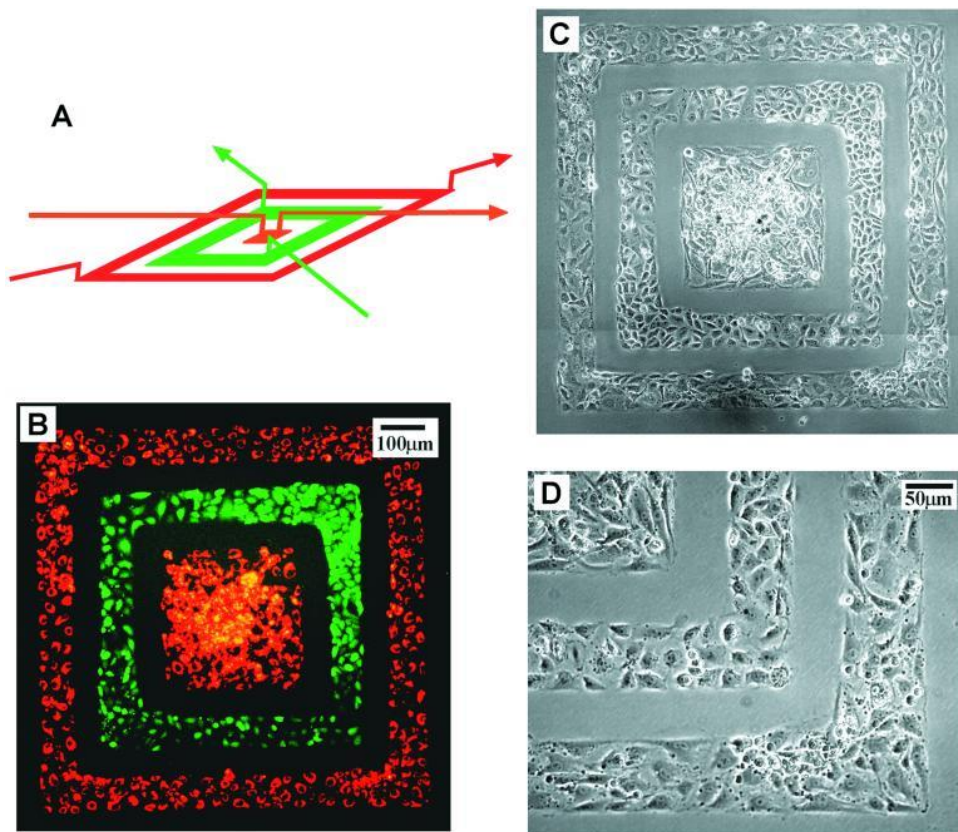


Figure 6: a) 3-D schematic of the pattern stamp created at the microfluidic device, b) fluorescent image of two types of patterned cells, Human bladder cancer cells (ECVs) labelled in green with 5-chloromethylfluorescein diacetate (CMFDA) and Bovine adrenal capillary endothelial cells (BCEs) labelled in red using DiI-conjugated acetylated low density lipoprotein. c) and d) phase contrast images of the two different cell types that were patterned.^[144]

Currently, there is a broad range of applications fluid mixing,^[142] fabrication of biopolymers,^[145] foams etc.^[146] to name a few, where a microfluidic approach has been adopted

instead of a large scale one.^[147] The common term “lab on a chip” describes perfectly all of the above as several laboratory functions can be integrated on a single microfluidic chip and achieve both automation and high-throughput screening.^[148] In addition, resolution is increased with the decrease of the size of the device, facilitating single particle tracking and collection but making them susceptible to clogging and more sensitive to particle absorption on their surface.^[149, 150] Microfluidic systems are usually consisted by a microfluidic device (chip), made out of several different types of materials, with polydimethylsiloxane (PDMS) to be the most popular choice, and often a syringe pump is employed to generate a flow. The device can be made using a wide variety of techniques such as 3-D printing, molding and nanofabrication, with photolithography to be the most popular one. The liquids are injected to the microchannels in the rate of micro- or nano- liters per unit of time which gives us better control and manipulation over the fluid properties.^[5] As a result transport phenomena in microscopic systems are now better understood and they can be easily observed and manipulated through various complex microfluidic designs. Berejnov et al. have used photolithography techniques to produce structured microfluidic networks for studying multiphase transport through porous media.^[151] By tuning the surface properties and altering the geometry of the pores, they were able to investigate a wide range of parameters related to multiphase transport phenomena that were particularly useful later for energy applications such as oil recovery and hydrogen fuel cells.^[151]

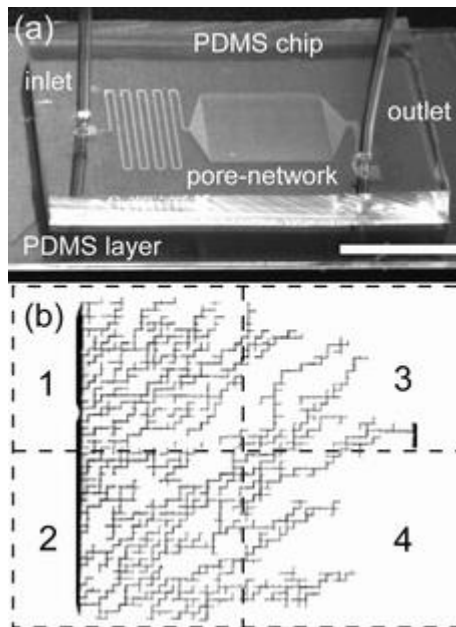


Figure 7: a) Picture of the microfluidic chip used by Berejnov et al. (scale bar of 15 mm) to study multiphase transport through porous media, b) Network of channels (pores) developed at the middle of the microfluidic channel with width varying from 10 to 80 μm to better understand how multiphase flows diffuse through the pore-network.

While PDMS has multiple advantages as a fabrication material, it also has several limitations. Due to its high porosity, organic solvents usually swell in the material.^[152] PDMS is also permeable to gases which makes the study of multiphase flows even trickier but is helpful when it comes to biological processes that require a constant O_2 or CO_2 supply.^[153, 154] Also, it has a low thermal conductivity making the walls between the channels to act as insulators.^[8, 155, 156]

Recently, various research groups focus on the fabrication of gradient hydrogels to mimic the tissue microenvironment on a single material, tackling the problems of biocompatibility and gradient control. Though, most of the research on that field is based on microfluidic gradient generators and monodispersed emulsified droplets loaded with cells. Microfluidic designs such as Y-shape tube,^[157] passive diffusion channels,^[158] T-junction and flow focusing devices are all employed for this cause.^[127, 159] They offer effective control over the material

properties and excellent bio-functionality. Although, they are lacking reproducibility and accuracy mainly due to the complexity of the production process or the different surface properties related to the cross-linker densities.^[10, 101] One of the first techniques that were developed for the fabrication of gradient polymers in the microscale is the microfluidic gradient generator.^[160] They produced a parallel flow microfluidic chip which was used to study the effect of chemoattractant gradients on blood cell migration, stem cell differentiation and various chemotaxis applications. The unique design of the device allowed the generation of gradients on a steady state flowrate, as it splits all the inlet fluids and then it recombines them on a single outlet channel. Though, during the recombination of the flows, the outlet channel expands the final liquid resulting in an expansion of the gradient range which makes it less steep and promotes a certain degree of mixing.

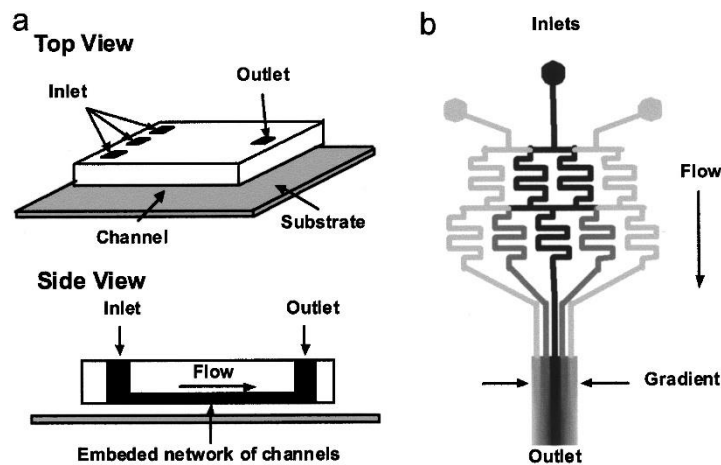


Figure 8: a) Schematic of the PDMS microfluidic device exhibiting an array of channels used for the generation of gradients, b) schematic of a microfluidic gradient generator. Different fluid streams are introduced from the top inlets, then mixed and recombined to a concentration gradient at the outlet channel.^[160]

Thermophoresis

In order to fabricate gradient biomaterials through microfluidic manipulation in a precise and tunable manner another method needed to be explored. Vigolo et al. demonstrated a novel microfluidic separator in colloidal suspensions using thermophoresis (Figure 9).^[161] They designed a microfluidic device consisting of a main channel and two side channels to act as hot and cold thermal sources. By carefully imposing and controlling temperature gradients across the main channel and exploiting the transport phenomenon of thermophoresis they were able to selectively drift the suspended particles towards the hot or the cold side.^[161]

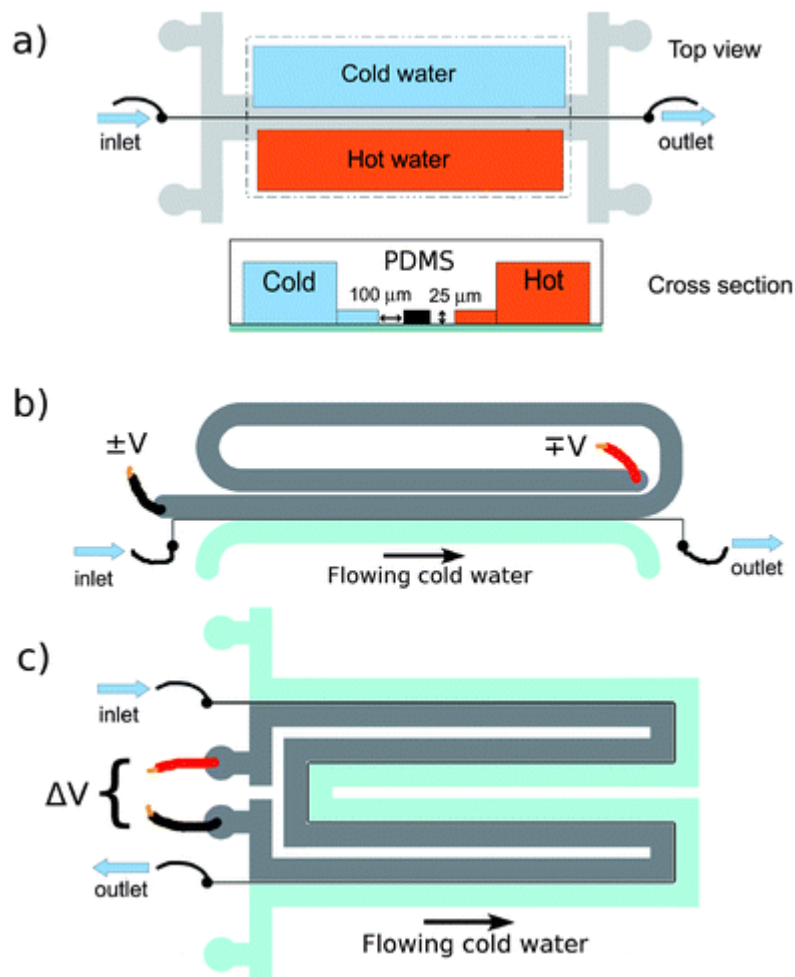


Figure 9: a) Schematic of a microfluidic device that induces a temperature gradient by flowing hot and cold water to the side channels, b) alternative design using a silver-epoxy resistive Joule heater for the hot channel, c) device similar to (b) but with a different design introducing a longer path.^[161]

Thermophoresis is a physical transport phenomenon that is mostly noted in micro geometries. It is the migration of a solute or particles dispersed in a solution towards the hot or the cold side in a temperature gradient ^[162]. Originally it was observed by Ludwig that salt solutions of high concentration were easily crystallized around a cool U-tube.^[163] Later, Soret proved that the application of a temperature gradient on a liquid leads to a homogenous concentration gradient of the dispersed salt in it.^[164] Thermophoresis in aerosols was also reported by Tyndall in 1870 who observed dust particles moving away from a heated surface on a dusty room.^[165] It took more than 100 years to discover that thermophoresis is also having an effect on solid-solid interfaces. Specifically, in 2006 Schoen et al. predicted via simulations in molecular dynamics that a particle confined in a single walled carbon nanotube will move towards the colder side on an axial temperature gradient.^[166, 167] This phenomenon was demonstrated experimentally by Barreiro et al. a couple of years later.^[168] The migration of particles or solute in a temperature gradient is mainly dependent upon the particle size, the average temperature and the specific solute-solvent interactions.^[169] The thermophoretic force is applied to the suspended particles alongside Brownian motion in a temperature gradient.^[161] The effect of thermophoresis has a relatively small but significant effect, especially when it comes to convective mixing. One of the first to quantify the forces applied in particles was Epstein in 1924.^[170] He observed spherical particles in a gas under the effect of a temperature gradient and derived expressions for the force and the velocity of the particles in the slip flow regime. However, these expressions were not taking into account the high thermal conductivity particles and the large Knudsen numbers, and they were later improved by several researchers in the field throughout the years.^[171-173]

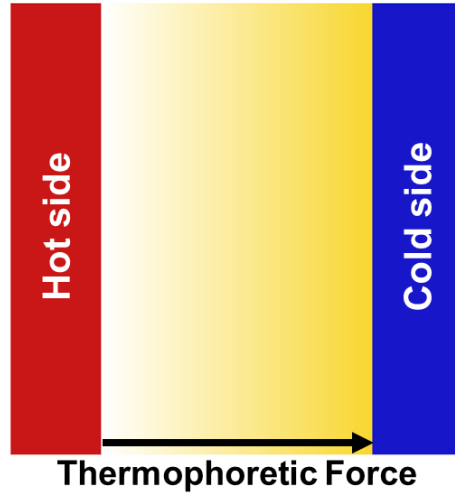


Figure 10: Schematic of thermophoretic transport of a solute or particles in a solution exposed to a temperature gradient. A concentration gradient is generated towards the cold side of the temperature gradient as a result of the application of the thermophoretic force to the particles/solute dispersed in the solution.

As stated before, thermophoresis is a particle transport mechanism brought into play on top of the Brownian diffusion in a presence of a temperature gradient. The total mass flux for diluted systems can be expressed as:

$$J = -D\nabla c - cD_T\nabla T \quad (1)$$

Where D is the Brownian Diffusion coefficient, D_T the thermophoretic mobility and c is the concentration of the solute. By considering that mass flux in a steady state is zero (1) can be transformed into:

$$\nabla c = -cS_T\nabla T \quad (2)$$

Where $S_T = D_T/D$ is called Soret coefficient.^[174] When S_T is positive, the particles move towards the cold side and we call it a thermophobic suspension, while the less frequent movement of the particles towards the hot side is called thermophilic suspension.^[169] Assuming

that convective effects are negligible and S_T is temperature dependent within the temperature difference ΔT across a channel of width w , then the steady state concentration at the hot side C_h is correlated to the cold one C_c as:

$$C_h = C_c \exp(-S_T \Delta T) \quad (3)$$

Nowadays, a big number of experimental studies have employed thermophoresis as the main tool to create gradients in colloidal systems and complex fluids. A recent study has demonstrated the use of thermophoresis to drive the isotropic-nematic transition in rod-like colloids.^[175] Thermophoresis was the driving force for the promotion of liquid crystal phase transitions for the accurate control over the concentration gradients of fibrous systems at the microscale, simply by fine-tuning the temperature gradient.^[175] Another study revealed the use of thermophoresis for controlling the structural, electrical and optical properties of gold plasmonic nanoparticles in order to present an alternative method to optical tweezers.^[176] In addition the motion of particles at a temperature gradient has been investigated both computationally and experimentally. In the study published by E. Michaelides, 4000 spherical nanoparticles with different material properties were simulated for four different liquids and the results that were generated have revealed the average thermophoretic velocity of the particles in the liquids.^[177] This study has shown the long-term movement of the particles towards the colder regions in a temperature gradient but also revealed that the thermophoretic velocity is proportional both to the kinematic viscosity of the fluid and the magnitude of the temperature gradient.^[177] It also confirmed the observations from previous experimental data that the thermophoretic coefficient depends more on the size of nanoparticles and less on the density ratio of particles to fluid.^[177, 178]

From all the above, we can deduce the fact that thermophoresis is a powerful tool that is currently employed for the fabrication of gradients and in general the manipulation of colloidal

systems in a wide variety of applications. In the present study, we employed thermophoresis for our microfluidic platform in the fabrication of a biomaterial exhibiting a stiffness gradient that will subsequently be used as a substrate for regulating cell activity.

Techniques

Microfluidic device fabrication

As stated before, PDMS is the most widely used material when it comes to microfluidic device fabrication due to its many advantages (physical properties, economy and easy to use).^[179] The most common option in material selection is Dow Corning's Sylgard 184, a two part system consisted of part A: silicone elastomer base and B: curing agent. The recommended mixing ratio is 10:1. By increasing the curing agent even up to 4:1 ratio the rigidity of the PDMS is increased, making it less elastic and preventing long channels to collapse.^[180] Further mixing with other materials can either alter the mechanical properties of the final product or even increase the biocompatibility of it.^[181] For example, to improve the hydrophilicity of PDMS surfaces, Gokaltun et al. added a PDMS-PEG block copolymer (BCP) at concentrations between 0.25-2%, before the curing step.^[182] In this way, the BCP segregated to the PDMS surface and created a hydrophilic substrate upon exposure to aqueous media which yielded contact angles from 31° down to 0° that lasted for up to 20 months of storage.^[182] Also, by altering the % of the BCP they were able to control the flexibility, the biocompatibility and the transparency of the material which demonstrated the ability to be potentially used in commercial applications.^[182]

There are several methods for fabricating PDMS structures, but the most common approach is casting on a reverse mold.^[183] These molds are usually prepared using photolithography techniques and they require a mask, a photosensitive resist polymer and a UV light source in order to pattern the desired structure (microchannels).^[184] The mask can be printed through different ways depending on the channel dimensions and the resolution we

want to achieve. It can be a simple laser printed transparent film with a resolution of 1200 dpi / 250 μm , or a high-resolution print on a thin polymer film with 10,000 dpi / 30 μm , all the way down to 420,000 dpi / 600 nm resolution when using a quartz photomask that is chromium printed.^[184] The design of the mask's blueprint is made by using any CAD software such as AutoCAD. The negative mold is fabricated by using several types of materials but the commonly used one is the SU-8 photoresist. A silicon wafer is often used as the base for the negative mold as it is a flat material with reduced roughness. The SU-8 is poured onto the silicon wafer and is then spin coated to reach the desired device thickness. The spin curves are available from the datasheet of the product and they are useful for estimating the optimal spin rate that corresponds to the desired thickness.^[185] For example 1250 rpm for 30 s yield a final thickness of approximately 205 μm when using SU-8 2075 photoresist. Later a prebaking stage is followed prior to the UV exposure to allow the SU-8 to evaporate its solvent. The mask that was previously printed is aligned with the spin coated silicon wafer and the UV radiation with a wavelength of 350-400 nm is emitted through the transparent micro channels for 10-20 seconds to ensure that the photoresist will be fully cured and prevent any poor bonding sites throughout the mold.^[184] Afterwards the mould is developed, baked and the unreacted photoresist is washed away, leaving the desired negative structure behind. The overall thickness is a function of spin coating speed and time.

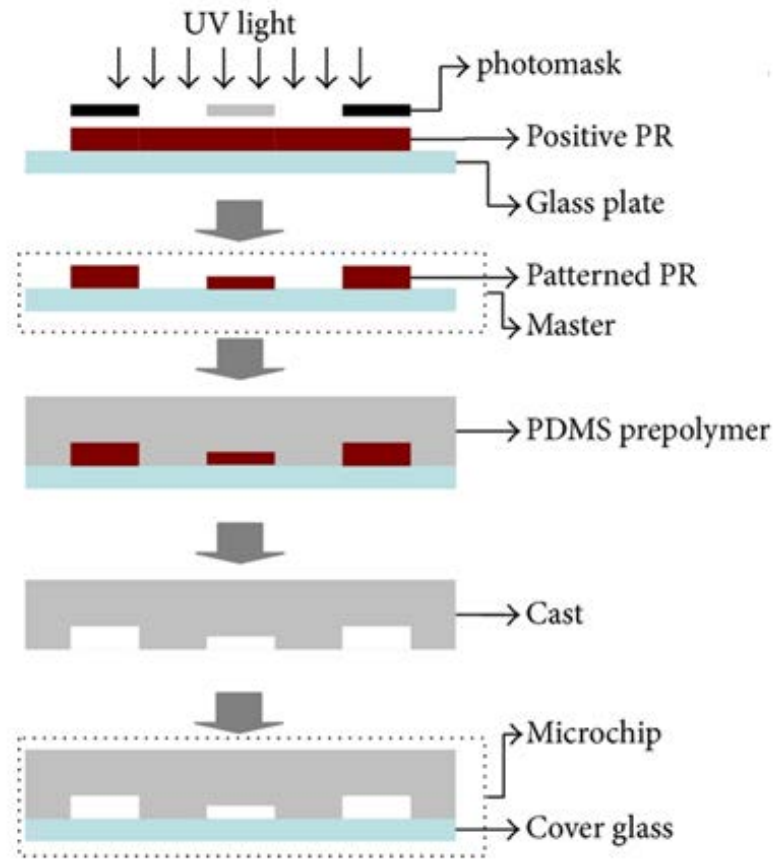


Figure 11: Standard photolithography and PDMS molding technique for fabricating microfluidic devices. The photoresist is cured using a photomask at specific regions of interest, the wafer is then filled with PDMS and cured. The PDMS is then peeled off the wafer and sealed using a microscope glass slide^[186]

Having created the negative mold on a silicon wafer the PDMS mixture is poured slowly on top of it so as not to create air bubbles. To remove the trapped air in the viscous PDMS liquid which will disrupt the device fabrication process, the mould-PDMS system is degassed prior to curing. Upon degassing, a baking process is taking place to speed up the curing of the polymer which has a pot life of 24 hours in room temperature. Depending on the oven temperature, the baking time varies with a reduced time being a result of increased temperature. For example at 70 °C a baking time of 90 minutes is required to ensure a fully cured and solid PDMS structure, while for a higher temperature the time is proportionally reduced.^[179]

In microfluidics the PDMS devices are often sealed by a standard microscope glass slide by using a plasma treatment.^[187] To perform a plasma treatment on both the PDMS and the glass surface a plasma chamber is required. The term “plasma” indicates an ionized gas consisted of electrons, ions and neutral atoms.^[188] It is formed by an oscillating electric field which is created within the gas region through capacitors or magnetic induction.^[189] The combination of low pressures, acceleration of electrons due to the electric field effect and the elastic scattering of electrons results in the heating of electrons.^[190] This plasma energy is then enough to ionize neutral atoms, form free reactive roots, excite molecules or atoms and heat the surface of PDMS locally.^[190] Plasma treatment removes the hydrocarbon groups and exposes the silanol hydroxyl groups (-OH) at the surface of the PDMS layer. Consequently, they form strong covalent bonds with glass (Si-O-Si) when the two surfaces are brought together.

Several methods have been employed for sealing the microfluidic devices onto a glass slide. Corona treatment a portable electric discharge equipment which produces a small amount of plasma and can be used to surface treat the PDMS device and the glass slide in a similar way as in the plasma chamber (Relyon, PZ2, Reylon plasma GMBH, Germany).^[191] It was first invented in 1951 by Verner Eisby, who applied this technology in an attempt to print on plastic.^[192] The corona discharge device is consisted of a high frequency power generator and a high voltage transformer connected to an electrode, which produces a major electric discharge close to the needle tip.^[191] As a result the electric field around that area is strong enough to make air electrons collide with atoms that are later converted to ions thus forming a small region of plasma around the electrode.^[188]



Figure 12: Corona discharge treatment used for sealing microfluidic devices by bonding PDMS with glass.^[193]

For having a more controlled environment a Peltier module is often used in microfluidic devices to control the overall temperature of the chip or a part of it.^[194] The Peltier module is a thermoelectric heater/cooler which operates according to the Peltier effect.^[195] This effect is generating a temperature difference on the module when a current flow through a junction between two electrical conductors.^[196] To create this electric current, we apply a voltage through an external power supply. Subsequently, one of the junctions is cooled down whereas the other one is heated up. Peltier modules act as a solid-state heat pump.^[194] They feature an array of n- and p- type semiconductors which have complementary Peltier coefficients and they are soldered, electrically in series but thermally in parallel, between two ceramic plates.^[197] They absorb heat from the environment on the cold side which is carried along by electron transport on the hot side as the electrons transit from a high to a low energy state.^[196] The Peltier thermoelectric modules offer a variety of advantages when it comes to temperature control as they are quite accurate, easy to control, they have a long lifespan, capable of heating/cooling far beyond the ambient temperature and they are considered as a quite cost-efficient tool.^[198]

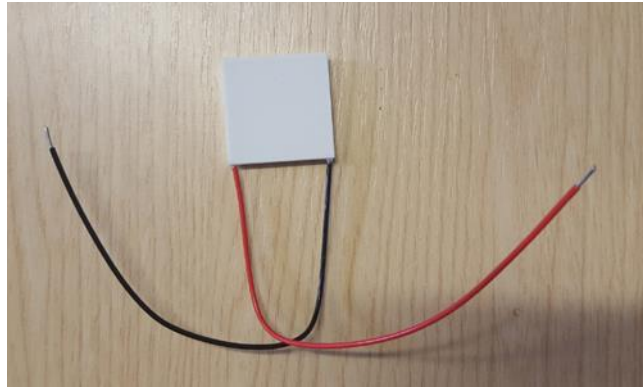


Figure 13: Picture of a peltier thermoelectric module used as a heat pump. The dimensions of the module are 40x40 mm.

Atomic Force Microscopy (AFM)

Scanning probe microscope (SPM) is one of the microscopy techniques used for obtaining images or surface scans using a probe that comes in contact with the sample.^[199] It was first invented by Binnig et al. in 1981 and it was a major breakthrough in science as we could investigate matter on the atomic scale for the first time. G. Binnig and H. Rohrer were later (1985) awarded the Nobel Prize in Physics for the invention of STM and its applications in the imaging of the Si(111)-(7x7) surface. Due to its amazing spatial resolution the STM had a significant impact on surface science. However, its major drawback was the use of electrical conduction on the sample as a tunnelling current flowing between the tip and the material is required. As a result, the STM could only image electrically conductive samples which is a huge limitation. One of the main branches of SPM is atomic force microscopy (AFM), a high-resolution microscope that can identify nanometre structures over 1000 times better than the optical diffraction limit. It was also invented by Binnig et al. who used a vibrating probe to “sense” the surface topography.^[200] Their main advantage compared to the other STM techniques used at that time, was the design of a cantilever beam with ultrasmall mass and the ability to measure its displacement in Angstroms, which enabled them to look at inter-atomic

forces between single atoms. The AFM quickly became a powerful and handy tool in surface mapping and characterization.^[201] It has been widely used both in air and liquids to obtain high resolution images of biomolecules and polymers.^[202, 203] In some cases, atomic resolution images of several insulating materials have been reported.^[204, 205] At the present time, in order to investigate the topography of a sample's surface, there are two main dynamic AFM modes: amplitude and frequency modulation AFM.^[206, 207] The first one, which is also known as tapping mode is based on the use of a stiff cantilever with a blunt tip at its end which is excited near its free resonance frequency. The feedback parameter that is used to measure the topography or the surface is the oscillation amplitude of the microlever. In addition, the phase shift between the tip oscillation and the driving force could be monitored to map the property variations of the material. On the other side, in frequency modulation the cantilever is continuously oscillating with a certain amplitude at its resonance frequency. The interactive forces between the tip and the surface of the sample define the cantilever's resonance frequency. The difference between the actual frequency and the cantilevers one is the main source of contrast. Subsequently, an image is obtained by using a constant frequency shift to map the surface characteristics of the material such as morphology, modulus, friction etc.

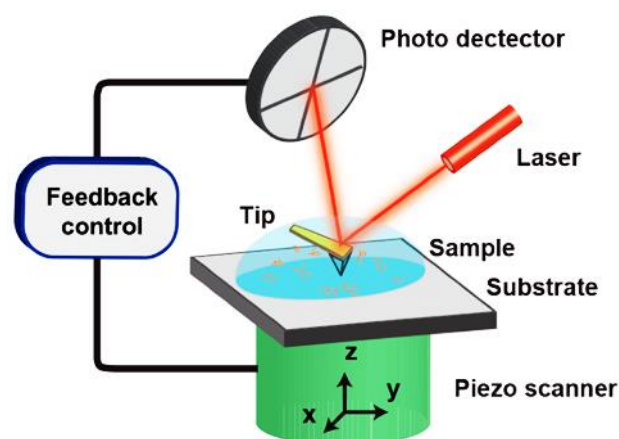


Figure 14: Schematic illustration of the principles of atomic force microscopy.^[208]

The principles of the AFM are quite simple to understand. A cantilever is mounted on a nano or even atomic precision scanning device which allows the three-dimensional movement of the tip. The tip is usually a reflective surface to facilitate laser deflection. A two-segment photo diode is used to track the deflected laser beam and is aligned with it. Depending on the deflection of the tip, the position sensitive photo diode builds a map of the height of the sample's surface.^[209] As a result, an image of the height map of the sample is created or even a force map of the surface depending on the approach mode that is used.^[210]

The cantilever/tip material depends on the application and the interactions with the substrate, but for most (common) applications either Si or Au tips are being used.^[211] In general there are several forces that take place during the tip-sample approach or separation that depend upon hydrophilic/hydrophobic interactions, the presence of a medium or other parameters.^[211] When the tip is far away there is no interaction, however in a few micron distance electrostatic interactions occur.^[212, 213] During the contact phase elastic repulsion forces dominate.^[212] At the tip-sample separation on atomic level, the major interaction is the Van der Waals force.^[211, 212] On the nanoscale though adhesion forces are taking place depending on the hydrophobicity/hydrophilicity of both the tip and the substrate but also the presence of a liquid film (for example water condensate from air) which will generate capillary forces at measurements in ambient.^[213, 214] Finally when the tip is far away from the surface all connections break between the tip and the substrate and no further interactions occur.^[213]

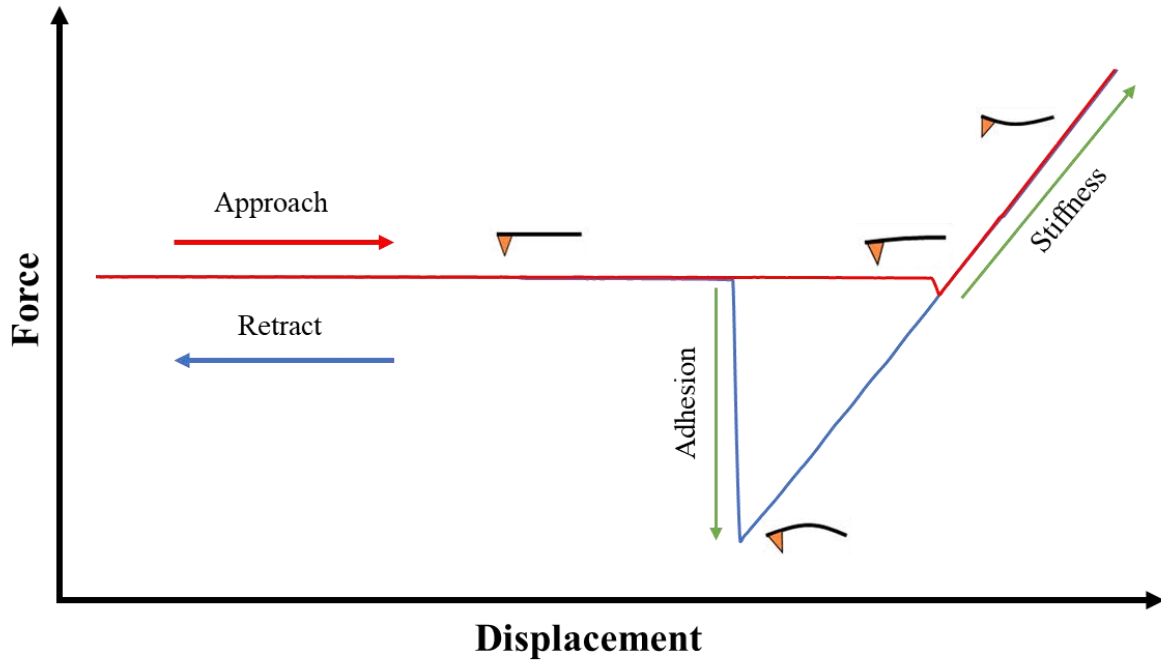


Figure 15: Schematic of an AFM force curve and cantilever bending.

Scanning Electron Microscopy (SEM)

The surface characterization and imaging of solid samples was one of the toughest challenges in the early 40s. As methods for producing even thinner samples were developed the early stages of electron microscopy were developed. The first one was Ruska in 1933 who illuminated the sample surface at a grazing incidence using an electron beam to obtain low resolution (10x) images of copper and gold surfaces.^[215] There were several other attempts to improve the grazing incidence method using transmission electron microscope (TEM) but they yielded only marginally better results.^[216] The major breakthrough came in the 60s, when the Stereoscan 1 SEM instrument was marketed in the UK by Cambridge Instrument Company and brought SEM to a form similar to the one that we use nowadays.^[217] The main principle of SEM is based on the interactions of electron beams with the atoms of a sample surface at

various depths in order to produce an image as a result. A wide variety of different signals are produced such as secondary, reflected or back scattered electrons, X-rays, absorbed current and transmitted electrons. The secondary electrons imaging (SEI) is producing high resolution images as the electrons are emitted from a short distance, very close to the sample surface, showing details that can be less than 1 nm in size. Back scattered electrons (BSE) are reflected from the surface by elastic scattering and emerge from locations that are found deeper in the sample, making BSE images less resolute than SE ones. However BSE images are more related to the atomic number of the sample, which is a useful tool that gives us information about the distribution of different elements in the specimen. The energy or the wavelength characteristic X-ray spectroscopy can be measured to map the distribution of elements and identify their quantities.^[218] The main advantage of SEM micrographs is that they produce a three dimensional picture with a large depth of field which is due to the narrow electron beam they use. This 3-D depiction of the sample surface is very useful for observing in detail the structure of the specimen. SEM resolution can reach close to 250 times the magnification limit of the top quality light microscopes.^[219]

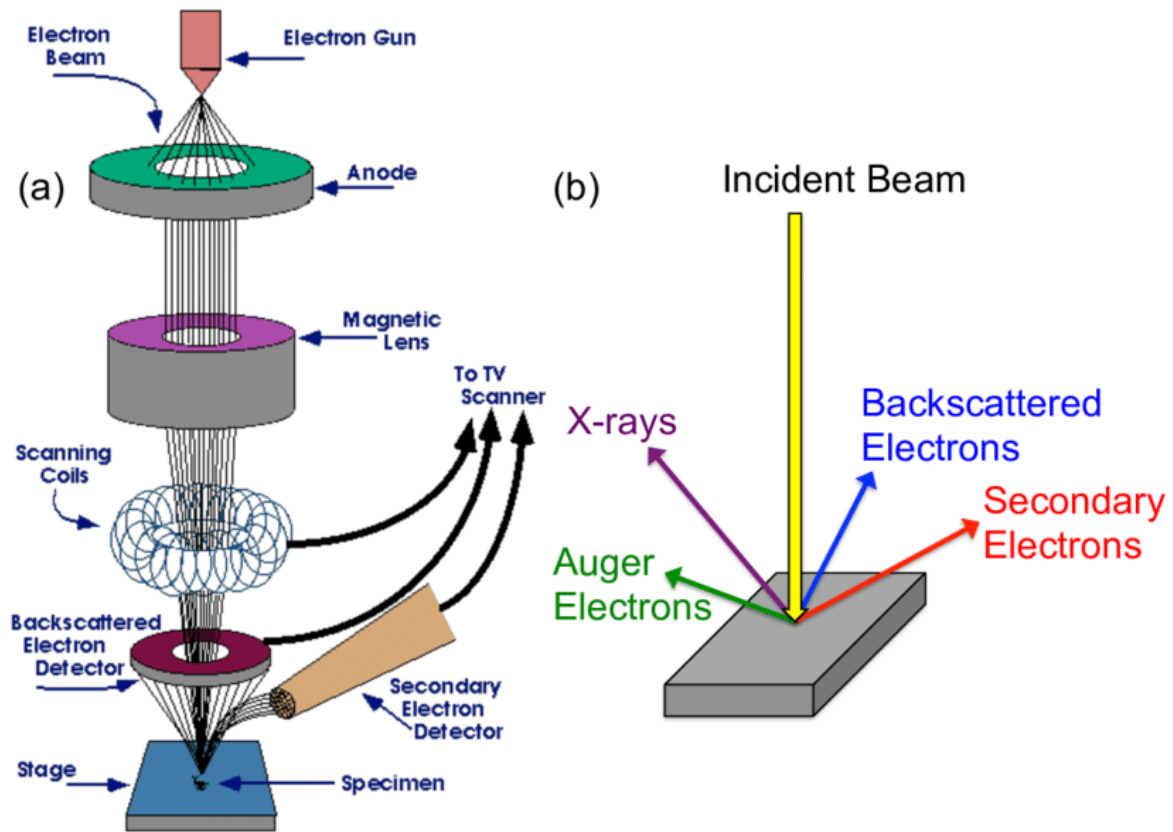


Figure 16: a) Schematic of a scanning electron microscope, b) beam-sample interactions.^[220]

Micro-compression rig

The mechanical properties of micro particles can be evaluated by the method of diametrical compression. Two parallel rigid plates compress the sample and the force of the compression is then measured to give us the particle's properties.^[221] This method was widely applied to the mechanical characterization of large particles ($>200\ \mu\text{m}$) such as polystyrene beads, detergent particles or even quartz sand agglomerates.^[222, 223] Though the determination of the properties of smaller microspheres was only possible upon the development of a novel micromanipulation technique used in a similar manner to conduct diametric conversion.^[224] It was developed by Prof. Zhang at the University of Birmingham in order to characterize the

mechanical properties of various type of particles, such as animal cells,^[224, 225] bacteria and micro-capsules.^[226, 227] Recently it was employed by Yan et al. for characterising agarose micro particle suspensions.^[228] Specifically, they developed accurate models to predict the rheological properties of agarose suspensions by elucidating (through micro compression) the deformation behaviour of agarose particles.^[228] This technique has been widely used to characterize spherical micro particles though it could be used to identify the Young's modulus of soft and deformable substrates.

Similarly, to the AFM, this micro-indentor deforms the solid surface using a tip and a force transducer. The tip in this instance is a thin glass rod made by heating and subsequent pulling of a glass capillary tube. Afterwards, the rod is polished, and a silicone based spherical probe is attached to its thin flat end. By using a camera and several precision micro actuators it is possible to navigate the probe towards the x, y and z axis with high accuracy over the sample stage. The glass probe is then attached to the force transducer (Model 406A, Aurora Scientific Inc., Canada), which detects the Nanonewtons of force applied to the sample in the Z axis. The transducer is connected to a PC-30D data logger (Amplicon Liveline, Brighton, UK) and a personal computer which records the signal force in terms of voltage (mV). Subsequently, the voltage is converted to force units and the displacement data are simultaneously recorded as movement in the Z-axis by the servomechanism that moves the transducer. The force-displacement curves are processed by fitting the hertz or Sneddon model depending on the indenter shape (spherical or conical respectively) resulting to the extraction of the Young's modulus value for each curve.

Confocal Laser Scanning Microscopy (CLSM)

Confocal laser scanning microscopy (CLSM), is an optical imaging technique commonly used to observe fluorescent particles in 3D structures. The main concept of confocal imaging relies on the improvement of existing traditional bright field fluorescent microscopes.^[229] A conventional fluorescent microscope excites evenly the whole specimen from a light source and as a result the fluorescence emission of both the sample and the unfocused background is detected by the microscope camera. On the other hand, a confocal microscope uses a spatial filter to block the light that is out of focus when it comes to image formation, making the optical resolution in the desired focal plane significantly better compared to the one of the wide field microscopes. Particularly, a laser beam goes through a spatial filter which is then focused to the desired area by an objective lens and the emitted photons from the fluorescent sample are collected pixel by pixel to build up an image. Also, its ability to capture multiple images on different levels, towards the Z axis of a sample, in order to make a three dimensional depiction of it, makes it a useful tool in the fields of materials science, biology, optics and crystallography.^[230] For example, it has been widely used to obtain cell images with different fluorescent stains on top or within the biomaterials that they are cultured, in order to acquire crucial information regarding the functionality of the cells. Pereira et al. developed gellan gum microparticles for therapeutic purposes in the intervertebral disc. To assess the novel hydrogel system aiming in the regeneration of IVD they loaded the material with lung fibroblast cell lines for 72 h of culture. Afterwards, they quantified the encapsulation ability of the particles by staining the cells with DAPI and phalloidin, but they also performed a live dead assay following confocal microscopy observations. Confocal imaging facilitated the process of obtaining a clear image (without a noisy background) of a single slice of a particle which

provided the group with valuable information regarding the biocompatibility and the viability of cells within the capsules.

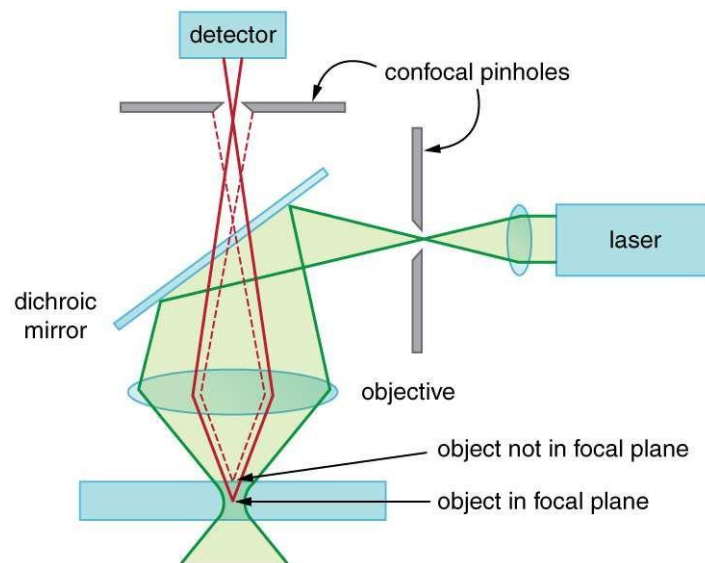


Figure 17: Working principle of Confocal Laser Scanning Microscopy.^[231]

X-Ray fluorescence (XRF)

X-Ray fluorescence spectrometry is a non-destructive, versatile tool mainly used to determine the elemental composition of materials. It is operated in quantitative and qualitative studies to analyse the major, minor and trace elements present in a sample in vacuum or ambient at both solid and liquid samples.^[232] The basic principle of the equipment is based on the emission of high energy X-rays to excite the atoms of the sample which subsequently emit characteristic photons of a certain amount of energy that can be correlated to the atomic number of each element present.^[233] In detail, the x-ray tube sends a beam to the atoms of the sample, exciting their electrons.^[234] It displaces them from the inner orbital shells by supplying them with energy higher than the binding energy that holds them in orbit.^[234] Subsequently, the lower orbits of the atoms are left vacant which makes them unstable, therefore electrons from the

higher orbits move down to fill those spaces, releasing energy.^[234] The amount of energy they emit is proportional to the energy difference between two different shells.^[235] This energy is detected by the equipment and is unique for each element of the periodic table.^[236] Finally, the quantity of each element present in the sample is calculated by the proportion of the total individual energies that appear, a method that nowadays is automatically conducted by the equipment's software.^[235, 236]

One of the main advantages of XRF is its non-invasive manner as it does not affect or disrupt the sample. The energy of the emitted and excited radiation is within the range of 1-115 keV. Therefore, it is used to detect elements on the surface of a material as its penetration depth is just a few microns for low atomic number elements and around 100 μm for heavier ones which varies depending on the type of sample.^[237] An XRF spectrometer is consisted of an excitation source, a sample stage and a detector which can be wavelength or energy dispersive. The excitation comes from the X-rays emitted by the X-ray tube. The intensity of the radiation is mainly dependent upon the applied voltage and the amplitude of the x-ray tube. The intensity and energy of the exciting photons which collide with the sample atoms defines the intensity of the detected fluorescence signal. Hence, there are multiple types of X-ray tubes ranging from 3 kW up to 18 kW depending on the application. The principle of an X-ray tube is a vacuum chamber with a cathode that emits electrons and an anode that collects them, establishing an electric current through the tube also known as beam.^[238] The electrons from the cathode collide with the anode and a portion of energy is radiated as X-rays with the rest released as heat.^[238]

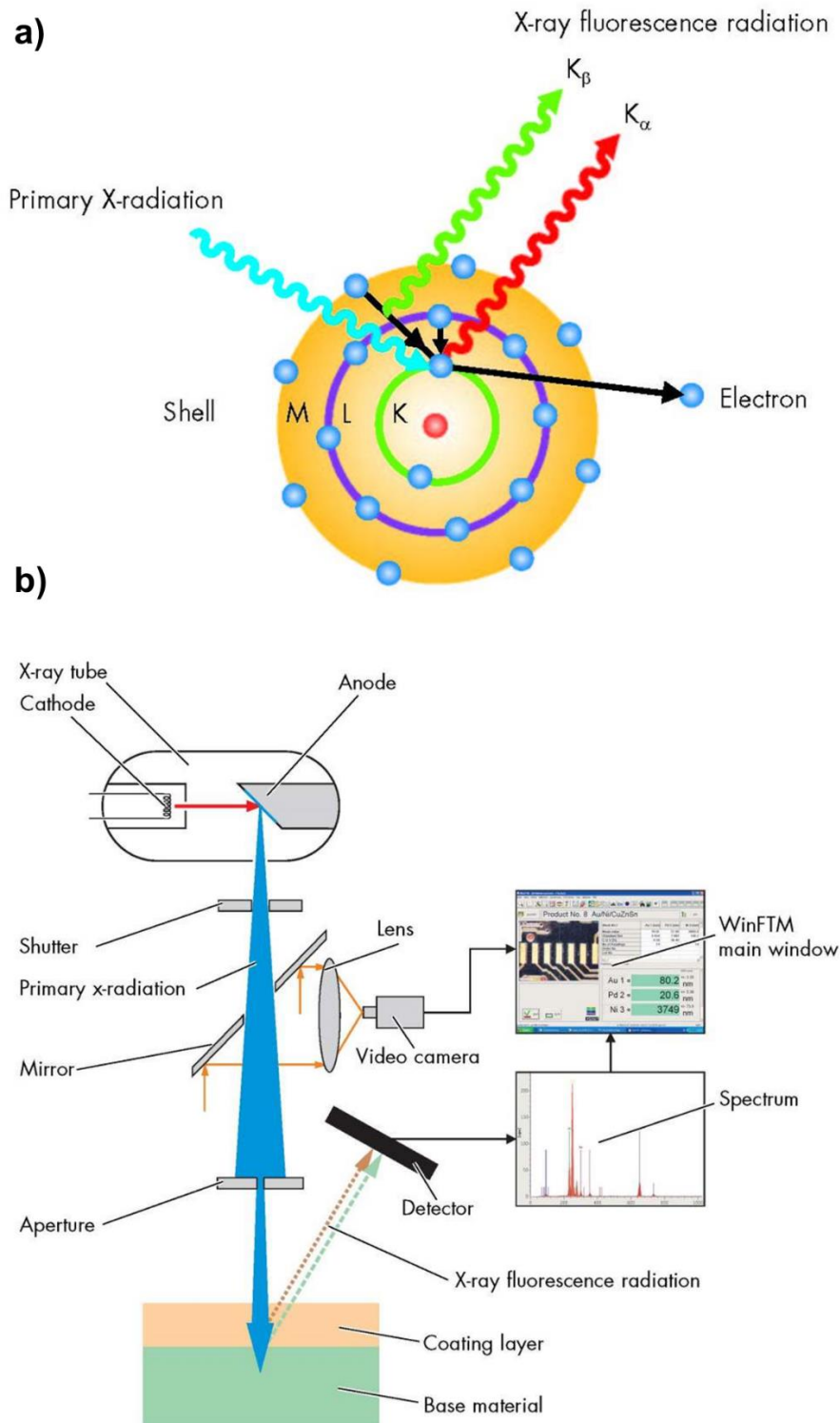


Figure 18: a) Principles of the electron excitation and the emission of fluorescence radiation, b) Schematic of an X-ray fluorescence equipment and its working principles.^[94]

There are multiple applications which require the analysis of the substrate and its breakdown into elements. Soil surveys,^[239] ceramic manufacturing,^[240] art objects (paintings),^[237] chemical and biological samples are only a few scientific areas where an XRF is employed.^[241] In the field of biomaterials it is often used to quantify the mineralization of the matrix from cells by detecting the minerals present on its surface. Mornet et al. have employed XRF to analyze the calcium deposits of human placental alkaline phosphatase found in bone to correlate it with tissue nonspecific alkaline phosphatase and build a three-dimensional model based on it.^[242] This model could then act as a probe to detect mutations in TNAP associated with hypophosphatasia, a rare disease which stems from defective bone mineralization.^[243]

Materials and methods

Materials

Gelzan™ CM, Poly(ethyleneimine) solution analytical standard 50 % (w/v) in H₂O, Minimum Essential Medium Eagle (Alpha Modification, with sodium bicarbonate, without L-glutamine, ribonucleosides and deoxyribonucleosides, liquid, sterile-filtered, suitable for cell culture), Fetal bovine serum (US origin sterile-filtered), Phosphate buffer saline (liquid, sterile-filtered, DPBS Modified 10X, without calcium, without magnesium, suitable for cell culture), L-glutamine, β-Glycerophosphate disodium salt hydrate (BioUltra, suitable for cell culture, suitable for plant cell culture, ≥99%) and Trypsin-EDTA solution (1x, sterile-filtered, BioReagent, suitable for cell culture, 0.5 g porcine trypsin and 0.2 g EDTA • 4Na per liter of Hanks' Balanced Salt Solution with phenol red) were purchased from Merck. Calcium chloride dehydrate 99% and Ethanol absolute ≥99.8% AnalaR NORMAPUR® were purchased from VWR International. Low melting point alloy (Bi 54%, Pb 28%, Sn 18%) was obtained as a free sample from 5N Plus, Germany. 9008 Series Borosilicate Glass Particles (8 μm diameter), Calcein-AM and Propidium Iodide (Invitrogen™) were purchased from Thermo Fisher Scientific. AFM All-In-One-Al tips were purchased from Budget Sensors.

Protocols

1. Device fabrication

A microfluidic device consisted of polydimethylsiloxane (Sylgard™ 184 Silicone Elastomer Kit, Dow Corning, UK) was fabricated using photolithography methods. The first step towards the creation of the device, is the design of the microchannels and their arrangement by using CAD software (Autodesk AutoCAD). The CAD design is then printed (by Microlithography Ltd, UK) on a photomask, which is actually an opaque sheet that allows light only to go through a defined pattern. It is commonly used in photolithography applications and especially in microfluidics, to form the microchannels on a substrate. The substrate that is normally used to build the negative mold, is a silicon wafer. The channels are formed by depositing a photoresist layer and employing the techniques of spin coating and photopolymerization. The process is usually conducted in a clean room using a UV lamp and a spin coater to shape the negative mold. The overall channel formation procedure goes as follows: a) the silicon wafer is placed on the spin coater and an epoxy-based photoresist (SU-8 2075, Permanent epoxy negative photoresist, MicroChem Corp., Westborough, USA) is poured over. b) The wafer is then rotated at a certain speed that defines the overall channel depth, for instance at 2000 rpm an overall coating of approximately 110 μm is formed. c) Upon the creation of a thin film of SU-8 on the wafer, the photomask is aligned with the wafer and the UV lamp. d) UV exposure of the wafer through the photomask for a certain amount of time to ensure fully polymerization of the photoresist. e) The unreacted resin residues are then washed away from the wafer using an SU-8 developer (1-methoxy-2-propanol acetate, MicroChem Corp., Westborough, USA) and the negative mold is ready to be used. With the

use of photolithography and especially the presence of a clean room, high resolution printing is achieved.

The reverse mold is repeatedly used to produce new microfluidic devices. PDMS silicone elastomer is a two-part component which occurs upon the mixing of the base with its curing agent at a 10:1 minimum ratio. Although, lower mixing ratios (such as 8:1 or 5:1) yield a stiffer final product and give a better polymerization throughout the polymer.^[244] The working time (pot life) of the mixture is 1.4 hours while the curing time at room temperature takes approximately 48 hours. To speed up the process a baking step is introduced which significantly lowers the curing time. Placing the mixture in the oven at 100 °C will yield a fully cured polymer in approximately 35 minutes.^[245] After mixing the base with the curing agent the mixture is poured onto the silicon wafer and the system is then transferred into the convection oven at a certain temperature (usually 70 – 100 °C) to accelerate the curing. Later, the system is removed from the oven and the PDMS is cross sectioned around the device design and peeled off carefully to avoid damaging the structure. An inlet and an outlet on every channel are required to be opened before sealing the device, using a biopsy puncher (Miltex Biopsy Punch with Plunger, Agar scientific Ltd., UK) with the standard 1.5 and 3 mm diameter depending on the application. The wider diameter is used to facilitate the injection of the joule heater that will be mentioned later on. In addition, a wide chamber is designed and cut off from the outlet of the main microchannel to facilitate the extraction of the hydrogels and prevent any possible deformation during the extraction process. The device is then sealed with a standard microscope glass slide (of 1 mm thickness) or another block of PDMS by the means of corona discharge. In order to create strong and irreversible bonds between the two materials a surface treatment with the corona discharge is required. This process is accelerated, and the bilayer becomes inseparable upon heating the system at around 100 °C for about 20 minutes. A hot plate is usually employed for that purpose.

There are two types of microfluidic devices that were tested for the two different materials used in the present research project. The principle of both devices, which derives from a previous study conducted by Vigolo et al.,^[161] is the application of thermophoresis to manipulate the (bio)material properties. In their study they introduced a novel design in which the main microchannel was surrounded by two side channels, one filled with a liquid epoxy to act as a joule heater and the other was used as a cold thermal source with water flowing through it.^[161] Similar to this device, the main part in both microfluidic designs of this project consisted of a main straight microchannel for loading the sample material and two side channels parallel to the main one to act as hot and cold thermal sources. The cold channel is filled with room temperature tap water flowing through it with the help of a syringe pump (Harvard Apparatus, Holliston, USA), whereas the hot channel is consisted by a joule heater made by a low melting point alloy (LMPA, MCP 96/Metspec 203 Alloy or Rose's "A" alloy, 5N Plus, Germany) with a melting point of 90 °C. In contrast with the liquid epoxy the main advantage of the LMPA, consisted of Bi 54%, Pb 28%, Sn 18%, is the uniformity of the temperature across its surface but it can also reach higher temperatures. Once the microfluidic device is sealed onto a glass slide, it is placed on a hot plate at 130 °C and small fragments of the LMPA were placed at the inlet of the hot channel. After a while, when the overall temperature of the device is above 90 °C, the alloy melts and it's injected through the hot channel until it's filled. The device is then cooled down slowly at room temperature to solidify the LMPA and prevent a thermal shock to it which will result in the cracking of the material. Meanwhile two copper wires are dipped at the inlet and the outlet of the hot channel to later connect the joule heater to a power supply. To further protect the joule heater from breaking, the two wires are also glued to the device by using a two part epoxy glue (Araldite Epoxy Adhesive, RS components, Corby, UK) as the device is only a few microns deep and the

metallic strip is extremely vulnerable to external vibrations. The microfluidic device fabrication process is then completed and further assembly with other components is following depending on the material.

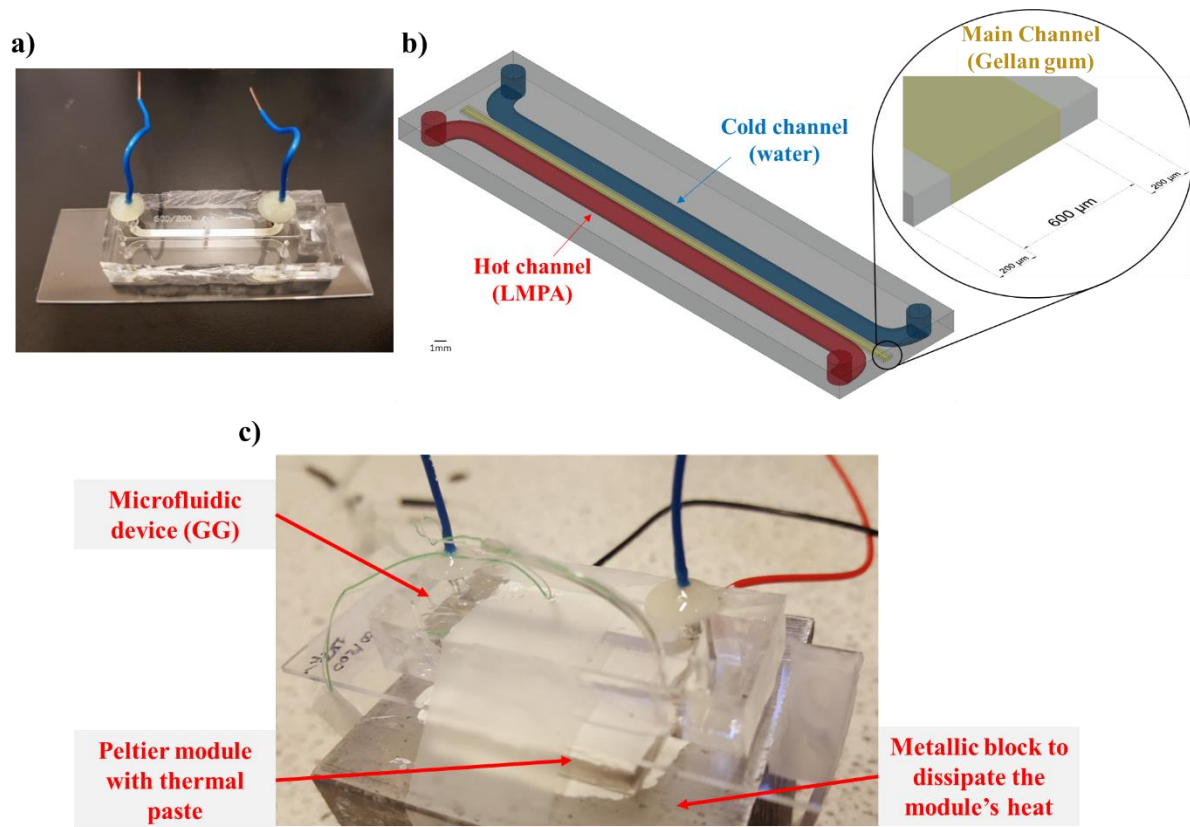


Figure 19: a) Picture of the microfluidic device used for the gellan gum, b) Schematic of the channel's arrangement in the microfluidic device, c) Picture of the assembly of the device with the Peltier module.

In the case of gellan gum, the overall system should work on a temperature beyond the gelling point of the material ($\sim 35\text{ }^{\circ}\text{C}$) to maintain a liquid and relatively low viscous state. In a low viscosity state, gellan fibres will migrate faster compared to a higher one as they encounter minor drag force which acts in the opposite direction of the thermophoretic force applied to the molecules by thermophoresis. Nevertheless, at the same time the system needs

to be able to be cooled down rapidly during the polymerization process in order to avoid any disruptions to the gradient. Once the temperature gradient is no longer applied, the phenomenon of thermophoresis is not having any effect to the GG coils and as a result they will tend to migrate towards the opposite side to restore the concentration balance within the gellan mixture in the microfluidic channel.

The microfluidic device is mounted onto a Peltier module (58.6 W, 6 A, 15.7 V, 40 x 40 mm, RS components, Corby, UK) with the addition of a thermal component between the ceramic plate and the glass slide of the device for improving the overall heat transfer. In addition, a solid metal block is placed underneath the Peltier module to dissipate the heat that is generated from the other side of the module (Figure 19c). Both the joule heater and the Peltier module are then connected to a power supply which supplies them with an electric current and voltage. These settings could be later adjusted to reach the desired temperature output in both components.

Regarding the sodium alginate case, a quite different microfluidic design was used as the polymerization process between the two materials significantly varies. The main part including the middle channel for the biomaterial and two side channels one for the hot (joule heater) and one for the cooling water flow remains practically the same. However, that PDMS part is not sealed onto a standard microscope glass slide but instead a thin PDMS membrane is used for this purpose. Sodium alginate can be cross-linked with the addition of monovalent or divalent cations, after the gel powder is dissolved in deionized water. For example, when a droplet of NaAlg interacts with a droplet of CaCl_2 a clear and durable gel is formed within a few seconds after the initial contact. In contrast with GG solution, the polymerization of NaAlg is not temperature dependent but solely depends on the cross-linking ion concentration in the mixture. Therefore, a mechanism of slow addition of calcium had to be implemented in order to polymerize NaAlg in the main microchannel, especially after the application of thermophoresis

for a certain amount of time. A challenging procedure as the calcium ions will immediately cross-link the NaAlg solution but at the same time the injection of CaCl_2 in the confined space of the microfluidic channel is almost impossible. For this reason, a sandwich like device was designed with the top part being the main one similar to the GG device, a thin PDMS membrane in the middle and a channel aligned with the main one at the bottom below the membrane. To cross-link the alginate, calcium carbonate nanoparticles were evenly dispersed to the initial NaAlg solution and later dissolved with the decrease of the pH of it. It is well known that CaCO_3 particles will not dissolve when mixed with pH 7 water unless the solution becomes acidic and the pH is significantly lowered. With this method we create a stock of undissolved calcium molecules which will dissolve and subsequently polymerize the material when the pH of the alginic solution is lowered. For that reason the bottom channel which is aligned with the main micro channel, is used for the flow of an acidic solution that will slowly diffuse through the thin PDMS membrane and as a result the NaAlg solution will slowly polymerize with the release of Ca^{+2} ions from the gradual dissolution of CaCO_3 nanoparticles. Though there are two major issues with this microfluidic setup. Firstly, the PDMS membrane should be thin enough to allow a rapid diffusion of the acidic solution. Also, the fact that PDMS is not permeable to water does not allow the use of aqueous solutions at the bottom channel. To address these problems a spin coater (Polos SPIN150i) was employed to produce a thin layer of PDMS to act as the middle membrane and also an acidic oil (Merck, UK) was used to facilitate the diffusion through the PDMS membrane and initiate the polymerization of NaAlg. The spin coating of PDMS was performed over a standard microscope glass slide (1 mm thickness) and the thickness of the membrane was determined by the speed of the coater. In this case 500 rpm maximum speed for 30 seconds were used to yield a PDMS layer of 250 μm thickness. The coated glass slides were cured on top of a hot plate at 100 °C for 45 minutes, followed by corona (plasma) treatment and a bonding of the two surfaces similar to the glass-

PDMS system as previously described. Afterwards, the hot channel is filled with the LMPA as shown above to form the joule heater in the top part of the device. Then, the sealed device is peeled off the glass slide slowly to remove the membrane from the slide and at the same time to prepare for the attachment of the bottom part. The single channel bottom device is then attached to the other (free) side of the membrane via corona treatment as well, resulting to the creation of the sandwich like device.

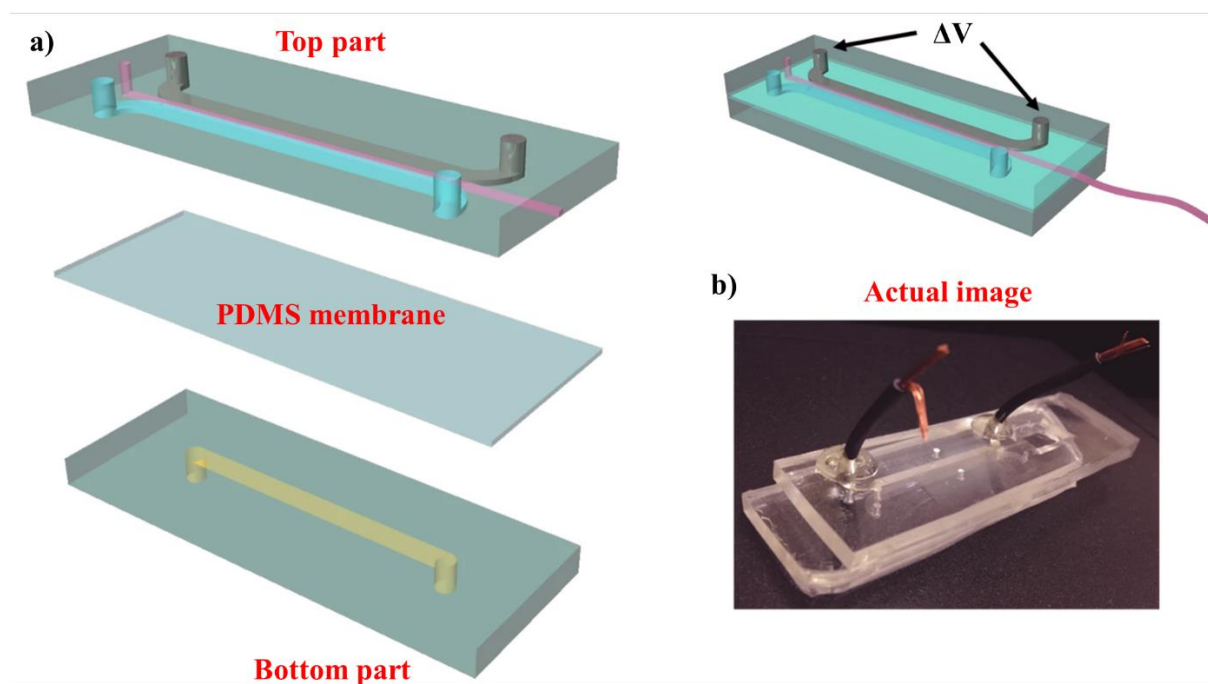


Figure 20: a) Schematic of the two-layer device. Top part is used for the manipulation of the mechanical properties of biomaterials, middle part is a PDMS oil and gas permeable membrane and bottom part is used for the polymerization of NaALG in the main microchannel by the infusion of an acidic oil to reduce the pH of the solution. (b) Picture of the 8cm long microfluidic device.^[246]

2. Biomaterial fabrication process

A. Gellan gum

A mixture of 1% w/v GG (Gelzan™ CM, Merck, UK) is prepared before injection in the microfluidic device. Usually, 0.1 g of Gelzan powder is slowly dissolved in 9.5 mL of deionized water on a hot plate under continuous heating and stirring. The overall mixture temperature is above 70 °C to ensure complete dissolution of the gellan powder and avoid having aggregates or larger particles dispersed in the mixture. Heating, above the gelling point ~35 °C also keeps the GG mixture at a relatively low viscosity state (around 10 cP) and facilitates dissolution (Figure 21).^[247]

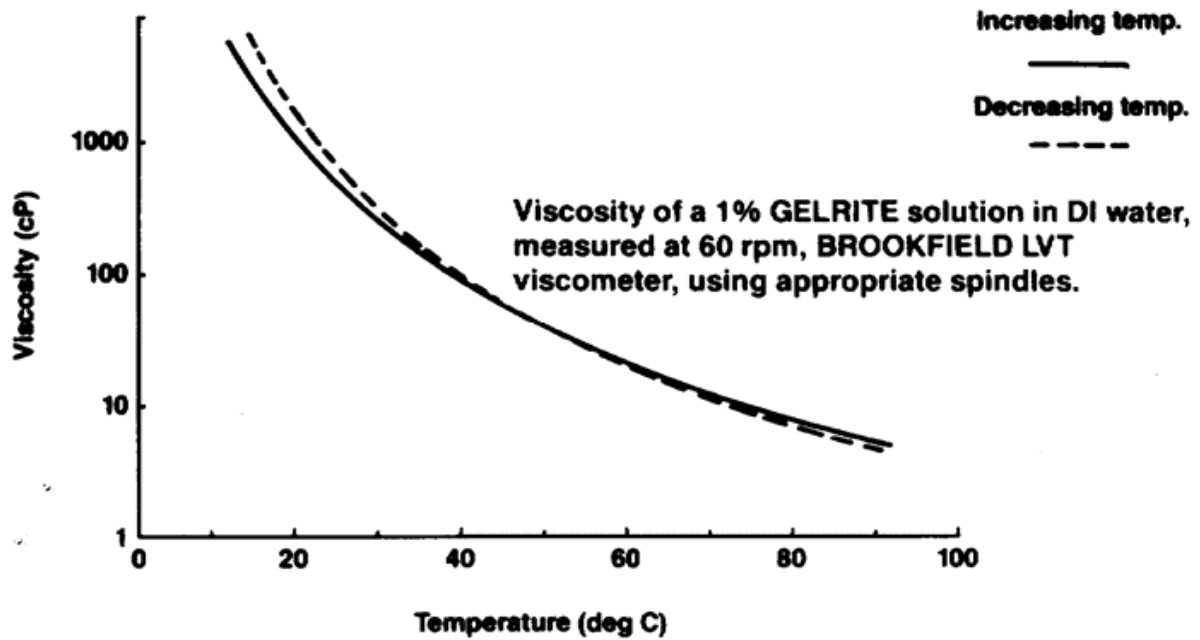


Figure 21: Low-acyl gellan gum viscosity change as a function of temperature for a solution of 1% w/v GG.^[247]

After 30 minutes the powder is completely dissolved, and the cross linker is added to the solution. The cross-linker in this case is an aqueous solution of CaCl_2 which was prepared with the addition of 1.47 g of CaCl_2 powder (Calcium chloride dehydrate, Merck, UK) in 100 mL deionized water to form a 100 mM CaCl_2 solution. 0.5 mL of the CaCl_2 solution are added slowly to the GG mixture with a pipette drop by drop to avoid local gelation beads that might be formed due to the temperature difference of the two solutions. That amount will result at a final CaCl_2 concentration of 5 mM in the GG mixture.

Meanwhile, the microfluidic setup is connected to the power supply, both the joule heater and the Peltier module. The temperature profiles of the hot, cold and the thermoelectric module are monitored throughout the experiment with the use of K-type thermocouples (Labfacility Z2-K-3M Series, Farnell, UK) and a USB data acquisition board (National instruments, USA) connected to the computer in order to log the data. The software used to monitor the process is

NI SignalExpress 2014 (National Instruments, UK). After the pre-heating of the device the flow of cold water starts to reach a steady state in the device temperatures between the main and the 2 side channels. Tap water is used to flow through the cold channel with the help of a syringe pump (Harvard Apparatus PhD 2000 Dual Infusion Syringe Pump, Harvard Apparatus, UK). A 60 mL syringe is mounted onto the pump to ensure the flow of the water throughout the duration of the experiment. The flowrate of the water ranges from 300 to 500 μL per minute with an initial setup of 350 $\mu\text{L}/\text{minute}$. The initial temperature profiles range around 55-58 $^{\circ}\text{C}$ for the cold channel, 69-72 $^{\circ}\text{C}$ for the hot channel and an average temperature of around 62-64 $^{\circ}\text{C}$ is maintained from the Peltier module. After the initial setup of the device, the injection of GG follows up.

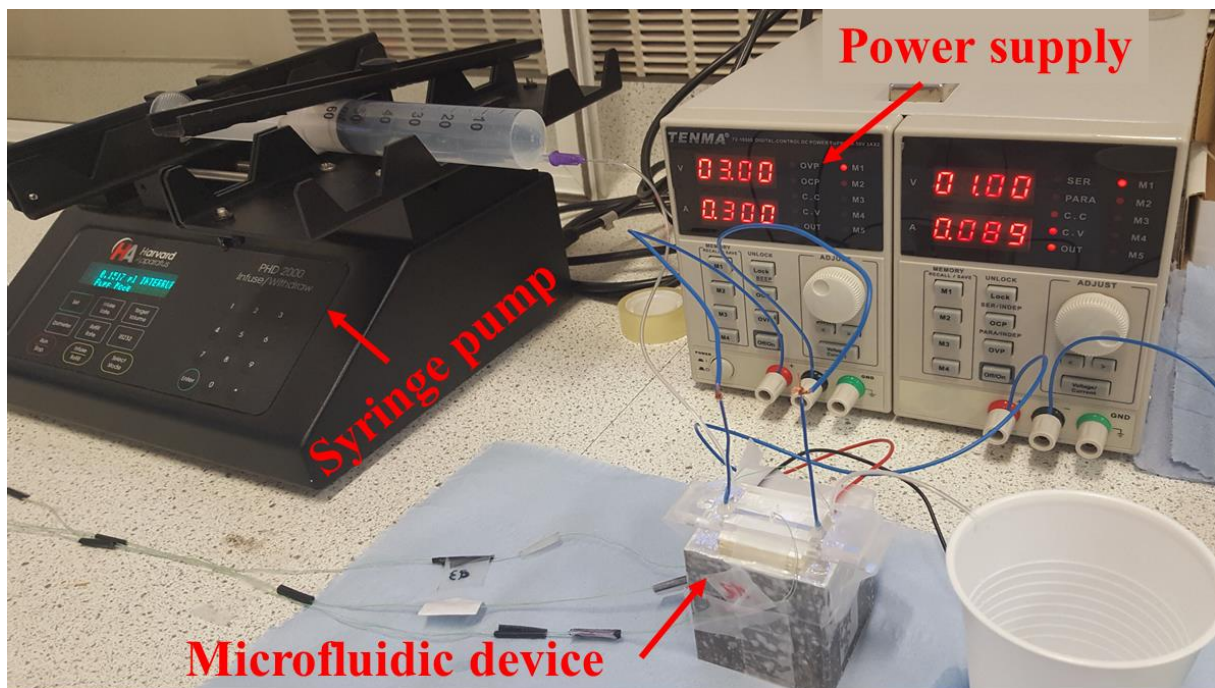


Figure 22: Picture of the microfluidic device setup for the gellan gum case. A syringe pump is used to flow the cold tap water on the “cold” channel, a power supply controls the current (and subsequently the temperature) of the peltier module and the Joule heater.

The inlet of the microfluidic device is extended using microfluidic tubing to facilitate injection and ensure proper fitting between the needle of the syringe and the inlet of the device. Following the preparation of the device, the GG mixture is injected into the microfluidic device by rapidly transferring the solution to a syringe and then to the main microchannel. To ensure that the channel is fully filled and to potentially insulate the system's inlet and outlet, the polymer is injected up to the point where the water bath outlet is filled with the GG solution. The inlet is also filled with the hydrogel which its rapidly gelled at both ends. In that way a physical barrier prevents the liquid GG mixture to escape from the main micro-channel.

Convection is present in the main channel as the temperature gradient induces a density gradient across the width of the channel. Therefore, the part that is closer to the hot side will recirculate towards the cold side and as a result the gellan molecules that migrated due to thermophoresis will be interrupted by it. For that reason, the device is rotated 90° with the hot channel at the top and the cold one at the lower part of the setup. Consequently, the least dense part (hot) is maintained at the top to prevent mixing with the lower (colder) part.

Following the injection of GG, in the pre-heated device, the application of the temperature gradient takes place. The temperature difference between the two channels (hot and cold) is maintained for a specified amount of time, that ranges from 20 to 40 minutes, until the concentration gradient on the hydrogel is formed. After forming the desired concentration gradient of GG in the main channel, a rapid polymerization should take place in order to avoid GG coils migrating backwards. Once the temperature gradient is halted, the GG solution will tend to disrupt the concentration gradient and restore the concentration balance by allowing the high concentration part to move towards the low one. Therefore, the Peltier module is converted from a heat pump to a cooling device by simply reversing the polarity between the power supply and the module. The temperature drops from 64 °C to 0 °C in less than a minute and is kept there for at least 15 minutes to ensure the complete gelation of the biomaterial.

Since the material is rapidly gelled, the concentration gradient is maintained, and we assume that it translates into a stiffness gradient as we move from a liquid to a solid material state.

The final steps are the extraction and storage of the material. To extract the fiber from the microfluidic device the removal of the excess polymer at the inlet and the outlet of the device is mandatory. Afterwards, using a syringe we gently push the material to the water bath at the outlet using air or deionized water in order to prevent any deformation or breakup to the biomaterial. The fiber is then extracted to the water bath and collected with a fine point tweezer. Finally, the material is stored in a petri dish full of deionized water at 4 °C to significantly slow down bacterial growth in the petri dish, as we are working in non-sterile conditions.

B. Sodium Alginate

Similarly, to the GG case described above, a 2% NaAlg solution is prepared in a beaker on a hot plate under stirring for 30 minutes. A calcium carbonate nanoparticles suspension is prepared using deionized water at a concentration of 100 mM. The final solution is consisted of 5 mL of 2% NaAlg solution with the addition of 2.2 mL of nano CaCO₃ 100 mM suspension and 2.8 mL of deionized water to reach a total volume of 10 mL. The concentrations of the final solution are 1% of NaAlg and 22 mM of nCaCO₃. The calcium carbonate nanoparticles are suspended within the solution and dissolved only when the acidic solution lowers the pH in the main microchannel to initiate the cross-linking of the material. The concentration of the nanoparticles was selected at 22 mM based on the article of Amici et al. who studied the gelation of sodium alginate drops in a microfluidic T-junction at different flow regimes and further optimized the process.^[248]

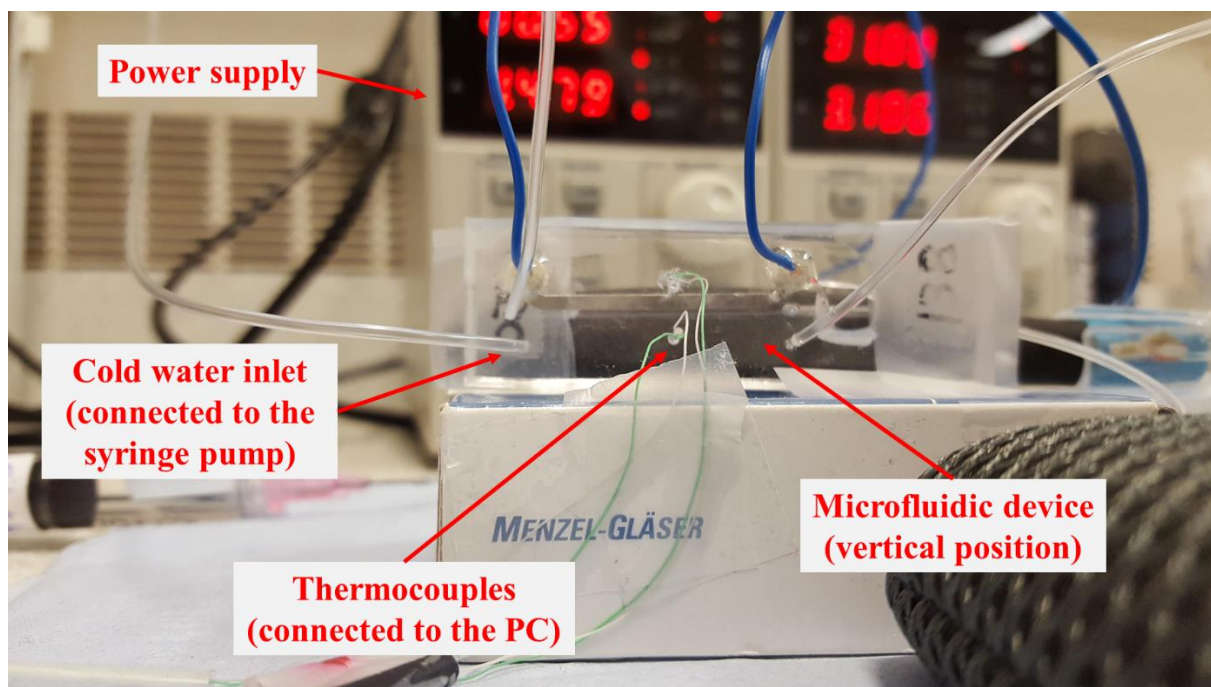


Figure 23: Picture of the sodium alginate (sandwich like) microfluidic device. The power supply controls the current of the Joule heater, the “cold” channel is supplied by a syringe pump, thermocouples monitor the hot and cold channel temperatures.

Similar to the gellan gum process, the joule heater of the device is connected to the power supply to initiate the generation of heat at the “hot” channel and the syringe pump is connected to the inlet and outlet of the “cold” channel to start the flow of the cooling water (Figure 23). In that case there is no peltier module as no external heating is required and the average temperature of the device is around 25 °C. The NaAlg solution is injected into the main microchannel of the sandwich like device and the flow is halted. The temperature gradient is applied for 20 to 30 minutes with the hot channel operating at a range from 27 to 33 °C and the cold one ranges from 22 to 24 °C. The flowrate of the water ranges from 300 to 400 μL per minute with an initial setup of 320 $\mu\text{L}/\text{minute}$. Upon the application of the temperature gradient and the formation of the concentration gradient to the NaAlg mixture, the gelation phase takes place. The temperature gradient is maintained in that case during the polymerization to prevent

any alginate molecules from migrating back and disrupting the gradient. The acidic solution which is consisted of 5% v/v acetic acid in silicone oil, is then used to fill the bottom channel which is located underneath the main microchannel on the other side of the thin PDMS membrane (fig. 20a). The oil is slowly diffusing through the membrane to the NaAlg solution, lowers the pH of the solution thus resulting in the dissolution of the CaCO_3 nanoparticles. Subsequently the free calcium ions Ca^{+2} in the NaAlg solution act as cross linking agents which form ionic bridges between the saccharide chains of the alginate.^[249] After at least 15 minutes of gelation, the joule heater as well as the syringe pump are turned off and the material is extracted by gently pushing the hydrogel out of the main channel using air or deionized water. The material is extracted at the water bath situated in the outlet of the device which is filled with CaCl_2 solution to ensure that the gel is fully gelled. Using a fine point tweezer, the fiber is transferred at a petri dish filled with deionized water to prevent any dehydration of the hydrogel. Finally, the material is stored at 4 °C.

3. Material storage

The materials were stored inside a petri dish filled with deionized water at a low temperature environment to prevent or impede bacterial growth. However, there are several issues in the material characterization part. When stored in deionized water, the hydrogel is floating at the surface and is often found in a tangled state which makes it difficult to recover using tweezers. In addition, the material is both transparent and 600 microns wide which makes it even harder to retrieve from the petri dish and there is a high risk of deforming or breaking it during the extraction. For this reason, the material is fixed on a supportive glass slide to

facilitate imaging and transferring. The glass slides were specifically modified to be able to attract and firmly grip the material to their surface.

Normal microscope glass slides (1 mm) were cut into smaller pieces according to the material length. Afterwards, they were washed with soap and water to clean them, followed by washing with deionized water and ethanol which was then evaporated. In that way the slides were perfectly clean and free from any dust or particles that was deposited previously in their surface. The next step was to corona treat the slides for 1 minute using the corona discharge device. In this way a negative charge was created to the surface of the slides. Afterwards, the negative charged glass slides are placed into an amine solution (Poly(ethyleneimine) (PEI) solution ~50% in H₂O, Merck, UK) for at least 20 minutes. The PEI solution is a 1% w/v and it's used to slowly replace the free hydroxyl groups (-OH) in the surface of glass, created by the plasma treatment, with amine groups (-NH₂). In that way, the negative charged glass surface turns into positive and strongly attracts negative charged surfaces such as several biological tissues. A typical example of this method is the application of a Poly-L-Lysine coating in surfaces to attach different types of cells for studying their properties.^[250] Poly-L-lysine, is a biopolymer well known for its cationic nature which makes it a suitable coating for adhering negatively charged biomolecules. PLL coatings are ideal for the adhesion of cells, since it is well known that the cell membrane is negatively charged.^[251] In our case, as the PLL coating attraction is too strong and might affect cell response afterwards, the more mild coating of PEI was preferred. The fabricated biomaterials upon extraction were placed onto the PEI coated glass slides which were first washed with deionized water and then left to dry to remove any water content that might affect the bonding. The material is attached to the slides with a firm grip which does not allow any movement, an important factor for the sensitive AFM evaluation later on. The biomaterial-slide system is then placed on a petri dish and filled with deionized water to prevent the dehydration of the material.

Material Characterization

1. Atomic force microscopy (AFM)

The first and most important step in the characterization of the fabricated biomaterials is the evaluation of the elasticity of their substrate. Two methods to evaluate locally the stiffness of the substrate across a 600 μm wide fiber with great accuracy and sensitivity were employed. Atomic force microscopy (AFM) and the micro-indentation technique developed on site by Prof. Zhang, were used to carry out this task. The delicate technique of AFM was used to identify the stiffness of the hydrogel locally to evaluate the stiffness gradient across the fibers. With the micro-manipulation technique, we obtained useful data regarding the stiffness of rougher surfaces of the biomaterials which was difficult to achieve using the AFM due to the high sensitivity of its tip.

A. Cantilever selection

One of the main problems faced in the early stages of the stiffness tests, was the deformation of the hydrogels during the tapping of the substrate by the AFM cantilever. Conventional cantilevers are usually sharp which serve best the purpose of imaging of a material surface. As the stiffness of the novel biomaterials was expected to be in the range of kPa, applying force for determining the deformation of their surface with such a tip will potentially damage the substrate, resulting also in an inaccurate measurement. In order to prevent those ruptures to the material surface, a blunt or spherical tip should be used. For that reason, we constructed a cantilever with a spherical probe attached to the tip. The cantilevers used were tip-less for allowing the attachment of the colloidal probe, with an aluminium

coating on the reflective surface to enhance the laser signal (All-In-One-Al-Tipless, BudgetSensors[®], Bulgaria). The probe that was used for the force measurements was a borosilicate glass sphere of 8 μm in diameter (Thermo Scientific[™] 9000 Series Glass Particle Standards, ThermoFisher Scientific, UK). In order to stick the glass spheres to the tip a 2-part epoxy glue was used (Araldite[®] Rapid, Go-Araldite, Switzerland). To assemble these 3 parts and make the final spherical tip a micromanipulation setup was utilized, owned by Professor Zhang at the University of Birmingham.^[224, 225] The rig was consisted of a glass stage where the silica particles were loaded, a custom-made adhesive head to attach the cantilever, a camera feeding the live image to a monitor and several high precision actuators. The process of attaching the probe is quite straightforward but requires a high level of accuracy and fast response in a timely manner as it is also a time dependent process.

The first step is to mix the two epoxy parts to initiate the polymerization of the glue. The viscosity of the epoxy glue is increasing exponentially over time therefore at approximately 5 minutes after mixing in room temperature the mixture starts to solidify. For that reason, the attachment of the probe becomes a time dependent process as mentioned before. After 3 minutes of mixing a tiny droplet of the glue is applied to the stage close to the cantilever tip. The tip should be already focused by the camera and aligned with the stage to be ready for the glue. After aligning the tip with the glue droplet and the stage a rapid dipping of the tip to the glue will result at the formation of a micron size droplet of glue at the bottom of the tip (the sample surface). Before the glue dries out and becomes solid (after 5 minutes) the tip is aligned with a spherical probe on the stage and it is glued with it. Finally, the tip is inverted and left to rest for at least 24 h to ensure the fully curing of the glue and the successful attachment of the spherical probe to it.

Likewise, the micro-indentor tip is created with a procedure similar to the AFM cantilever. The tip is made out of a thin glass capillary tube which heated and pulled before

eventually splitting in 2 parts. Afterwards, the thinner part is selected to be polished, using a rotating polyester disc with high accuracy using micro-actuators and a 10x magnification lens. The goal was to create a flat surface 8 to 20 microns in diameter to accommodate the spherical part of the tip. The latter is consisted by a borosilicate glass sphere of 8 μm in diameter (Thermo Scientific™ 9000 Series Glass Particle Standards, ThermoFisher Scientific, UK). Once the tip is polished it is attached to the micromanipulator transducer by using superglue (RS PRO 3 g Super Glue, RS components, UK). Using the cameras and the micro-actuators of the rig, the polished part of the tip is attached to the 8 μm sphere in the same way as the AFM cantilever (mentioned above). The tip is then left for at least 24 hours in vertical position to ensure the fully curing of the epoxy glue and the attachment of the borosilicate sphere.

B. Young's Modulus evaluation

The glass slide that supports the material should be attached firmly (using a double-sided tape) to the petri dish to avoid any movement during the AFM probing. In addition, the petri dish should be filled with deionized water to prevent the dehydration of the biomaterial. Following the sample preparation is the calibration of the equipment, with the AFM mode to be set at contact mode and force spectroscopy. The tip is loaded onto the supportive glass specifically made for measurements in liquid and its fixed in its special socket under the AFM head. It is then calibrated to align the laser on its reflective surface and adjust its spring constant, its resonance frequency, and its sensitivity. Then the cantilever stage is moving down towards the water surface where a second adjustment needed to be made in the laser alignment, due to the refraction of the laser beam. The tip is moving slowly towards the sample surface after another alignment of the tip with the substrate using the camera present. Once the tip has reached the biomaterial surface the evaluation of Young's Modulus locally takes place.

The Young's modulus of the substrate was evaluated locally in 4 different areas across the 600 μm wide fiber to ascertain the existence of a stiffness gradient along that direction. The measurements were conducted at 4 equally spaced locations across the width of the substrate, taking care to avoid the very edges to avoid any misrepresentation of the stiffness due to the friction experienced by the material during the extrusion stage.

Initially, each measurement consisted of a rectangular grid 100 μm long and 30 μm wide including 25 points (5×5) of equal distance between them. A grid consisting of 25 contact points provide us with a sample of total 100 points across the surface that could be considered as statistically adequate. Each spot represents an indentation created by the tip which approaches the surface with a force of 100 nN and applies a force of 50 nN to the substrate. In due course these area grids were reduced to $20 \times 20 \mu\text{m}$ due to the fact that stiffness greatly increases across the distance of 100 μm which subsequently upsurges the inconsistency of the measurements (Figure 24). Also, a $20 \times 20 \mu\text{m}$ area gives plenty of room to the 8 μm spherical tip to conduct measurements that do not overlap and subsequently it allows the deformed gel to recover before the next indentation. The latter was also validated by observing the deformation and recovery time of the sample under the micro-indentor of Prof. Zhang. After the indentation measurement, the substrate slowly recovers within seconds though in AFM a high repeatability of the measurements might not allow the substrate to recover thus resulting to an experimental error. These 4 measurements across the fiber's width represent only one part of the biomaterial thus a replication of these measurements in two to three other areas is necessary to ensure that the gradient is uniform throughout the fiber.

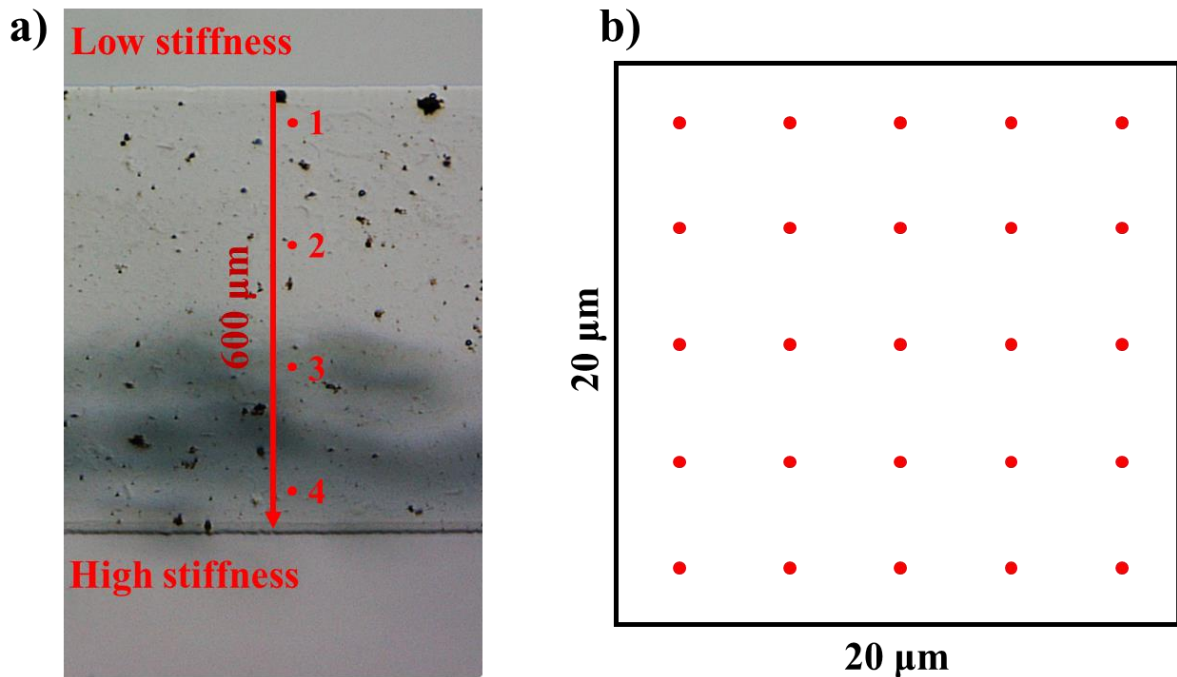


Figure 24: a) 4 spots across the 600 μm wide fiber of local AFM indentation measurements, b) Area (20x20 μm) of each spot containing 25 contact points.

The data obtained by the AFM are force versus displacement curves for each one of the spots. A further analysis is needed by the data processing software provided by JPK in order to extract the Young's modulus values from each one. The curves are then translated into stiffness by setting the radius of the glass probe, which was 4 μm as we used the custom made 8 μm borosilicate sphere tips, and the Poisson ratio. Poisson's ratio in biomaterials describes the degree of contraction or expansion of the scaffold in the transverse direction.^[252] Typically, for soft biological samples, such as hydrogels Poisson's ratio is assumed to be positive and around 0.5 as they consist by 99% of water which is incompressible and its volume remains practically the same when stress is applied.^[253] One of the most important parameters which is set during the data processing is the selection of the right model to be fitted in the curves. As the tip used in this project is spherical, the Hertz model is selected to be the appropriate fit for the force/displacement curves. Afterwards, the data points were averaged to give us an overview

of the stiffness of each area so they can be later plotted to illustrate the stiffness gradient across the material width.

The data extraction using the micro-indenter is similar to the AFM with a calibration step followed by subsequent 4 local measurements across the width of the fiber. Once the data are extracted and the force-displacement curves are plotted, the Hertz model is applied using MATLAB software, as no automated data processing software exists for the custom-made micromanipulation rig.

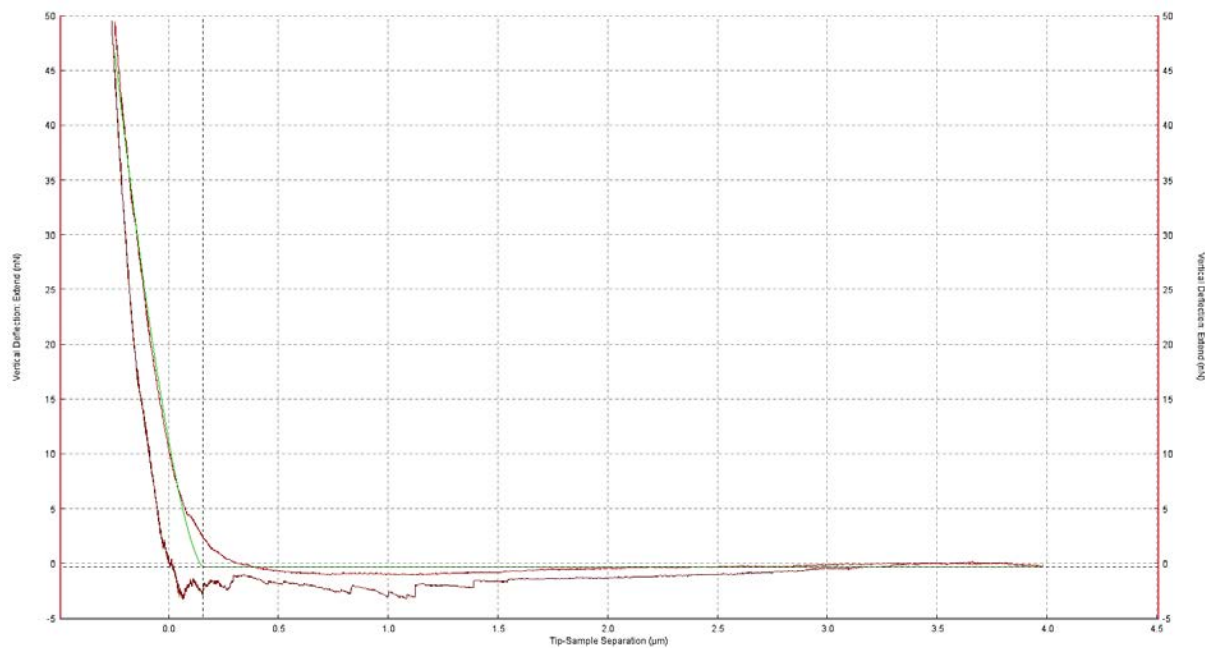


Figure 25: Force - displacement curve fitting on the JPK nanowizard software. Green colour curve represents the Hertz model fit, red curve represents the approach and purple one the retract movement of the piezo at the substrate.

The Hertz model best describes the contact of two “curved” surfaces and the slight deformation of one of them under a certain amount of stress applied.^[254] The amount of deformation is dependent of the Young’s modulus or elastic modulus (E) of the materials in contact.^[255] The Hertz model is based on several assumptions made such as:^[256]

- a. The sample is considered an isotropic and linear elastic solid.

- b. The indenter is not deformable, and no further interactions occur between the indenter and the sample.
- c. The contact area is smaller than the dimensions of the two bodies that come into contact.

Since these conditions are met the model can be fitted into the force/displacement curves to extract the Young's Modulus value for each curve. However, in Hertz's model there are several equations that each describes better the contact depending on the geometry of the indenter. In our case the tip is spherical but the corresponding equation was not used as the parabolic model is often used for spheres due to the fact that the approximation of the tip shape is reasonable for small indentations and also the fit is easier.^[257]

$$F = \frac{4\sqrt{R_c}}{3} \frac{E}{(1-\nu^2)} \delta^{3/2}$$

Where F: Force (N), δ : displacement (m), RC: Tip radius (m), E: Young's Modulus (Pa) and ν : Poisson's ratio.^[256]

The next step in the material characterization was to understand the mechanism behind the stiffness gradient. The AFM evaluation of Young's Modulus verifies the existence of a stiffness gradient, but we cannot be certain about the reason that this gradient formed. In theory, the temperature gradient applied to the hydrogel mixture in the microfluidic device induces a concentration gradient to the liquid phase which was later translated into a stiffness gradient via the rapid polymerization of the material.^[246] Unfortunately, this cannot be confirmed only by the AFM results, as they show the existence of a stiffness gradient but they do not reveal the mechanism that led to it.

2. Scanning electron microscopy (SEM)

An SEM imaging process on the surface of the fiber was conducted to better understand the structure and confirm the concentration gradient of the hydrogel molecules that led to the stiffness gradient of the biomaterial.

A. Sample preparation

In order to perform an SEM imaging, the material should be in a solid state as most of the SEM instruments operate under vacuum. In general, a gel and especially a hydrogel is mainly considered as a liquid dispersed in a continuous solid phase.^[64] That of course generates the problem of removing all the liquid content from a hydrogel which is consisted of 99% of water. A common practice applied to this problem is to convert the hydrogel into an aerogel. Aerogels are synthetic porous materials derived from gels which had previously replaced their liquid content with a gas. However, it is a complex process which requires several steps in order to remove all the water content and at the same time maintain the structure and the surface characteristics of the material.

There are two principal methods most commonly used for the preparation of aerogels from a hydrogel.^[258] The first one is lyophilization (also known as freeze drying), a popular technique in food industry, which involves the freezing of the material and the subsequent sublimation of ice under vacuum.^[259] This method requires the rapid freezing of the material with liquid nitrogen or dry ice otherwise the water molecules of the hydrogel will deform the material as they solidify and expand (forming large ice crystals).^[260] Therefore, the faster the freezing process the less deformed the material will be. Afterwards, a freeze dryer will slowly (time depends on the volume of water that needs to be sublimated) remove all the water content,

converting the hydrogel into an aerogel.^[259] The second method is supercritical drying using CO₂.^[261] This method is considered to be advantageous as it minimizes the shrinkage of the material which is related to the surface tension effect.^[261] Although, the main issue here is the requirement of an intermediate stage of solvent exchange which should be done gradually otherwise the difference in surface tension between the water and the organic solvent will damage the structure of the material.^[262]

B. Supercritical CO₂ and SEM imaging

As a better option the supercritical CO₂ method was preferred. The material (1% Gellan gum) was placed in 0.5 mL of deionized water and a syringe pump (Harvard Apparatus, Holliston, USA) was employed to infuse ethanol (Ethanol absolute \geq 99.8%, VWR, UK) at a rate of 0.5 μ L/hr for 24 hrs. Later, the material was transferred in specimen capsules (78 μ m pore size, Agar Scientific) and dried by supercritical CO₂ (Quorum E3100 critical point dryer, Quorum Technologies, UK). The fibers were flushed 4 to 5 times with liquid CO₂ and incubated for 15 minutes in between. The fibers were then sputter-coated with 15 nm iridium (Qorum K575X, Quorum Technologies, UK) and then observed under scanning electron microscope (FEI Verios 460, Thermo Fisher Scientific, UK) at 2 KeV and 25-50 pA probe current. The processes of both the supercritical CO₂ drying and the SEM imaging were carried out at the chemistry department of the University of Cambridge by Dr. Yi Shen.

Once the SEM images of dried fibers were obtained, they were processed by the ImageJ software to extract the approximated porosity values for each section of the material. At first, the images were calibrated using the scale from the original SEM images. The pictures were then converted into an 8-Bit format, then into binary images (black and white) followed by a

fine tuning to the threshold applied to them by the software. Following the image conversion, we set the parameters of the “Analyze particles” plugin by adjusting the scale/pixel ratio and setting the upper and lower limits for the size of the pores. In addition, the watershed function of ImageJ software was employed to smoothen the rough edges and improve the circularity of the pores. Subsequently, the measurements of the total area as well as the average size of the pores was conducted for each picture which correspond to a specific area of the hydrogel.

Biological experiments

1. Mammalian cell cultures

A. Cell culture preparation

The biological tests were conducted using mammalian cells, with all the work taking place under a laminar flow hood, to maintain a sterile environment. Osteoblasts derived from animal bone tissue, is the cell type that was selected and was under investigation in all the experiments. Specifically, the cell line of MC3T3 is extracted from mouse calvaria and when the cells are found in organized groups, they produce minerals and proteins to compose a bone tissue.^[263] For the cell culture of MC3T3s a specific mixture of cell culture medium, antibiotics and proteins has been prepared to optimize cell growth and proliferation. The medium was purchased by Merck, UK and it was the “Minimum Essential Medium Eagle Alpha Modification, with sodium bicarbonate, without L-glutamine, ribonucleosides and deoxyribonucleosides”. The medium was later supplemented with fetal bovine serum (FBS), L-glutamine and Penicillin-Streptomycin (all purchased from Merck, UK), at a final

concentration of 10%, 2.5% and 1% respectively. The cells are usually grown in T-75 and T-175 flasks in the presence of cell culture medium and incubation conditions. They are stored at a sterile environment of 37 °C and 5% CO₂ while a zinc chloride - EDTA solution is often used to kill bacteria or fungi that might contaminate the culture flasks.

Also, during the cell culture process, cells become confluent on a culture flask after a few days, meaning that their proliferation rate is significantly decreasing. For maintaining an expansion in cell population, it is advisable to subculture confluent cells into new culture flasks. For that reason, Trypsin is often used to dissociate adherent cells without damaging them. It is an enzyme which cleaves the peptide bonds in proteins.^[264] In this case, the hydrolyzed proteins are the ones found in the focal adhesions of the cells, forcing them detach from the flask surface in which they are cultured. This subculturing process is also known as “passaging” due to the term “passage number” that is expressed as the number of times a specific cell culture has been divided or transferred to another vessel. Cell lines with a high passage number often exhibit alterations in protein expression,^[265] differentiation,^[266] morphology and efficiency compared to the lower ones.^[267] Avoiding the use of (lower quality) cell lines that have been cultured for a long period of time, is of great importance when it comes to successful experimentation. Cell line quality is an important factor to the scientific community due to the passage number effects on cells.^[265-268] Though, the mechanisms behind these effects are not yet fully understood which limits the actions that the researchers can take to reduce them or avoid them in their experiments.^[269]

B. Cell counting and splitting

Nevertheless, cell growth is not always moving forward as expected and a variation from the anticipated cell population is a common fact. For example, MC3T3s are ideally doubling their population every 38 hours according to the datasheet provided by the manufacturer.^[270] However, this is just an estimation as there are multiple factors that determine cell proliferation, such as sterility levels, culture flask size, growth medium etc. Cells are often found more or less confluent than expected therefore a counting mechanism had to be implemented especially during the passaging process. The cell counting procedure was carried out using a counting chamber device known as hemocytometer.^[271] It consists of a thick glass microscope slide which has a grid of vertical lines formed by laser engraving. The area of the squares formed between the lines is known therefore it is possible to count the number of cells in those areas for a specific volume of the cell suspension and thereby calculate the concentration of cells in the overall mixture. Upon having the number of cells extracted from each flask during the cell splitting process, it is possible to divide them according to the desired number of cells. For example each T-175 flask yields approximately 4 million cells when 70-80 % confluent which could later be splitted into 4 parts and placed into new T-175 flasks for expanding the culture. The cell splitting procedure when cells are confluent at a T-175 flask goes as follows.

The old medium is removed from the cell culture flask and 10 mL of PBS (Merck, UK) are used to wash away any remaining content. Afterwards, a 6 mL solution of Trypsin-EDTA (Merck, UK) is pipetted into the flask, following a subsequent incubation for 5 minutes. After 5 minutes the cells are trypsinized therefore we add 6 mL of ess and extract the 12 mL mixture into a 15 mL conical centrifuge tube (Falcon™, Fisher Scientific, UK). The tube is then centrifugated for 5 minutes at 1000 rpm. Later, the liquid is removed, and 1 mL of fresh a-MEM is added and mixed (pipet the cell-medium solution up and down) with the cell pellet

that is formed at the bottom of the tube. Then, 10 μL of the cell suspension is transferred to a 1 mL conical tube and mixed with 90 μL of Trypan blue stain (Merck, UK). Trypan blue is an azo dye which is used to stain dead cells and distinguish them from live ones. It traverses through the dead cell membrane; hence live cells are excluded as they are selective in the compounds that go through their membrane. This method is also known as dye exclusion. A thin glass coverslip is placed on top of the hemocytometer, and 10 μL of the trypan-cell mixture are pipetted on each side of it. Capillary forces contain the suspension between the engraved part of the hemocytometer and the thin coverslip. The live cells marked white are then counted under a bright field microscope for each one of the four major sections of the hemocytometer. Same counting process is followed on the other engraved side and the total number of cells is divided by 8 (4 sections x 2 sides) to get an average number of cells. Finally, the concentration of the cells in the original mixture is calculated using the equation below:

$$\left(\frac{\text{cells}}{\text{mL}}\right) = \frac{(\text{avg number of live cells counted}) * (\text{dilution factor})}{(\text{volume of 1 large square in mL})} \quad (1)$$

The volume of 1 large square in the hemocytometer is known and equal to 10^{-4} mL as the marked area is 1x1 mm and the depth between the coverslip and the bottom is 0.1 mm. The dilution factor depends on the ratio of trypan blue and cell suspension. In our case 10 μL of the suspension were diluted at a total 100 μL of mixture yielding a dilution factor of 10.

Therefore (1) can be expressed as:

$$(1) \Leftrightarrow \left(\frac{\text{cells}}{\text{mL}}\right) = (\text{avg number of live cells counted}) * 10^5$$

As a result the total cell number is calculated as the cell density multiplied by the volume of the original cell suspension which in this example it is 1 mL. A portion of these cells is then transferred into the new cell culture flasks for expanding cell population. For a T-175 flask it is recommended to use an initial cell population between 5×10^5 and 10^6 cells. For example, if the

number of cells in the original 1 mL suspension is 4×10^6 , then the amount of volume transferred into the new T-175 flask should be between 125 and 250 μL . Finally, the flask is filled with fresh cell culture medium (a-MEM) up to 20 mL and is placed at the incubator. The same protocol is followed for T-75 flasks with half of all the quantities mentioned above.

C. Cell storage

Cell cultures are susceptible to microbial contamination and the effect of passage number as mentioned before. An established cell line is considered a valuable resource which requires both time and money to be invested. Therefore, it is crucial to freeze down batches of cells to preserve them for a long-term storage. Often during the subculturing process, a small surplus of cells is frozen to build a seed stock. This cellular bank can serve as a continuous feed of fresh early passage number cells that can be used for experimentation. Other (working) stocks of cells can be continuously replenished from the frozen ones preventing a depletion of the cell bank with only a minimum increase in the passage number from the initial stock. The cryopreservation of cultured cells is achieved by storing them in liquid nitrogen in the presence of cell culture medium and a cryoprotective agent like dimethylsulfoxide (DMSO). DMSO is required to reduce the freezing point of the medium and slow down the cooling rate for preventing crystal formation that might damage the cells. The preparation of a freezing medium is straightforward. It is a mixture of normal supplemented medium (a-MEM with FBS, L-glutamine and Penicilin-Streptomycin) with DMSO at a 9:1 ratio. The cell suspension is prepared as mentioned in the counting section and a part of it containing approximately 2 to 5 $\times 10^5$ cells is mixed with the freezing medium at a total volume of 1 mL. The vial should then swiftly be placed in $-80\text{ }^\circ\text{C}$ for 4 h at a special container which slowly cools down the cells and at the same time minimize the time they are in contact with the toxic DMSO at the liquid state.

Regarding the process of thawing cell line stocks, a different procedure is followed. The vial is removed from the liquid nitrogen and is thawed at a 37 °C water bath. When the cell suspension is almost at the liquid state, it is carefully transferred using a sterile pipette into a centrifuge tube containing 10 mL of a-MEM. The tube is then centrifuged, the supernatant is removed without disturbing the cell pellet at the bottom and cells are resuspended in 1 mL of fresh culture medium. The new suspension is transferred onto a T-75 flask and 9 more mL of fresh a-MEM are added before incubation.

D. Material Preparation and seeding

The hydrogel fibers were kept in the fridge at 8 °C to prevent or slow down bacterial and fungi growth. Though, as these materials are stored in a non-sterile environment, they are not suitable for cell culture. There are several common practices of sterilization, such as autoclave, UV exposure, or ethanol immersion, all of which are considered particularly effective. Yet, ethanol and autoclave will probably damage the material due to the ethanol interfacial tension and the high temperatures respectively. Also, UV light is reported in the literature to be damaging the surface characteristics of soft biocompatible materials and should be used with caution. To tackle this limitation, we constructed a custom-made UV chamber with a standard 254nm and 13 Watt UV lamp for sterilizing efficiently the GG hydrogel fibers.

Once the material is sterile, the fibers are transferred to sterile 6-well plates and the osteoblast (MC3T3) seeding takes place. A cell suspension is prepared to a desired concentration of cells and with the use of microliter pipettes the cells are deposited on top of the material. The materials are then left on the incubator for 2-3 hours before the subsequent filling of the well with fresh cell culture medium. The wells are refreshed every 3 days to supply

the cells with nutrients found in the medium and at the same time prevent the accumulation of toxic by-products that might inhibit cell growth and proliferation.

The protocol of cell seeding starts with the preparation of a 1 mL cell suspension containing the desired number of cells. That number depends on the cells we want to deposit over a certain area of the fiber. There are two crucial parameters though that need to be taken into consideration before preparing and seeding the cell suspension. First, the suspension droplet should be only deposited on top of the material and avoid dripping on the supportive glass slide to prevent the sedimentation and subsequent attachment of the cells away from the material. Cells tend to migrate and proliferate on a stiffer substrate so most of them might establish themselves on the stiffer glass slide rather than the soft hydrogel.^[9] Secondly, there should be enough culture medium for the cells to grow and attach over the 3h incubation time. We can therefore deduce that the suspension droplet which will be deposited on top of the fiber should: a) contain the right amount of cells, b) have a sufficient volume of medium for preventing cell death and c) at the same time not exceed the limits of the fiber and drip onto the supportive glass slide. For example, if the desired cell seeding density is 1,000 cells/mm² and it is known that the fiber can support up to 10 μ L of medium per 5 mm², then for covering a total area of 15 mm², a 5×10^5 cells/mL suspension is prepared and 3 drops of 10 μ L each are deposited on top of the fiber. Once the material is loaded with MC3T3s on its surface, it is incubated for 3 h to allow the cells to adhere to the substrate as much as possible. During that time if a part of the culture medium on the top is evaporated it should be carefully refreshed with new one. After 3 h the wells are filled with 4 mL of fresh cell culture medium (a-MEM) by pipetting it slowly through the walls to avoid washing away the cells deposited on the surface of the material.

2. Live dead assay

A live dead assay is a common practice applied in eukaryotic cells for distinguishing the live from the dead cells and determine the level of cytotoxicity of a substrate or a substance present. A staining solution is used which is a mixture of two fluorescent dyes that differentially label live and dead cells. The first one is Calcein AM (CalcAM), a green fluorescent dye used to detect and quantify live eukaryotic cells. The excitation and emission wavelengths of Calcein are 495 nm and 515 nm respectively. Its main component is acetoxymethyl ester which diffuses through cell membrane and is hydrolysed by intracellular esterases. The secondary stain used to identify dead cells is Propidium Iodide (PI). It is a red fluorescent nuclear stain with an excitation maximum at 535 nm and an emission peak at 617 nm, which binds to the DNA of the cells by intercalating between the bases with little or no sequence preference. It is often combined with CalcAM as it cannot permeate the cell membrane making it a useful tool to distinguish necrotic and apoptotic from healthy cells based on the integrity of their membrane. The stains were applied on top of the cell cultured materials at a volume of 2.5 μL CalcAM and 5 μL PI per mL of cell culture medium on the well. To facilitate confocal imaging later on the amount of a-MEM in the wells was 2 mL which was sufficient to cover the material's surface.

A. Osteogenic cell culture medium preparation

An osteogenic cell culture medium is a type of medium applied to bone cell types (such as osteoblasts, mesenchymal stem cells, bone marrow stem cells etc.) which promotes the formation of bone tissue and metabolic activity of the cells. To prepare osteogenic cell culture

medium, ascorbic acid (L-Ascorbic acid, Merck, UK) and beta-glycerol phosphate (β -Glycerophosphate disodium salt hydrate, Merck, UK) were added to the supplemented a-MEM. One thing that needs to be taken under consideration is that the aqueous solution of ascorbic acid may oxidize by air rapidly, reducing its half-life. Therefore, regular preparation of small batches of the osteogenic medium is recommended. To make a batch of 50 mL, a quantity of 5 mL of normal medium (a-MEM) is aliquoted at a 15 mL conical tube and 0.108 g of beta-glycerol phosphate (10 mM) as well as 2.5 mg of ascorbic acid are added and stirred to dissolve. The solution is then sterile filtered, to remove any aggregates or bacteria found in the powders, using a 0.22 μ m filter. The solution is then transferred to a 50 mL tube and it is supplemented with 45 mL of fresh medium to reach the target volume. Osteogenic medium should be kept in 8 °C for no longer than 2 weeks as the ascorbic acid action will be inhibited as previously mentioned.

3. X-ray Fluorescence (XRF)

In this study, XRF is used to detect calcium and phosphorus elements present at the surface of the biomaterials which resulted from the gradient of mechanical properties and its effect on bone cells. The preparation of samples for the XRF tests involves the samples that were incubated for 15 and 30 days under normal or osteogenic medium. After the incubation time the medium from the wells is removed and the fibers are washed with PBS and deionized water thoroughly to remove all the ions from the culture medium and the PBS. The fibers are then left to dry and collapse before placing them at the M4 TORNADO (Bruker, UK). Upon the loading of the sample to the XRF a vacuum is generated using a pump connected to the equipment. The X-ray tube is pre heated and operated at 50 kV and 400 mA. The samples are located, and the elements found in the surface of the substrate are analysed. Further,

quantification of elements is applied using the built in software, to provide us with useful information regarding the distribution of the elements of interest, which in this case are calcium (Ca^{+2}) and phosphorus (P, which is found at the ionic form of PO_4^{-3}).

RESULTS

Sodium Alginate experiments

1. Microfluidic setup

The preparation of NaAlg solutions involved deionized water, NaAlg powder, calcium carbonate nanoparticles and polystyrene particles. The initial concentration used was 1% w/v NaAlg, 22mM nano-CaCO₃ and 0.1% w/v PS particles 200 nm at a 10 mL aqueous solution. The 200 nm polystyrene beads were used for facilitating the tracking of the material and visualize it due to its transparency, especially in water. They make the NaAlg fibers translucent as they are only a few microns wide making it difficult to detect them during extraction or characterization.

The microfluidic device was inspired by previous research papers that employed thermophoresis as a tool to study particle mobility or amyloid fibril transitions in the presence of a temperature gradient.^[161, 175] The dimensions of the device for the main microchannel are 600 μm wide, 4 cm long and 140 μm deep (Figure 26). The side channels are 1 mm wide, 4 cm long and 140 μm deep with a PDMS wall separating them from the main microchannel. The wall is 100 or 200 μm thick depending on the design of the device. The inlet is a cylindrical vertical channel of 1 mm in diameter and the outlet is a water bath with its dimensions varying on each microfluidic device. Some variations on the design of the overall microfluidic setup were implemented for studying different materials with different cross-linking protocols.

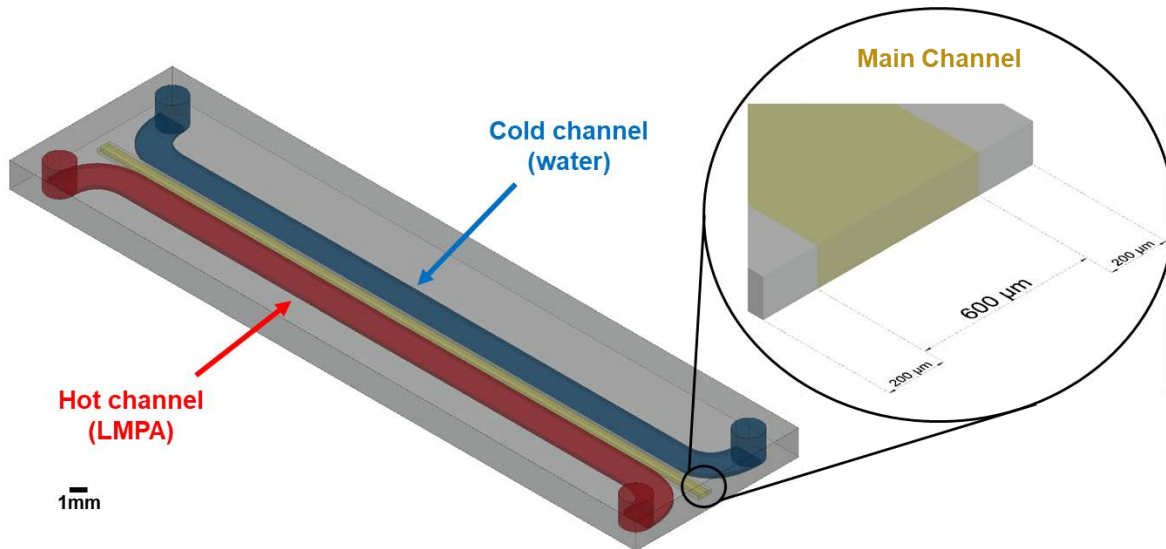


Figure 26: Microfluidic device design, with 200 μm thick PDMS walls between the channels and 600 μm wide main channel. Hot and cold side channels are highlighted in red and blue respectively

The first few sets of experiments were mainly focused to set an optimal operation procedure in terms of temperature and polymerization. The first and most important parameter for exploiting the phenomenon of thermophoresis is the temperature control. The temperature is monitored by thermocouples connected to a PC which converts voltage into Celsius degrees. However, as mentioned before PDMS is an excellent insulator which impedes our ability to measure temperature and it must be done from a short distance. For that reason, the device has two additional 1 mm diameter holes on the outer side of the side channels at a distance less than a millimetre (Figure 27). The distance is not known at first as they are opened at a random position as close as possible to the channel, but it is later calculated under the microscope. Images of the channels and the holes are captured and then by calibrating the pixel to micron ratio, the distance is accurately calculated to find the thickness of the PDMS wall between the thermocouple and the channel.

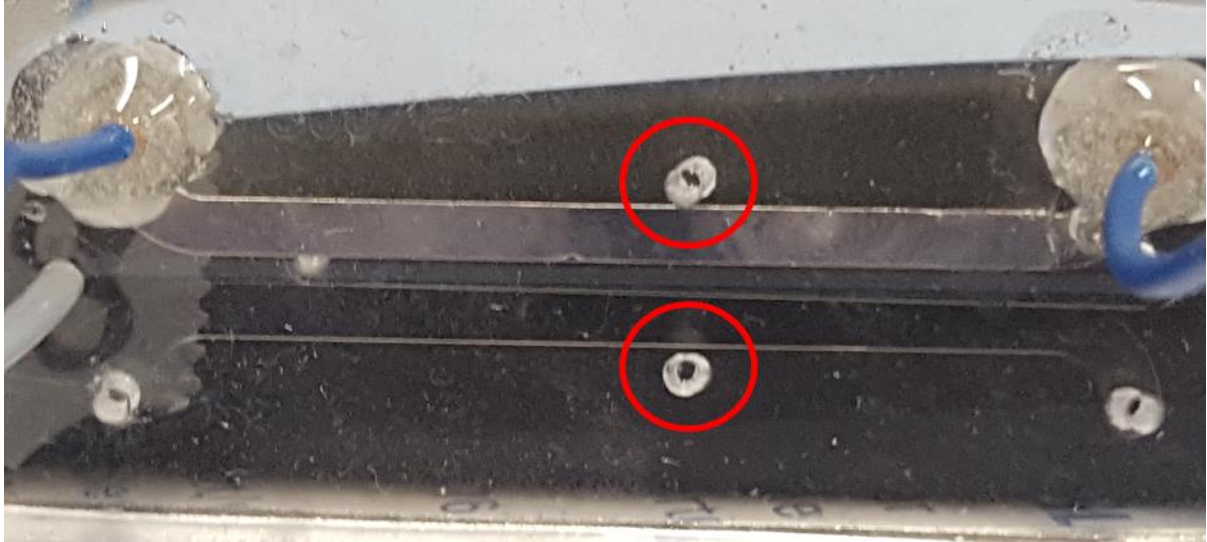


Figure 27: Picture of the microfluidic device from with the two thermocouple holes next to the side channels (marked with red). They serve as receptors for the thermocouples.

The temperature readings on the computer can then be converted to the actual temperature of the hot and cold side channel. The whole system is converted into an “electrical model” as shown in Figure 28, where the resistance of each material equals its thermal resistivity.

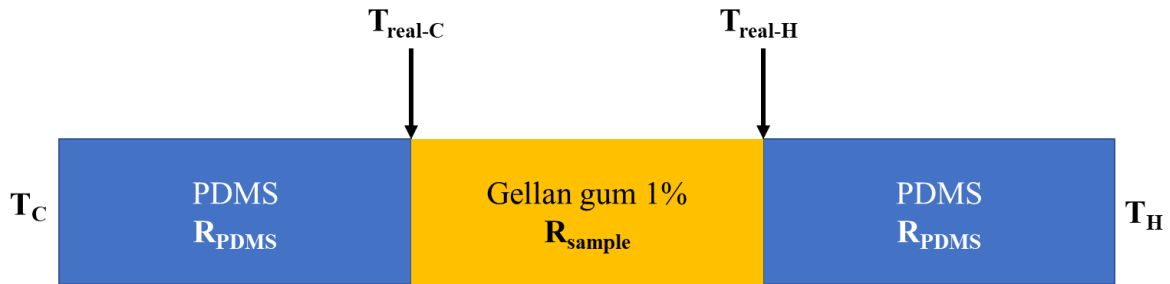


Figure 28: Schematic of the temperature distribution across the device and its electrical analogy in terms of thermal resistances.

$$\text{Defining : } \Delta T_{tot} = T_H - T_C, \Delta T_{PDMS-C} = T_{real C} - T_C, \Delta T_{PDMS-H} = T_H - T_{real H}, \Delta T_{sample} = T_{real H} - T_{real C} \quad (1)$$

$$\text{and } \Delta T_{sample} = \Delta T_{tot} \times \frac{R_{sample}}{R_{tot}} \quad (2), \text{ where } R_{sample} = \frac{d_{sample}}{k_{sample}} \quad (3)$$

$$\text{Considering that } k_{\text{sample}} = k_{\text{water}} \text{ and } R_{\text{tot}} = R_{\text{PDMS-C}} + R_{\text{sample}} + R_{\text{PDMS-H}} = 2g \frac{d_{\text{PDMS}}}{k_{\text{PDMS}}} + \frac{d_{\text{sample}}}{k_{\text{water}}} \quad (4)$$

Where T: temperature (°C), k: thermal conductivity (w m⁻¹ K⁻¹),

R: thermal resistivity (m² K w⁻¹) and d: distance (m)

By replacing equations 1, 3 and 4 in 2 we conclude that:

$$\Delta T_{\text{sample}} = \frac{(T_H - T_C)gd_{\text{sample}}}{2g \left(\frac{d_{\text{PDMS}}}{k_{\text{PDMS}}} + \frac{d_{\text{sample}}}{k_{\text{water}}} \right) gk_{\text{sample}}} \quad (5)$$

Given the fact that the thermal conductivity of water and PDMS are known as well as the dimensions of the device and the temperatures on the sides, the actual temperatures can be easily calculated. For example, the device with $d_{\text{PDMS}} = 100 \mu\text{m}$, $\Delta T_{\text{sample}} = \Delta T_{\text{tot}} \times 0.43$, and for the device with $d_{\text{PDMS}} = 200 \mu\text{m}$, $\Delta T_{\text{sample}} = \Delta T_{\text{tot}} \times 0.27$. These values represent the conversion factors of the measured to the actual temperature gradient across the 600 μm channel, which are mainly dependent upon the PDMS wall that mediates between the thermocouple and the sample. Though, when referring to temperature gradient we refer to a unit of temperature per unit of length which is the reason why the two previous conversion factors should be adjusted to match a length of 1 mm instead of the width of the device (600 μm). This is achieved by simply dividing the two numbers by 0.6, resulting in a final conversion factor of 0.72 and 0.45 for the 100 and 200 μm wall thickness, respectively. For example, if the reading for the hot channel is at 72°C and for the cold one at 60°C, giving us a measured (experimental) temperature gradient of 12 °C, the actual temperature gradient across the main microchannel for the 200 μm wall thickness is $12 \times 0.45 = 5.4 \text{ °C/mm}$.

To further optimise this system and get more accurate readings for the two side channels, another device preparation method has been developed. Instead of the old design which

included 2 side holes on the outer section of the device, the thermocouples were now directly in contact with the cooling/heating medium.



Figure 29: Picture of the microfluidic device with an incorporated thermocouple hole to the Joule heater (in red). The hole is directly above the joule heater and the thermocouple is inserted and is in direct contact with the low melting point alloy.

Regarding the hot channel, a hole of 1 mm diameter is opened in the middle of the channel before the sealing of the device. This hole however remains closed during the LMPA injection for preventing the diversion of the liquid metal. Once the LMPA is solid the hole can be unsealed giving us direct access to the hot channel. The thermocouple is then inserted with the addition of a thermal component for improving conduction and minimize any heat loss. In this way, the measurement of the thermocouple is closer to the actual temperature of the Joule heater and no other calculations are needed, as it comes in direct contact with the hot metal whereas on the previous case a thick PDMS wall was between the thermocouple and the LMPA. On the other side, the thermocouple is inserted to the outlet tube reaching all the way down to the cold channel. By that method, the thermocouple is in contact with the “cold” water of the outlet giving us a more accurate temperature profile for the water flow over time. Implementing these changes to the system greatly improved the manipulation of the gradient as a faster response rate was now observed during step changes to the input values. Once the

value of the flowrate of the cold water or the value of the voltage on the power supply were altered, a change in the temperature of water and LMPA respectively was noticed at the data logger with just a short response time. This time was previously much higher as the thick PDMS walls were limiting the heat flow from the heater/cooler to the thermocouples thus more time was required until the system reached a steady state.

2. Preliminary results

The first set of experiments was conducted using the sandwich-like device with NaAlg. The temperature gradient of 2.3 °C/mm was applied for 10-15 minutes through the 600 µm wide and 200 µm wall thickness channel, for the 1% w/v NaAlg aqueous solution. After the temperature gradient was applied the acidic oil was injected slowly through the bottom channel to not deform the membrane and disrupt the concentration gradient of the alginate solution. To ensure a high degree of cross-linking, the material was left for over 15 minutes in the device upon the injection of the acidic solution. However, the materials yielded from this process were of uniform stiffness, as the time that the temperature gradient was applied was not sufficient to allow the alginate molecules migrate towards one of the sides.

Another factor that was taken into consideration was the effect of convection to the main channel. Convection is a transport phenomenon which occurs due to the bulk motion of a fluid due to the difference in density across its area.^[272] For example, when a fluid is heated from the bottom, the layer closer to the heating source exhibits lower density thus moving upwards and likewise colder and less denser fluid layers move downwards.^[272] In this case, the presence of a temperature gradient will induce a difference in densities on the main channel and especially near the hot channel. The phenomenon of convection will then disrupt the movement

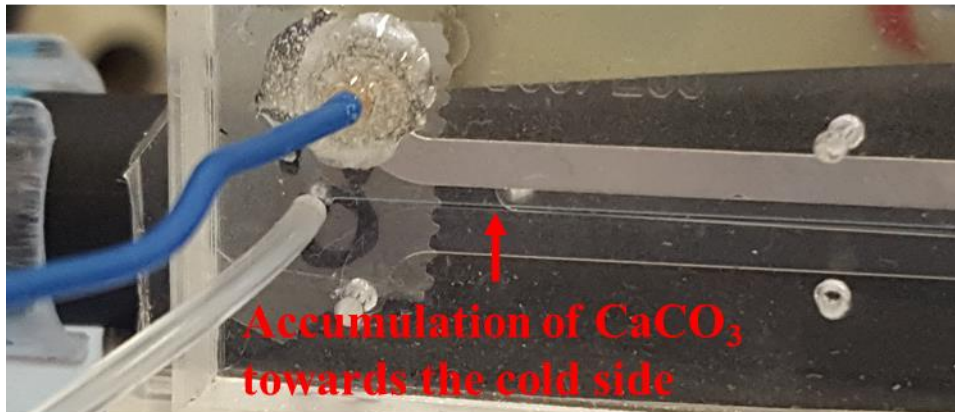
of the alginate molecules due to the bulk motion of water. In addition, the temperature gradient will also be disrupted as convection will mix the different temperature layers of water, thus making thermophoresis having a weak effect on the NaAlg molecules. To tackle this issue the device was placed on a vertical position with the hot side channel to be on top of the setup. In this way, the hotter and denser layers of the solution will remain at the top part of the channel and will not disrupt thermophoresis or alginate movement. However, the fibers were once more exhibiting a uniform stiffness as the residence time of the material was too short.

In the next few experiments, the residence time in the microfluidic device was increased to 40 minutes. Though, the fibers extracted were approximately 30-50 μm wide which differs greatly from the expected 600 μm . A thorough investigation of the situation showed that CaCO_3 nanoparticles were sedimenting or migrating towards the cold side at the bottom. After 15 to 20 minutes the bottom part of the vertical device is highly concentrated in calcium carbonate aggregates whereas towards the top part a more transparent solution has been observed, indicating the mobility of CaCO_3 nanoparticles. It is well known that calcium carbonate does not disperse in water, thus forming large aggregates which can be affected both by gravitational and thermophoretic forces in the case of the temperature gradient. The heavier an object is, the more is “pulled” by gravity and in our case it is also seen from the literature that calcium particles are affected by thermophoresis with particle size to be the main factor of the movement.^[161, 273] To tackle this limitation, a method had to be developed to break the aggregates of the nano- CaCO_3 in the alginate solution and maintain an evenly dispersed solution of nanoparticles. To approach this issue at first, an ultrasonic probe-sonicator (UP400St, Hielscher Ultrasonics, Germany) was used to sonicate the mixture in different intensities and times. As the sonicator was operating at 96% of its total power, heat was generated on the vessel which prevented the use of it for a long period of time without a water bath to cool it down at the same time. A nano- CaCO_3 aqueous solution was prepared and then

sonicated for 120 seconds in total (3x40 seconds each time). The solution was left overnight showing an excellent stability after 16 hours. Though when mixed with NaAlg and polystyrene particles and injected in the device, the calcium carbonate nanoparticles started to sediment and form aggregates after 10 minutes in the device.

Another method was the addition of an organic solvent in the mixture, to create more stable suspensions and disperse evenly the CaCO₃ nanoparticles.^[274] The solvent used was 2-Propanol (also known as isopropanol, or isopropyl alcohol, IPA) which replaced a part of the deionized water to the mixture. A 10 mL solution of IPA was prepared by adding 0.4 g of nano-CaCO₃ (0.4 M), followed by gentle vortex mixing. The result was a white opaque liquid indicating a homogenous dispersion of CaCO₃ nanoparticles which lasted for more than 24 hours. Yet, large aggregates of the CaCO₃ nanoparticles could be observed in the solution. For that reason, a combination of both the use of organic solvent and sonication was employed to obtain the best result. The isopropanol solution was prepared as previously described, but this time a sonication of 80 seconds (2x40 secs) was carried out afterwards. This resulted to the breakup of the CaCO₃ aggregates and at the same time the dispersion of the particles evenly throughout the 10 mL solution. The final 4 mL solution was prepared by mixing 2 mL of a 2% NaAlg solution, 80 µL PS particles 10%, 220 µL of the 0.4 M nano-CaCO₃-IPA solution and 1.7 ml of deionized water. A low percentage of 4.88% of IPA was assumed not to influence the biocompatibility of the material and required further investigation. During the application of the temperature gradient in the microfluidic device the CaCO₃ nanoparticles remained stable throughout the whole process.

Before



After



Figure 30: Dispersion of nano-CaCO₃ particles at the NaAlg solution inside the microfluidic device. Pictures before and after the application of sonication and organic solvent. A fully transparent channel with a thin white line underneath is noticed before whereas a white transparent line across the whole channel is observed after.

As a result, 1% sodium alginate hydrogel fibers were successfully extracted from the device after the application of thermophoresis. The temperature gradient was applied for 40 minutes with the measured temperatures on both sides of the device to be 23.5°C and 33°C. These two temperature readings correspond to an actual temperature gradient of 4.3°C/mm. The fibers were placed onto supportive glass slides and stored in deionized water at 8 °C.

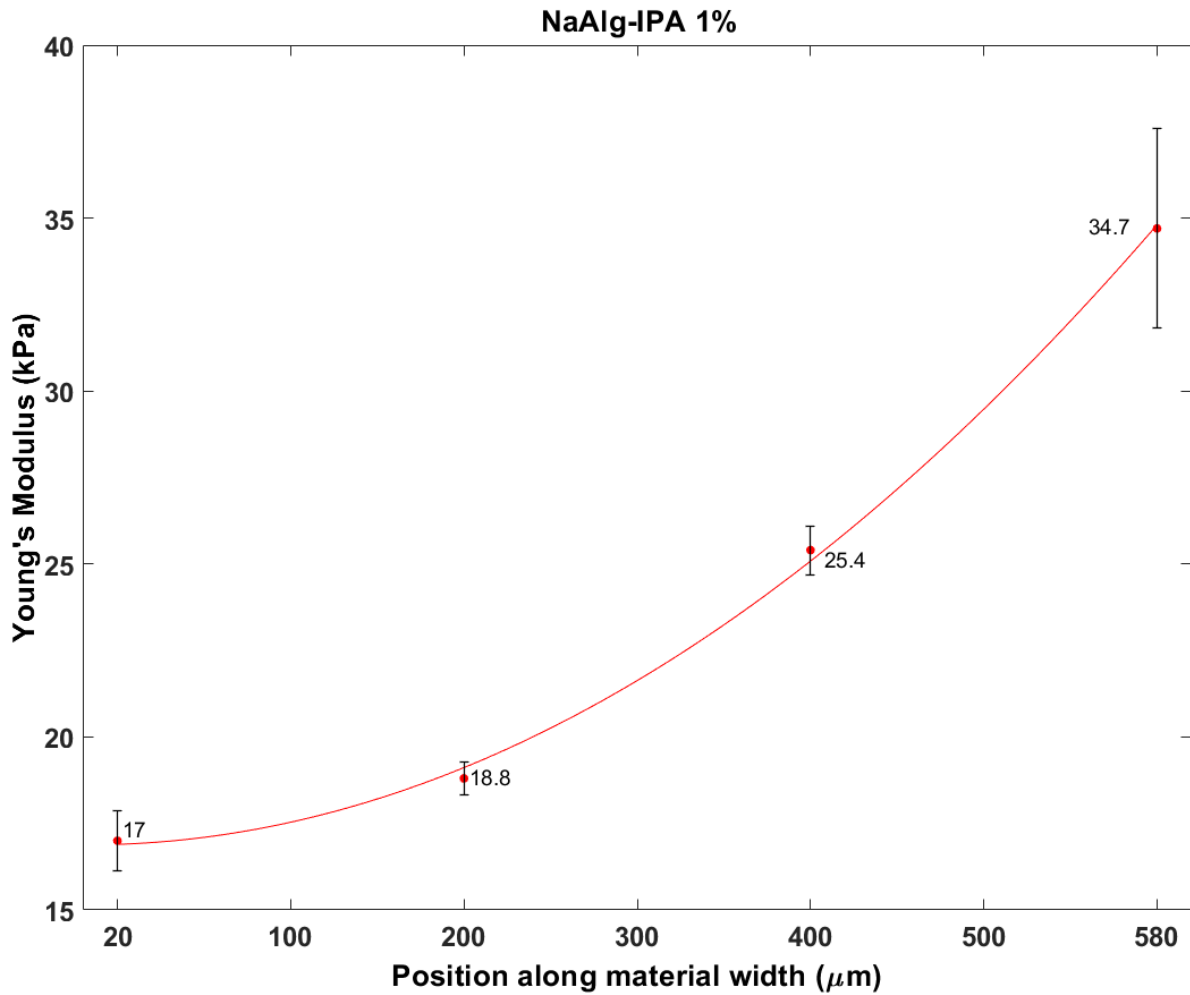


Figure 31: NaALG 1% stiffness gradient profile across the width of the material. Error bars represent standard error. Exponential fit was used for creating the trendline. Each point is the average of 3 areas on the same width position across the length of the same fiber.

These preliminary results have revealed us the capabilities of this new method for manipulating the mechanical properties of biomaterials. The material extracted exhibited a gradient of stiffness which is attributed to the effect of thermophoresis and can consist the foundation for standardizing a method to fabricate stiffness gradient biomaterials. The errorbars represent the standard error that was calculated from the measurement spots conducted at each local area. As seen on Figure 31 we can observe that the stiffness gradient ranges from 17 kPa up to 35 kPa which suggests an increase of 100% in Young's Modulus at

an exponential rate. That increase was achieved through an actual temperature difference of only 2.5°C across the 600 μm wide channel applied for 40 minutes. The higher stiffness area of the material was observed towards the “colder” side of the channel suggesting that the direction of the thermophoretic force applied to the NaAlg chains was pointing towards that side and the Soret coefficient was positive. We can therefore conclude that those preliminary results reveal and confirm the effect of thermophoresis on the stiffness of the substrate.

Moreover, an exponential trend is observed on the stiffness gradient of the material which should theoretically follow the same trend as the concentration gradient induced by thermophoresis in the liquid phase of the NaAlg mixture. The steady state concentration gradient just before the polymerization step for a two-dimensional thermophoresis could be approximated by the exponential depletion law, given that the temperature gradient is linear and assuming that both diffusion and thermodiffusion coefficients are constant.^[275]

$$\frac{c}{c_0} = \exp [-S_T(T - T_0)]$$

Where we observe that the normalized concentration c/c_0 depends on the temperature difference across the channel $T-T_0$.^[275] For that reason, an exponential trendline is fitted to all the plots as they exhibit an exponential stiffness gradient which is resulting from the concentration gradient that previously occurred while thermophoresis was applied.

However, the solution of sodium alginate is a complex multi-component system which makes it difficult to achieve a high reproducibility degree. It is a hydrogel that yields soft, fragile 3-D fibers that are hard to manipulate, especially at the extraction stage. In addition, the materials may form crackings depending on the batch and they tend to degrade over a short period of time. Also, the presence of acetic acid and 2-propanol might possibly affect biocompatibility and decrease cell viability. Hence, a simpler, single component system that

forms strong 3-D gels should be investigated and added in the process to tackle the above limitations.

Gellan gum experiments

1. Microfluidic setup

Several materials were taken under consideration in order to choose the optimal one that will fit in the process. Collagen, pectin and gelatin methacrylate were a few materials that were under investigation. However, most of these materials required a complex cross-linking mechanism with multiple components which increases the amount of parameters that needed to be considered (e.g. in the case of NaAlg the breakup of CaCO_3 particles) and reduce the reproducibility degree of the system. Therefore, the material that was selected due to its ease of cross-linking and the fact that no additives were needed in the solution, was gellan gum. The aqueous solution contained deionized water, GG powder, calcium ions to act as a cross-linker and PS particles for the visualization of the fibers. Also, a new device had to be designed to meet the cross-linking criteria of the material which is mainly dictated by temperature.

The GG device is similar to the NaAlg one, but it differs only to the polymerization part as shown in the experimental protocols chapter. The top part remains the same for both devices, briefly a 600 μm channel with two side channels for the LMPA and the cold water flow to act as hot and cold thermal sources respectively. There is also a water bath outlet to facilitate the fiber extraction and prevent any potential cracking or folding of the material. This top PDMS part is sealed using a typical 1 mm thickness microscope glass slide which is a much better heat conductor than the previously used PDMS membrane. Under the glass part of the microfluidic device a Peltier module was placed to increase the overall temperature of the

device for keeping GG in a liquid state and prevent an early cross linking in the device. Also, a solid iron block was attached to the other side of the Peltier module to dissipate heat . Three thermocouples are placed around the different areas of the microfluidic device, one in contact with the metal alloy, one in the outlet of the water channel and another one between the module and the glass (bottom) part of the device (Figure 32). A conductive thermal component was used in both the LMPA-thermocouple and the Peltier-thermocouple interfaces to improve heat transfer and acquire more precise temperature readings.

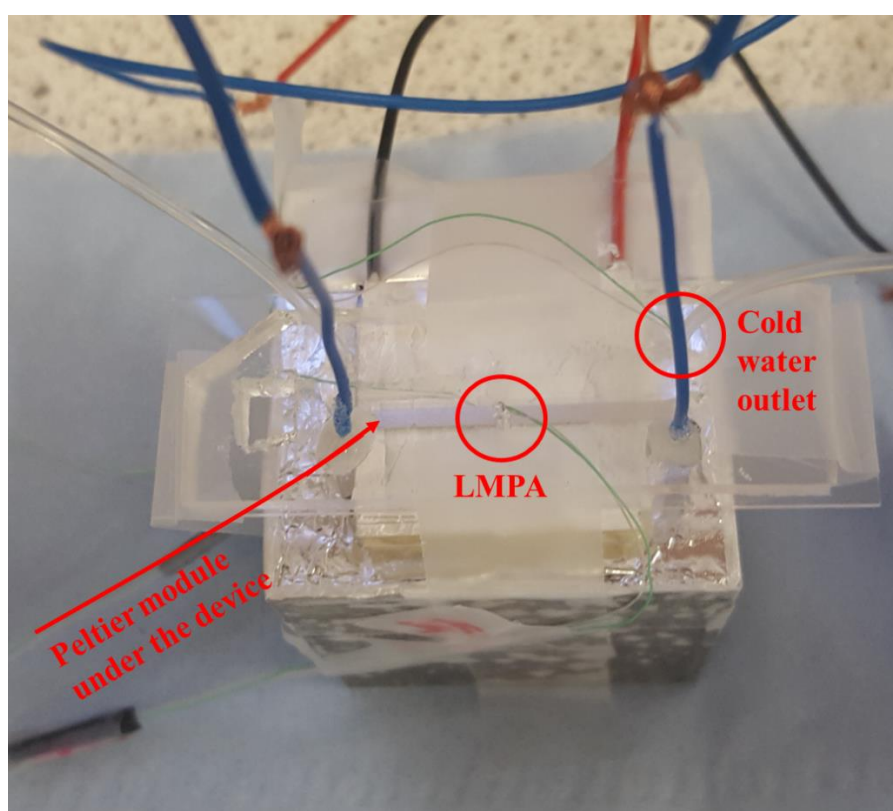


Figure 32: Picture of the microfluidic setup consisting of the device the pelier module and the 3 thermocouples mounted at the a) LMPA, b) cold water outlet and c) between the device and the peltier module.

This device was specifically designed to match the polymerization process of GG. Once GG powder is mixed with water it forms a viscous liquid at room temperature and in the presence of ions it forms a strong cross-linked 3D gel. These ions can be either monovalent

(such as Na^+ or K^+) or divalent (such as Ca^{+2} Mg^{+2}). Divalent cations have a much stronger effect on gel strength than monovalent ones do.^[247, 276] Especially calcium forms the strongest ionic bonds between the GG chains and the material will not re-melt under autoclave conditions.^[247] Another factor that influences gel strength and the overall substrate stiffness is the concentration of GG in the mixture. It is expected that an increase in the GG concentration will cause an increase in substrate stiffness, contrary to the increase of cross-linker concentration which follows a different trend (as seen from the product SDS).^[247] A further investigation on both factors was carried out to determine the optimal concentration of GG and ions that will yield strong 3-D gels suitable for cell culture . On Figure 33 a solution of 1% GG was prepared as previously reported and was supplemented by a different cross-linker concentration at a time, to observe the effect of the Ca^{+2} ions on the average stiffness of the material. In Figure 34 though the CaCl_2 cross-linker solution was kept constant at 5 mM, with the GG concentration being the variable this time.

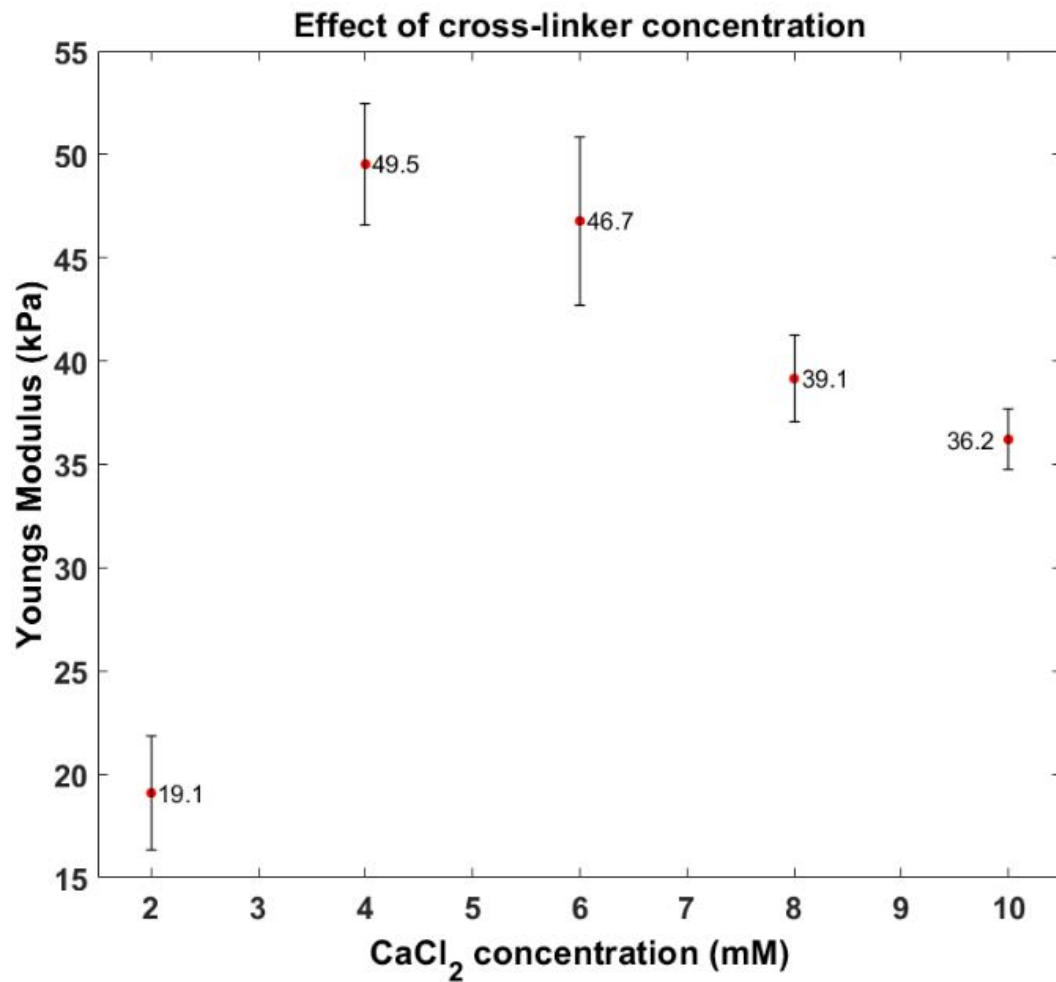


Figure 33: Effect of the CaCl₁ cross-linker concentration to the stiffness of uniform 1% GG materials. Error bars represent standard error. Each point is the average of 3 areas randomly selected on the same uniform stiffness fiber.

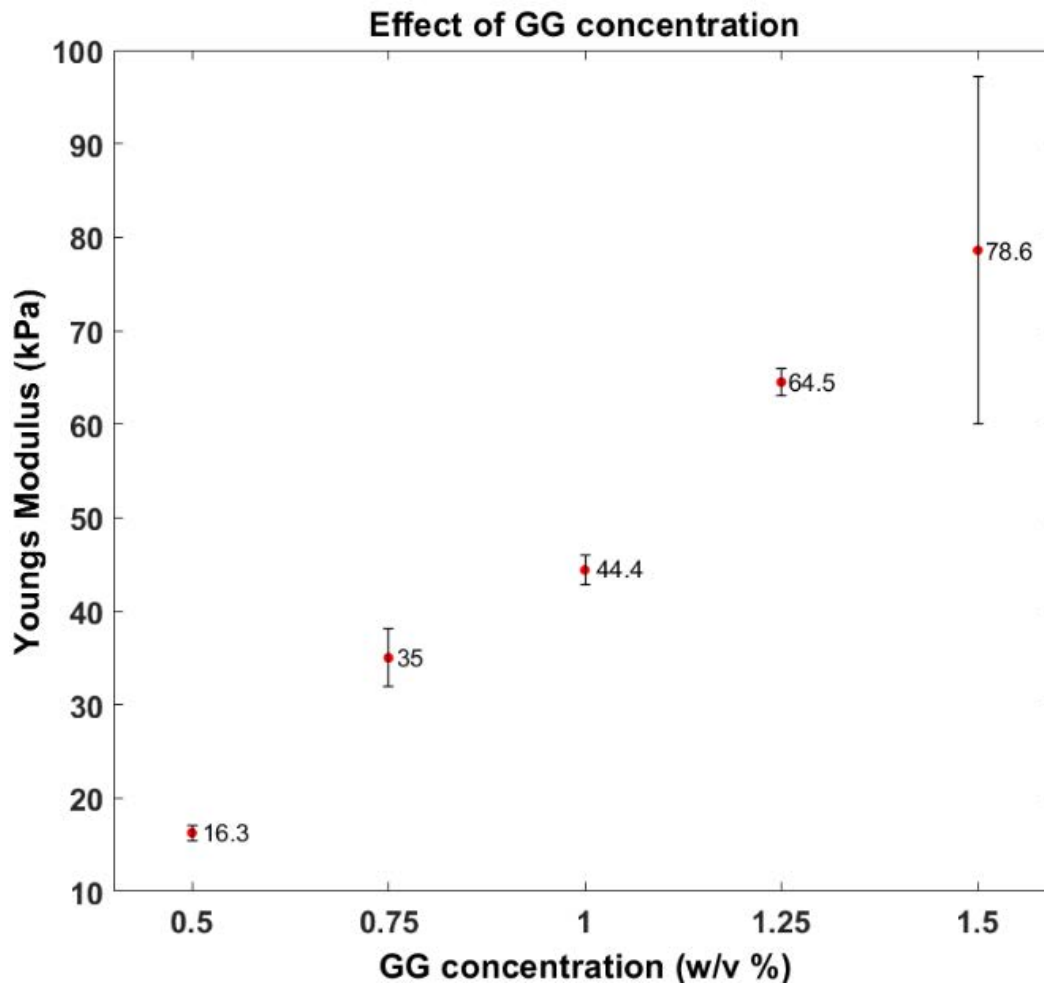


Figure 34: Effect of the GG concentration to the stiffness of uniform surfaces with 5 mM of cross-linker added. Error bars represent standard error. Each point is the average of 3 areas randomly selected on the same uniform stiffness fiber.

As the overall goal at a later stage is to culture cells on the biomaterials and given the fact that tissue cells do sense the stiffness of their substrate,^[9] the optimal concentration of GG and CaCl₂ that was selected was 1% and 5 mM respectively. The average stiffness at these conditions is around 45 kPa which upon the application of thermophoresis will vary due to the concentration gradient that will form in the microfluidic channel.

In the current microfluidic device, the GG solution is pre-mixed on a beaker at a high temperature (70 °C) to maintain a liquid state and then injected at the main micro-channel.

Afterwards, the application of thermophoresis was initiated for 15 minutes. The temperature values were 74 °C for the hot channel and 60 °C for the cold one, resulting at a temperature gradient of 6.3 °C/mm. Upon reaching the desired concentration gradient state the device was cooled down rapidly to initiate the polymerization process and “translate” the concentration gradient into a stiffness gradient. To achieve a rapid freezing of the material the polarity of the Peltier module underneath is reversed so as to convert the heating surface into a cooling one. Initially 6 V and 0.6 A were applied to the module which acted as a heat pump, however when the process was reverted to the cooling function of the module the voltage was increased to 8 V. At the same time the temperature of the thermoelectric module dropped from 63 °C down to 0.5 °C within 1-2 minutes. After at least 15 mins of cooling (to ensure complete polymerization) the material is extracted by forcing it out of the channel using deionized water. The material is extracted in the water bath that is placed at the outlet of the device and is then collected using tweezers onto PLL coated or surface treated glass slides (mentioned in the experimental section).

The data presented on Figure 33 and Figure 34 were generated by MSc student Hanzhen Xu who conducted all the experiments under my supervision.

2. Preliminary results

The initial results reveal no gradient therefore the residence time of the material on the device had to be increased to 20 minutes. After that increase, the following results were much more promising displaying a slight stiffness gradient. However, there were several inconsistencies on the force mapping across the material’s surface and often the standard error bars were overlapping each other between the different spots. Once the residence time was

increased to about 30 minutes for a temperature gradient of 6.3 °C/mm, we obtained some valuable results which clearly confirm the existence of a stiffness gradient on the biomaterial.

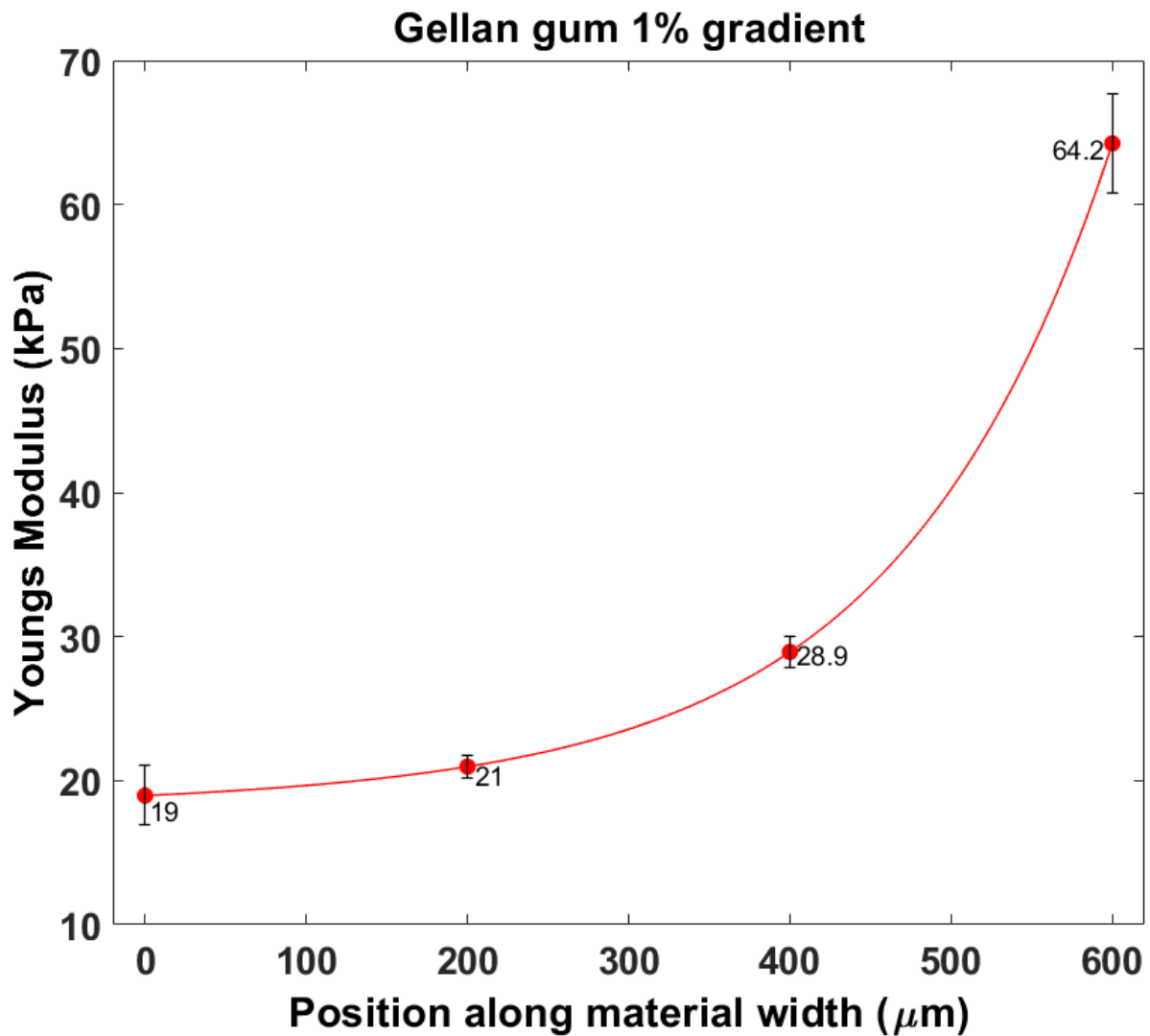


Figure 35: Gellan gum 1% stiffness gradient profile across the width of the fiber. Error bars represent standard error. Exponential fit was used for creating the trendline. Each point is the average of 3 areas on the same width position across the length of the same fiber.

The material was extracted from the water bath situated at the outlet of the device using a pair of tweezers. The fiber was retrieved from the water bath with ease as the GG solution contained a minimum amount of (200 nm diameter) polystyrene particles in order to make the material visible in water and facilitate its extraction. However, the influence of those polystyrene particles that were dispersed in the original solution needed to be further

investigated. For that reason, uniform substrates with various PS particle concentrations were prepared and further indented to determine if the particles have any effect on the young's modulus of the substrate. The results (Figure 36) show that there is no difference in the stiffness of the substrate up to a PS particle concentration of 0.1%. Above that percentage there is clear evidence that they influence the Young's modulus values and mixtures with more than 0.1% of particles should not be used.

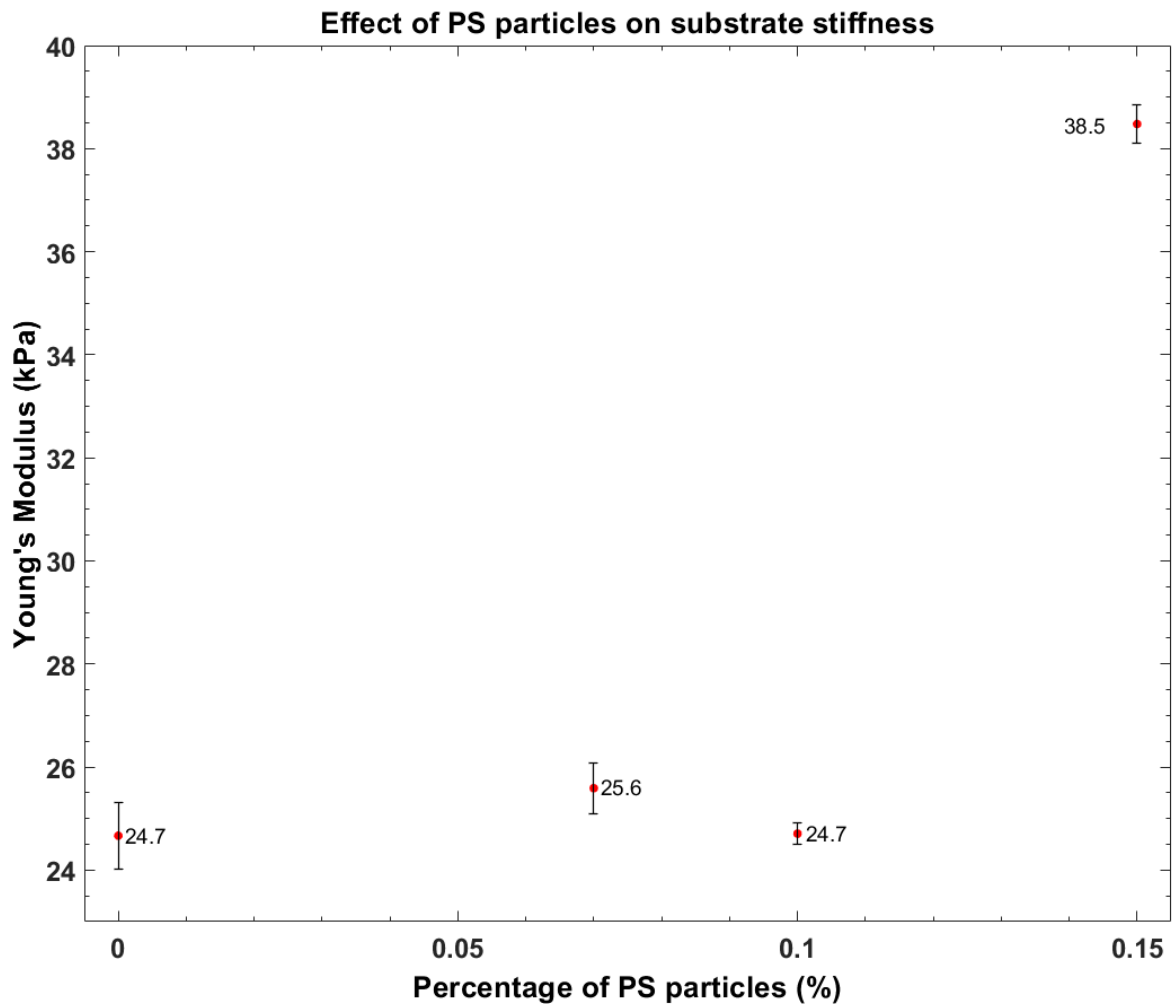


Figure 36: Effect of 200nm polystyrene particles on the stiffness of uniform 1% GG substrates. Error bars represent standard error. Each point is the average of 3 areas randomly selected on the same uniform stiffness fiber.

Later though, a further optimization of the extraction process made it possible to obtain transparent GG fibres without the addition of PS particles. The presence of polystyrene particles was adding another level of complexity to the system which could potentially influence the stiffness gradient and for that reason their deletion from the mixture was of great importance. The water bath technique was also abandoned as the gel strength of the GG fibers was allowing the extraction of the material using air to “push” it towards the outlet without folding or disrupting the gradient. The stiffness gradient results of the 1% GG fibers without the PS particles exhibit a similar trend to the previous ones (Figure 37).

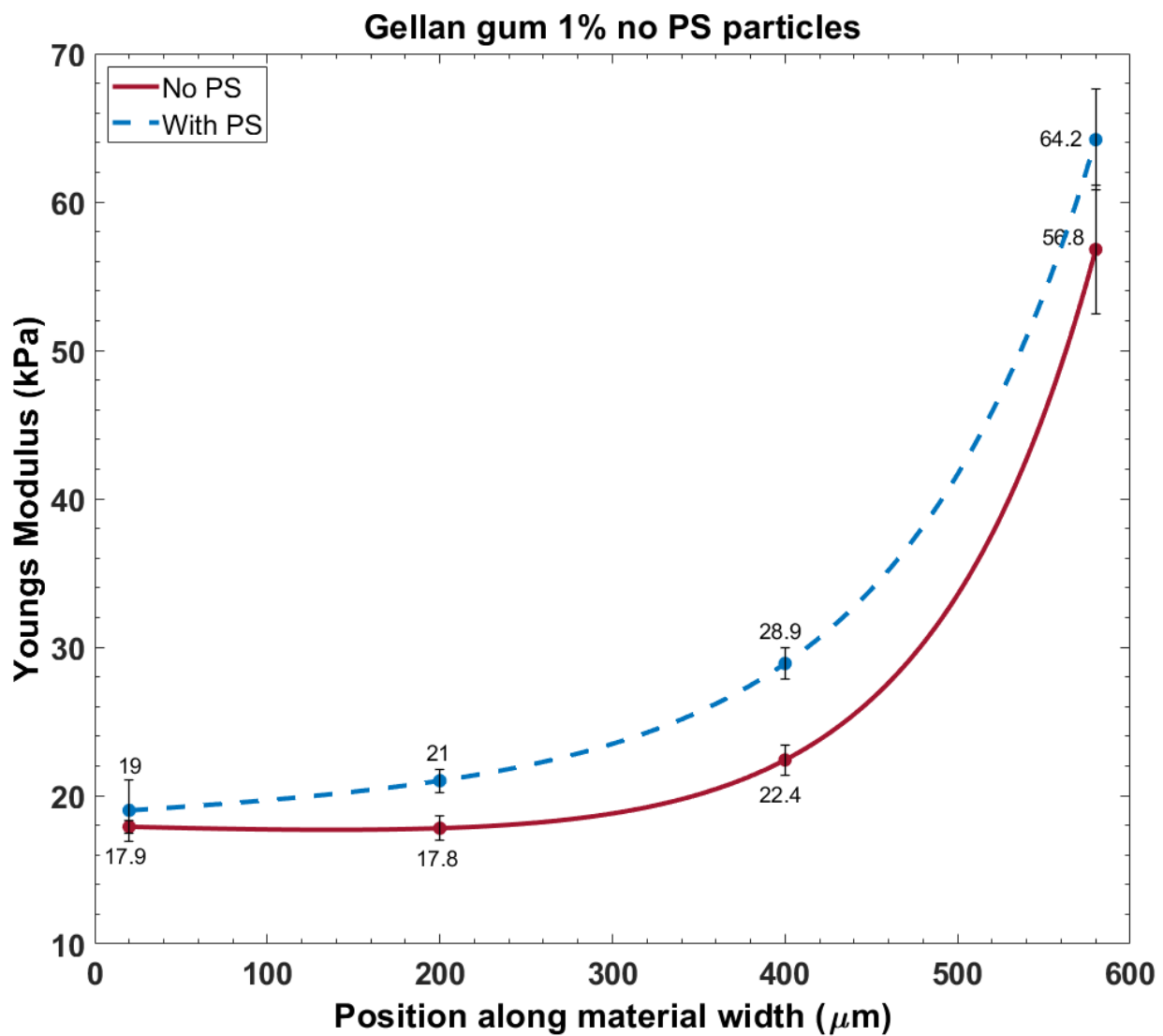


Figure 37: Stiffness gradient profile across the width of two Gellan gum 1% fibers, with the blue line representing the sample prepared with PS particles and the red line representing the sample prepared without the

addition of PS particles. Error bars represent standard error. Exponential fit was used for creating the trendline. Each point is the average of 3 areas on the same width position across the length of the same fiber and each trendline represents a single sample.

3. Main results

The optimal conditions in the device were later established at a gradient of 7.6°C/mm with an average device temperature around 74°C and a residence time of 30 minutes. The polymerization time remained at 15 minutes and the extracted materials were placed on top of PLL coated or plasma treated glass slides. They were later stored in petri dishes filled with deionized water to keep the materials hydrated. As we can see from Figure 35 and Figure 37 the presence of PS particles does not influence the gradient or raise the overall Young's Modulus values. This could be attributed to the fact that PS particle concentration is particularly low. It could also be credited to the fact that PS particles are larger (200 nm) than the GG coils (2.5 Å for a single coil),^[277] thus having a smaller diffusion coefficient and consequently in the time that thermophoresis is applied, the PS particles don't drift as much. We can therefore conclude that the PS particles did not affect the gradient or the stiffness of the material as the YM values across its surface are similar between the two materials.

Moreover, in all the GG experiments the direction of thermodiffusion was the same as the NaAlg experiments previously conducted. The higher stiffness area of the hydrogels, which theoretically stems from the highest GG concentration area in the micro-channel, was found to be the "colder" side, indicating a positive Soret coefficient.

Additionally, the local stiffness of each point along the gradient GG fiber was correlated with the concentration data obtained from Figure 34. That shows a clear link between the effect

of thermophoresis, responsible for the creation of a concentration gradient, and the observed stiffness gradient (Figure 38). To establish the correlation between stiffness and GG concentration we used the set of materials with different initial GG concentration presenting no stiffness gradient that was previously prepared and measured. To be consistent, each sample was injected in the same microfluidic device that was previously used to fabricate the concentration gradient material and was kept at uniform (room) temperature until the gelation process was completed. We were then able to obtain a Young's modulus versus GG concentration master curve (see inset in Figure 38). This permitted us to extrapolate the local concentration of GG along the material exhibiting a stiffness gradient as shown in the main plot in Figure 34.

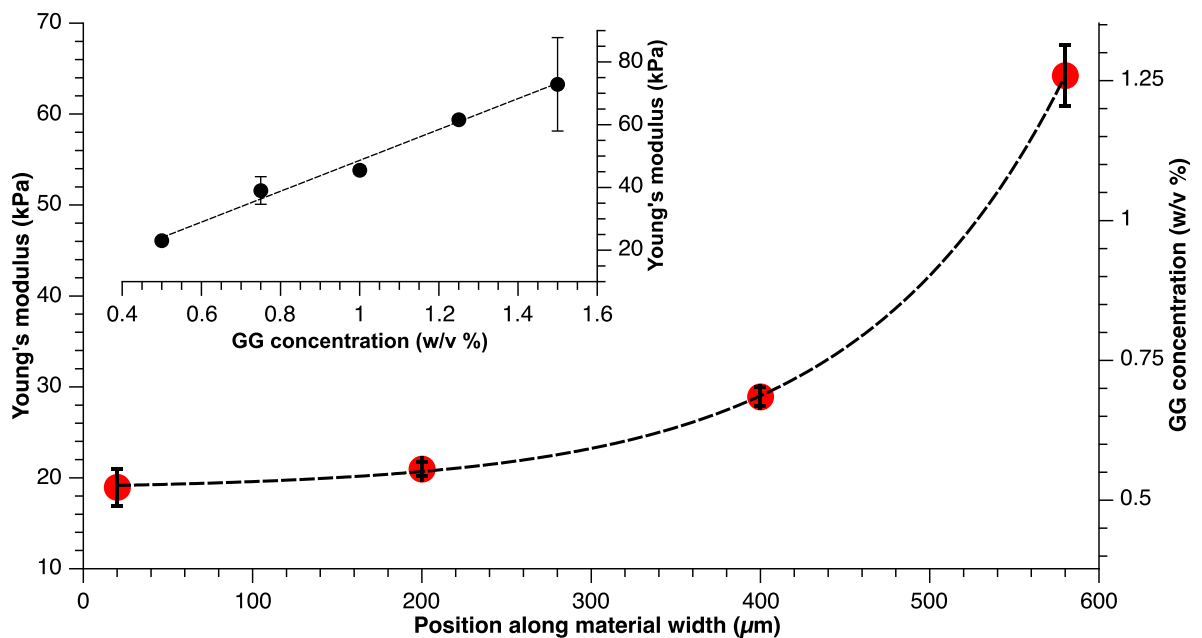


Figure 38: Young's modulus values for the stiffness gradient GG fiber (left axis) and the corresponding local concentration (right axis). The dashed line is an exponential fit. In the inset the Young's modulus for different GG concentrations obtained from uniform substrates used to calibrate the main curve. Error bars represent standard error. Each point is the average of 3 areas on the same width position across the length of the same fiber.

However, it is yet unclear the true mechanism that is responsible for the formation of the gradient. The initial theory related to the stiffness gradient on the hydrogel is based on the hypothesis that thermophoresis induces GG coils to migrate towards one of the sides of the temperature gradient over time thus creating a concentration gradient in liquid state. Once the liquid solution is cross-linked into a hydrogel then the concentration gradient is converted into a stiffness gradient. Although, this might be the case it was yet unknown whether other mechanisms take place. Though, this initial assumption was later validated as we imaged the morphology of the substrate using SEM to demonstrate the porosity and concentration gradient across the material surface. More details follow on the SEM section.

SEM imaging

The force mapping of the material's surface using AFM, gave us valuable information on the existence and the magnitude of the stiffness gradient of the biomaterials. However, the nature of the existence of the gradient remained unclear. The mechanism behind the formation of the stiffness gradient could be attributed to a variety of factors such as crosslinking gradient,^[278] migration of calcium particles etc.^[279] For example, thermophoresis might force calcium ions in the solution to migrate towards one of the sides resulting in a cross-linking gradient with one side having a higher number of binding spots between the GG coils than the other. One of the main key findings of this research project is that thermophoresis induces a concentration gradient which upon the polymerization of the hydrogel “translates” into a stiffness gradient. To be able to confirm that hypothesis we employed an additional method which could provide us with both qualitative and quantitative information on the morphology of the substrate at the nanoscale. For that reason, SEM was employed as the imaging method,

which could give us valuable information on the gradient of gellan fibers and the porosity of the substrate across the material surface.

1. Material preparation

The GG fiber is found in an aqueous environment and consequently the imaging of the surface is impossible as SEM equipment's operate under vacuum. Though, the hydrogel cannot simply be dehydrated as once the water content is removed, polymeric structure might collapse or damage its surface characteristics.^[280] For addressing these issues, we needed to convert the hydrogel into an aerogel before an SEM scanning could be performed under vacuum. There are several different ways to achieve that conversion, including ambient,^[281] supercritical and freeze drying.^[282, 283] Freeze drying (also known as lyophilization) is a quite popular method in industry which relies in the thawing of the water, although in this case a freezing step of the material would harm its structure as water crystals will expand and damage the GG fiber cross-linked network.^[284] The most popular, gentle with the hydrogel structure, but expensive method due to the equipment cost, is supercritical drying using CO₂.^[285] An additional step of solvent exchange though was required before a CO₂ drying could be performed. This added a new complexity to the system as the exchange of solvents would significantly change the material volume due to the osmotic de-swelling kinetics once the solvent diffuses through the hydrogel pores.^[286] For that reason, several solvent exchange experiments with water and ethanol and various exchange times were performed. The first few experiments included a transition from 0 to 100% (with a 10% step) ethanol solution by simply transferring the material to a higher EtOH concentration solution over 24-48 hours. The optimal exchange from water to ethanol

though was achieved with the addition of EtOH slowly over 24h via a syringe pump at a rate of microliters per minute to ensure a smooth transition from aqueous to organic solvent. The material was initially placed at a 20 mL petri dish, with only 200 μL of water deposited on its surface. The container was later filled with ethanol over 24 h by pumping 99.8% ethanol at a rate of 825 $\mu\text{L}/\text{h}$. In this way, the shrinkage effect of the material was negligible and the mechanical properties of the hydrogel were not damaged from the difference in pressure between the organic solvent and the water^[287] The material was later checked under the AFM to verify the integrity of the gradient which was maintained throughout its surface.

Following the exchange of solvents, the material was then transferred to our external collaborators at the department of chemistry at Cambridge University, where supercritical CO_2 drying took place. The fibers were transferred in specimen capsules (78 μm pore size, Agar Scientific) and dried by supercritical CO_2 (Quorum E3100 critical point dryer).^[288] They were flushed 4 to 5 times with liquid CO_2 followed by 15 min incubation in between.

2. SEM measurements

The hydrogel was converted to an aerogel maintaining its structural integrity and consequently the stiffness gradient exhibited along its width. Later, the fibers were sputter-coated with 15 nm iridium (Quorum K575X) to facilitate the reflection of electrons and obtain higher resolution images under the SEM as the GG fibers are a non-conductive material. We obtained the SEM images across the surface of the material, using a FEI Verios 460 scanning electron microscope at 2 KeV and 25-50 pA probe current. These pictures unveil the mechanism responsible for the creation of the stiffness gradient which confirms our assumption that is formed due to the gradient of concentration of GG coils across the material width. As

seen on Figure 39 the density of the overlapping GG fibers increases as we move from the one side to the other. To quantify the data obtained from these pictures, pore size was selected as the key property to investigate. The gradient of porosity is confirming that we can effectively manipulate a range of different mechanical properties of biomaterials in microfluidics using thermophoresis.

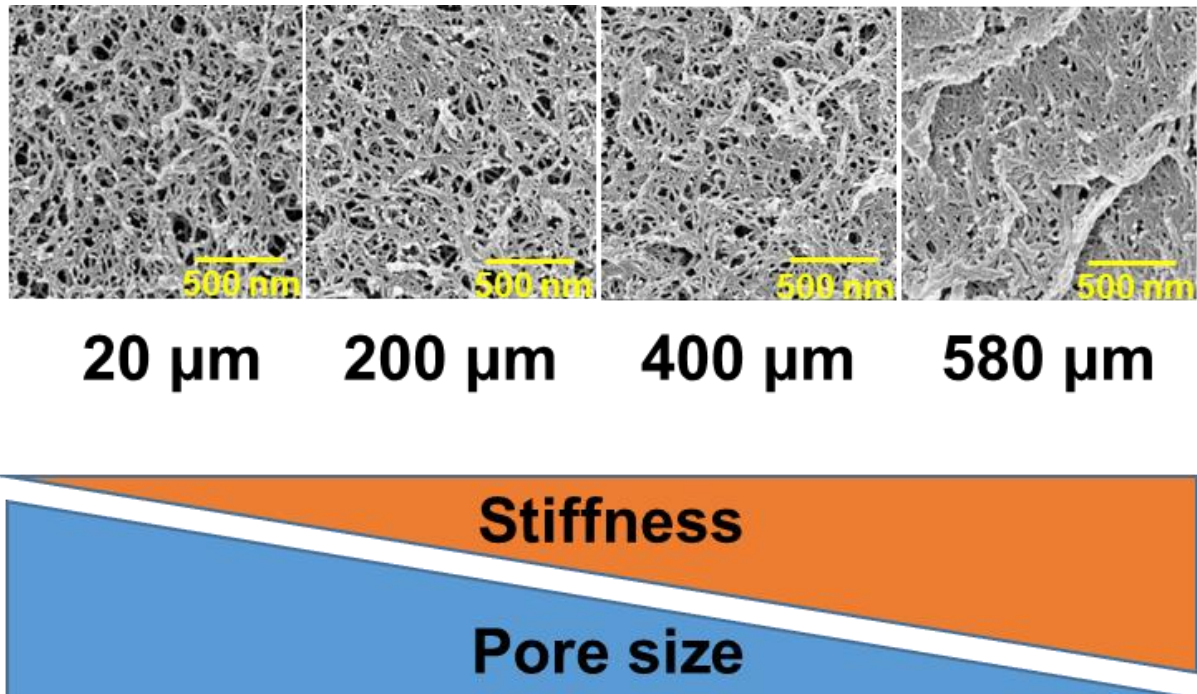


Figure 39: SEM images on 4 different areas to demonstrate porosity change across the width of the fiber.

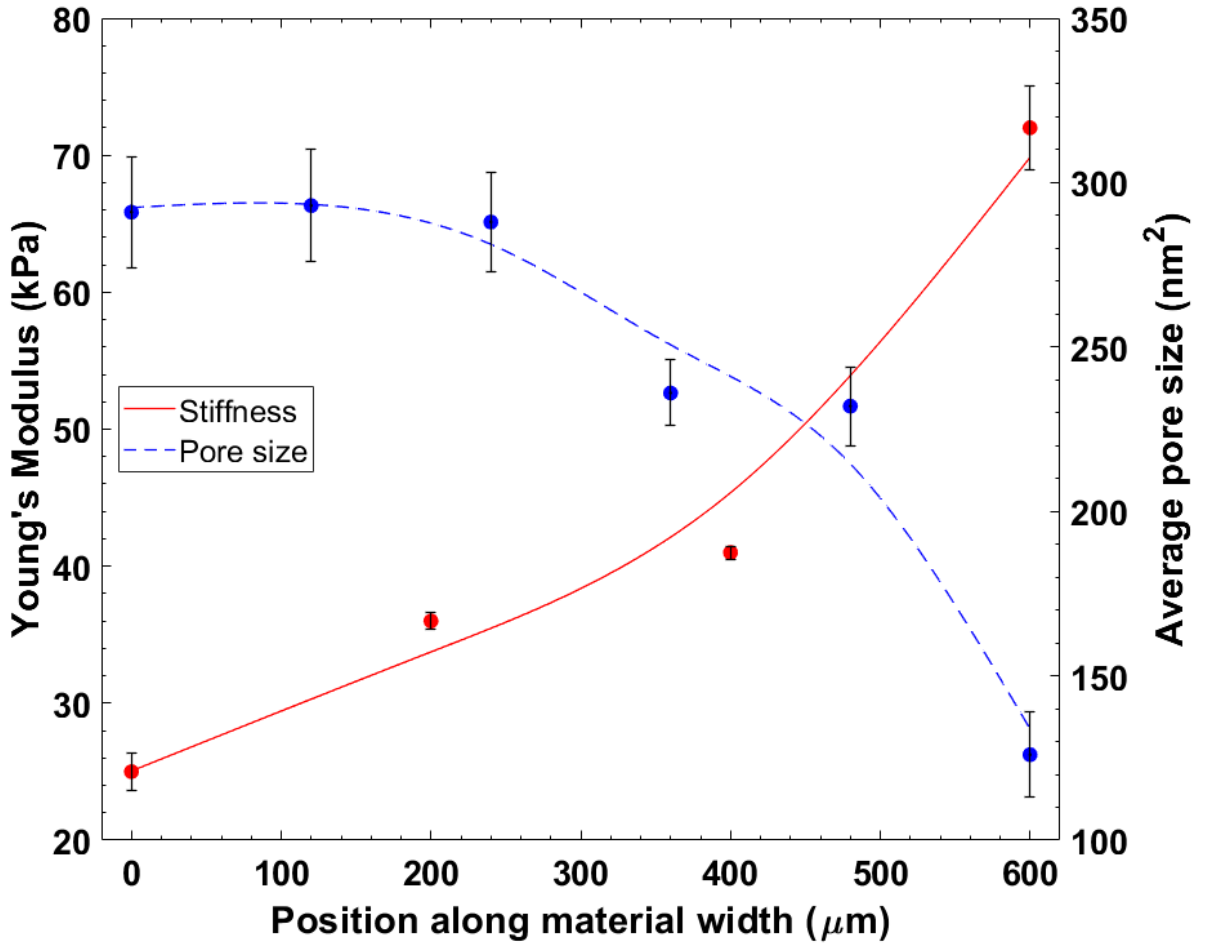


Figure 40: Pore size distribution versus Young's modulus data across the width of the material. Blue line represents the pore size and red line represents the stiffness of a single gradient GG fiber. Polynomial fit was used for creating both trendlines. Each stiffness point is the average of 3 areas on the same width position across the length of the same fiber. Each pore size point is the average pore size of a 2x2 µm area across the width of the same fiber. Error bars represent standard error.

As seen on Figure 40 the pore size distribution across the material width follows a similar but reverse trend to its stiffness. The material was characterised under the AFM, exhibits a stiffness gradient that ranges from 25 to 72 kPa and at the same time the SEM images reveal a porosity gradient scaling down from 290 to 130 nm². It is sensible to have a much smaller average pore size, around 130 nm² at the 72 kPa stiffness area as the concentration of GG coils is significantly higher, allowing less space between them. In addition, we can observe from the stiffness / pore size plot an exponential trend in both variables which can be noticed on the

SEM pictures where the GG coils are packed, often overlapping each other, at the higher stiffness areas.

Manipulation of the mechanical properties

Since the mechanism behind the creation of the stiffness gradient was investigated and revealed, we wanted to demonstrate the effective control over the gradient of mechanical properties and particularly the ability to fine-tune the stiffness range of the fibers. The fabricated hydrogels so far were only limited to a certain range of stiffness gradient along their width which consecutively leads to a limitation in terms of cell types that could be seeded at a later stage on the surface of the biomaterial. Considering that the ultimate goal of the project is to grow cells on top of the substrate and observe their activity over time, we further investigated several ways to improve the manipulation of the stiffness gradient of the biomaterials.

1. Effect of GG concentration

The first step towards this direction was the alteration of the GG concentration in the solution which was expected to have a major impact on the overall stiffness of the fibers. Theoretically, as the gellan gum concentration increases, an augmented amount of GG coils in the mixture will result at a stiffer material displaying higher Young's modulus values in both the softer and the stiffer side of the gradient. By keeping at a constant value the variables of a) temperature gradient, b) residence time in the device and c) cross-linker concentration but also by using the same device for all data sets, we altered the GG concentration from 0.8 to 1 and 1.5 % w/v. The microfluidic device used was the standard 200 μm wall thickness one, the

temperature gradient was kept constant at 4.5 °C/mm with a residence time of 27.5 minutes and a cross-linker concentration of 5 mM.

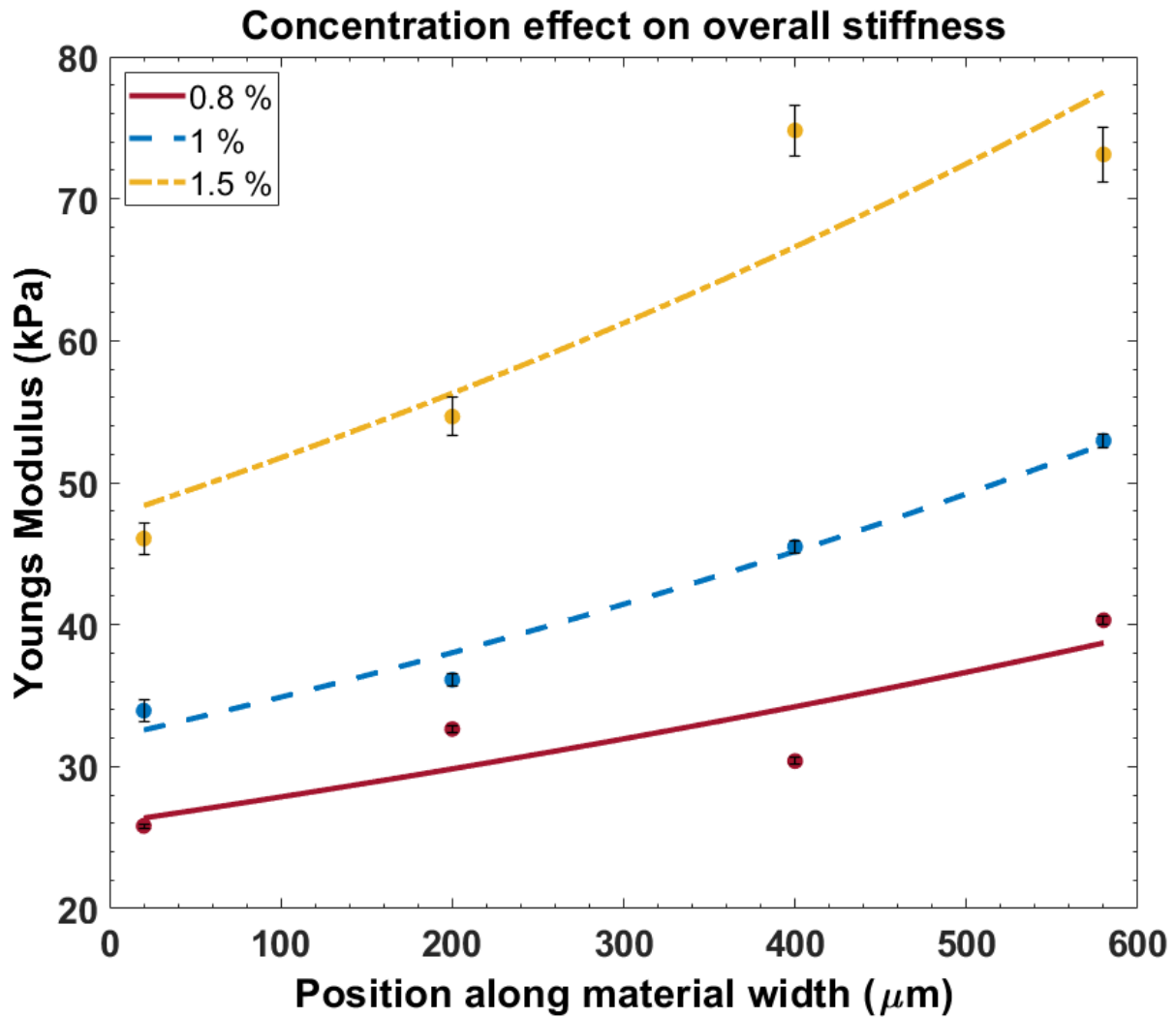


Figure 41: Effect of GG concentration on the stiffness gradient profile across the width of each material. Three different concentration GG fibers are represented each with a colored line (red 0,8%, blue 1% and yellow 1.5%).

Each point is the average of 3 areas on the same width position across the length of the same fiber and each trendline represents the stiffness profile across the width of a single sample. Error bars represent standard error.

Exponential fit was used for creating each trendline.

As observed on Figure 41 there is an overall increase of YM values across the stiffness gradient as the GG concentration increases which confirms the initial theory mentioned above.

The softer sides range from 26 to 46 kPa whereas the stiffer ones start from 38 kPa and reach

the 76 kPa mark for the 0.8 and 1.5 % w/v GG concentration, respectively. We can therefore conclude that it is feasible to shift the overall stiffness of the material by simply altering the initial concentration of the GG solution and that the increase of the YM values are proportional to the increase of the GG concentration (as seen on Figure 41). Also, the exponential gradient is similar for all 3 materials which justifies the fact that is independent from the concentration of the material but only depends on the temperature gradient and the residence time in the device. These results demonstrate the capability of shifting the stiffness gradient range towards higher or lower Young's modulus values which enables the potential of culturing a wider variety of cell types on the material.

The data presented on Figure 41 were generated by MEng student Rowan Liddle who conducted all the experiments under my supervision.

2. Effect of temperature gradient

In the same context, a way to tune and manipulate the stiffness gradient of the fibers was explored by altering the temperature gradient applied in the device. The GG concentration was kept constant at 1% w/v with the addition of 5 mM of CaCl₂, as well as the residence time (23 min) for the 200 μm wall thickness device. Furthermore, three different values were selected for the temperature gradient variable, namely 3.6, 4.5 and 5.4 °C/mm. The results are displayed at Figure 42 below.

The data presented on Figure 42 were generated by MSc student Wenbin shi who conducted all the experiments under my supervision.

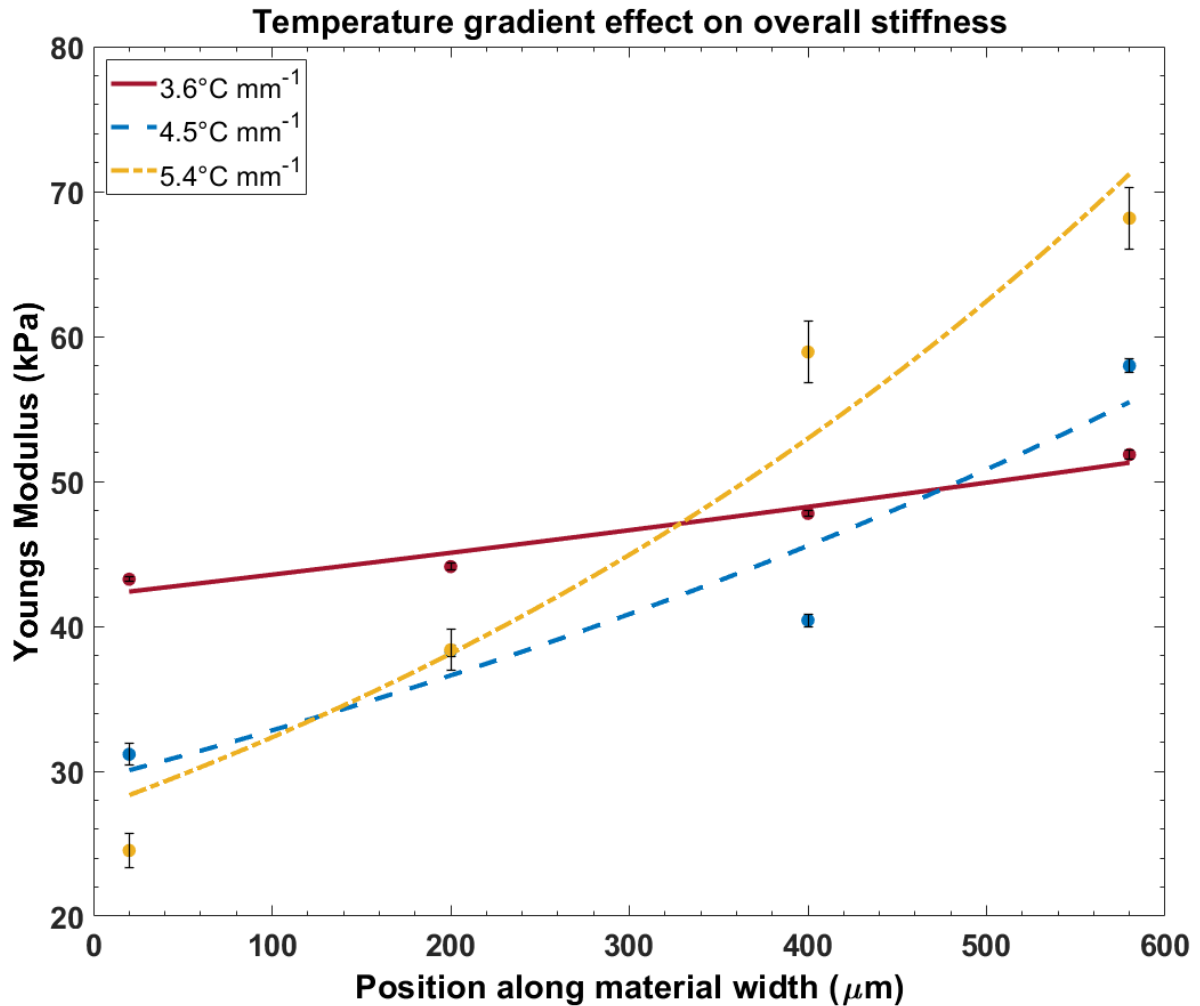


Figure 42: Effect of temperature gradient (applied at the microfluidic device) on the stiffness gradient profile across the width of the 1% GG fibers. Three different GG fibers were fabricated at various temperature gradients represented each with a colored line (red $3.6^\circ\text{C mm}^{-1}$, blue $4.5^\circ\text{C mm}^{-1}$ and yellow $5.4^\circ\text{C mm}^{-1}$). Each point is the average of 3 areas on the same width position across the length of the same fiber and each trendline represents the stiffness profile across the width of a single sample. Error bars represent standard error. Exponential fit was used for creating each trendline.

We can observe that the gradient of each data set becomes steeper for higher ∇T values. By increasing the temperature difference across the device, we generated a more pronounced exponential stiffness profile confirming the thermophoretic nature of the effect. The thermophoretic force has a stronger effect on the GG coils the more we increase the temperature gradient.^[169, 289] As a result, at a higher ∇T both ends were stretched to achieve a higher

maximum and a lower minimum Young's modulus value. This clearly depicts on Figure 42, where the lower ∇T value exhibits a linear trend whereas the higher temperature gradient data set displays an exponential trend.

3. Effect of residence time

Another factor that was expected to influence the stiffness gradient, is the residence time in the device. We conducted experiments with a constant GG concentration (1% w/v), cross-linker concentration (5mM) and temperature gradient (4.5 °C/mm) while the residence times varied. In principal, a higher residence time in the device will allow more GG coils to migrate towards the colder side of the material, leading to a steeper stiffness gradient. A trend similar to the previous ∇T results was expected, however as seen on Figure 43 the experimental data partially confirm that theory.

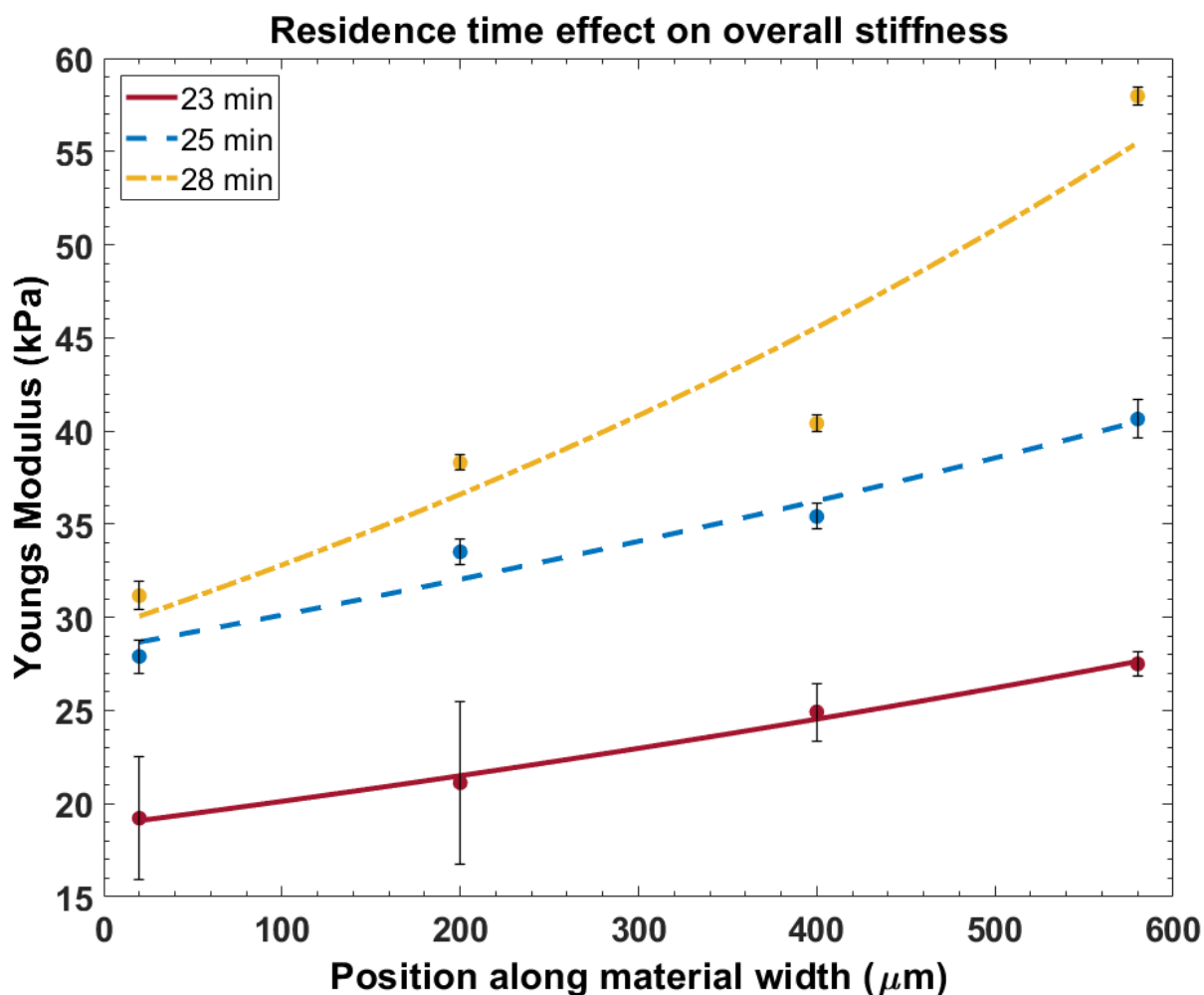


Figure 43: Effect of residence time (in the microfluidic device) on the stiffness gradient profile across the width of 1% GG fibers. Error bars represent standard error. Three different GG fibers were fabricated each with a different residence time in the device are represented 3 colored lines (red 23 min, blue 25 min and yellow 28 min). Each point is the average of 3 areas on the same width position across the length of the same fiber and each trendline represents the stiffness profile across the width of a single sample. Exponential fit was used for creating each trendline.

As we can observe, the gradient becomes steeper as we move to higher residence time values, similar to the Figure 42 results. Though as residence time increases the overall YM values are increased, similar to the trend of Figure 41 where GG concentration was the variable factor. The explanation to this unexpected trend is quite simple though. As residence time increases, water evaporates from the GG solution situated in the main micro-channel at high temperatures (ranging from 70 to 85°C). PDMS is well known to be a porous gas permeable

medium which cannot contain the evaporated water within the device, resulting to the decrease of the solvent (water) and the simultaneous increase of GG concentration throughout the material. As a result, a higher residence time leads to a higher dehydration rate of the material, creating a more concentrated, thus stiffer hydrogel overall. As seen on Figure 43 an average stiffness of 23 kPa is associated with the ~23 minutes of residence time in the device which as we move towards higher time values it increases to ~34 and ~45 kPa for the 25 and 28 minutes respectively.

In conclusion, the capabilities of the microfluidic device were explored thoroughly in order to demonstrate the effective manipulation of the mechanical properties of biomaterials. By altering parameters such as the magnitude of the temperature gradient, the residence time in the device or even the concentration of the material we were able to fine tune the mechanical properties of GG fibers. A novel, simple and efficient method which was introduced to address the problems of mimicking the tissue microenvironment accurately through the fabrication of 3-D scaffolds.

The data presented on Figure 43 were generated by MEng student Rowan Liddle who conducted all the experiments under my supervision.

4. Reproducibility of the method

The microfluidic platform developed, is a simple and straightforward technique which can be operated by monitoring the temperature gradient and the residence time of the hydrogel on the device. By keeping a certain standard on those 2 major parameters as well as the concentration of the initial solution, it is possible to generate fibers that exhibit similar mechanical properties. The gradient itself remains the same over the 600 μm width of the fiber with fluctuations of the stiffness across its surface. To further support that statement, we

fabricated a series of materials that were realized under the same conditions of temperature gradient, concentration, and residence time in the microfluidic device. The 1% GG solution was kept for 27 minutes in the microfluidic device, imposing a temperature gradient of 4.5 °C/mm. The results of the elasticity across their width are shown on **Error! Reference source not found.** below:

Table 1: Elasticity across the width of 4 independent samples that were prepared under the same conditions to test the reproducibility of the method. Four samples were prepared in total at the same microfluidic device, out of a 1% GG solution, at 27 minutes and 4.5 °C/mm temperature gradient. The YM values are the average of three measurements per sample, prepared in quadruplicate for the areas located on the same width position, followed by the standard error. The stiffness gradient is also averaged from the 4 independent samples and is expressed at Pa per μm across the width of the fiber.

Position across the width (μm)	Average Young's modulus (kPa)	Standard error
20	22.0	± 1.5
200	29.2	± 6.1
400	43.9	± 8.2
580	64.3	± 1.4
Gradient (Pa/μm)	75.5 ± 2.8	

We can observe that the average Young's modulus for all the samples comes a low error factor ($< 10\%$) which indicates that the stiffness increase over the 600 μm width of the fiber is similar. The latter is also supported by looking at the gradient itself for the four fibers which has a low error and its similar for every sample prepared. In addition, both ends also exhibit a low error factor ($< 2\%$) which shows that higher and lower stiffness values can be replicated by applying the same conditions on the fiber fabrication process. The slight fluctuation in the middle values can be accounted to experimental error factors such as the existence of dust or particles that might exist in the channel or the mixture, or the application of the temperature gradient that is manually adjusted throughout the experiment and may rarely result to a seconds long overshoot of the temperature during the adjustment. Overall, the method can be considered

as reproducible and simple to use, as it was performed by several master students that yielded valuable results being trained only a short time on the operation of the microfluidic setup.

Exploring a new type of gradient

The swelling ratio of the material was another factor that needed to be investigated as hydrogels alter their mechanical properties in accordance with their swelling or de-swelling ratio.^[290] Oddly, the GG fiber did not display any swelling behavior and the gellan network collapsed entirely upon removing all the water content from the material. As the fibers are consisted of 99% of water, they form water-based hydrogels that maintain their structure only when found at an aqueous environment. In addition, the quantity of the water content of the fibers is only a few microliters which can rapidly evaporate once the material is exposed to the environment. Consequently, a mechanism similar to the exchange of solvents takes place and the material shrinks due to capillary stress.^[291]

Nevertheless, the stiffness gradient is preserved as the material shrinks over time, although the overall YM values are elevated. It was observed that as the fibers dehydrate slowly over time the overall stiffness increases up to 100 times more, though the stiffness gradient is always present. For that reason, a gradient GG fiber was slowly immersed in deionized water leaving the one end more exposed to ambient than the other, creating a gradient of dehydration along the material length.

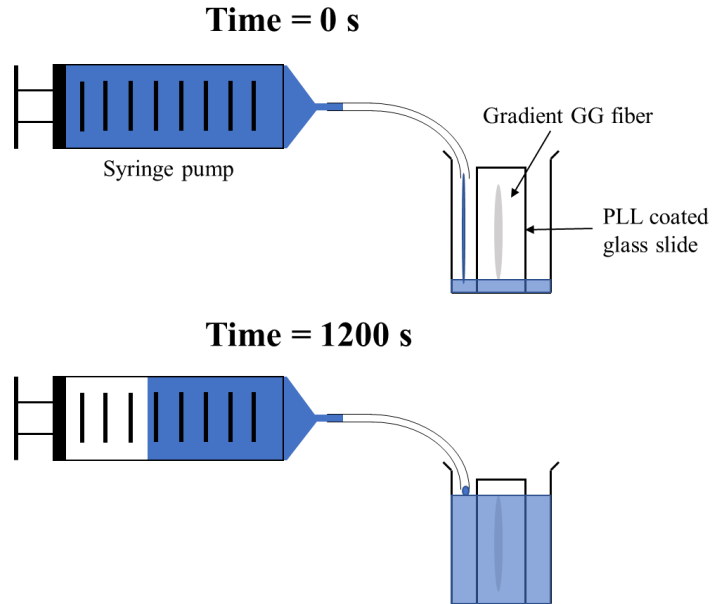


Figure 44: Schematic of the procedure followed during the x-axis stiffness gradient formation. A syringe pump is slowly filling the beaker containing the gradient GG fiber which is placed at a vertical position.

The 2 cm long fibers were firstly attached onto a glass slide (PLL or pre-treated as mentioned before) and then left vertically to a glass beaker. By using a syringe pump the beaker was slowly filled with water at a rate proportional to the length of the material, so as to fully immerse the fiber after 20 minutes (Figure 44). The hydrogel's stiffness profile across its surface was then examined using the AFM and it is shown below on Figure 45.

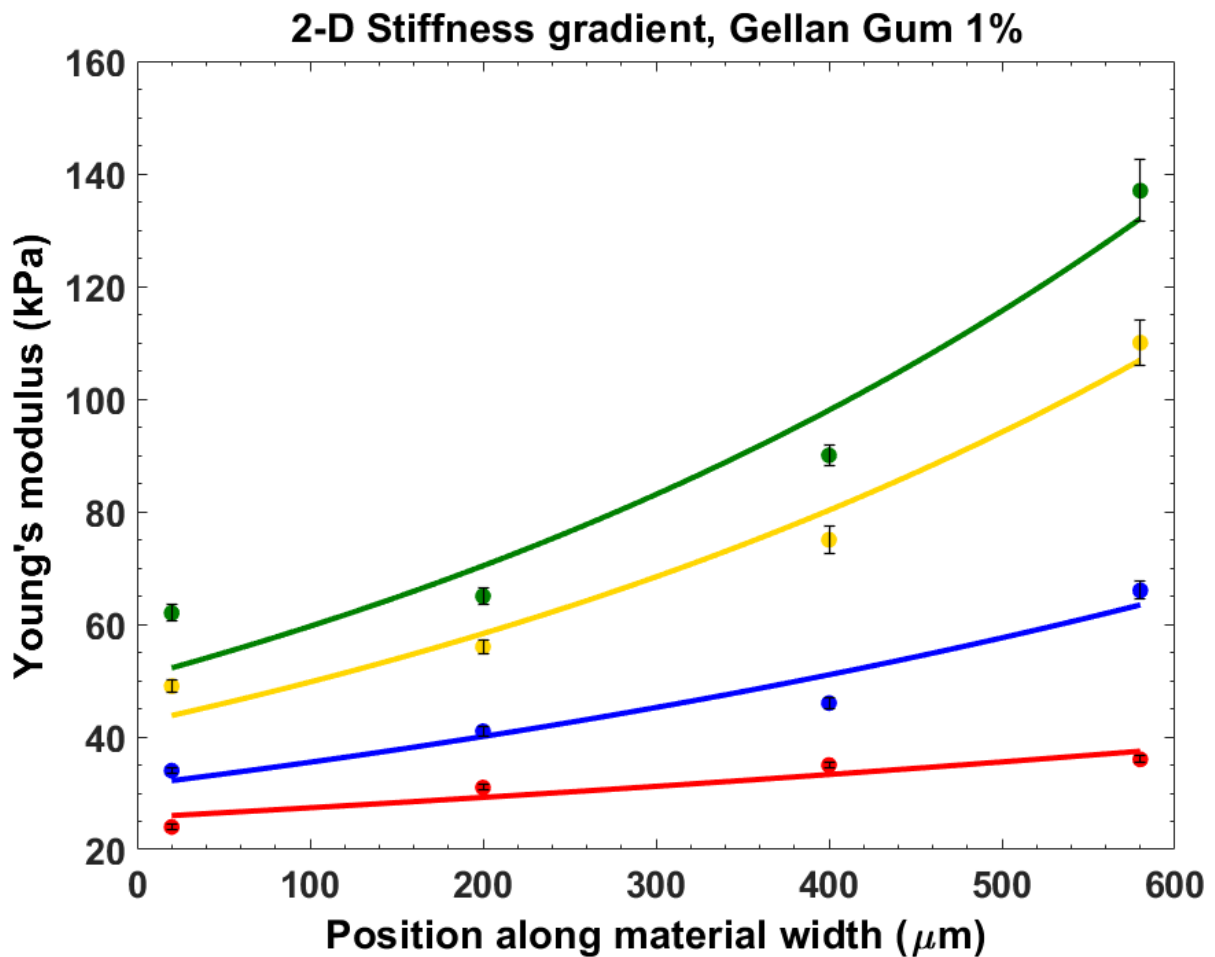


Figure 45: Two-dimensional stiffness gradient towards the length and the width of the material. Position along the width is exhibited on X-axis, Young's modulus on Y-axis and position across the length of the material is illustrated with curves of different color for each individual area. The position along the length of the material was approximated every 0.5 cm with the softest area to be the red curve, followed by the blue, the yellow and the (stiffer) green one. Error bars represent standard error. Exponential fit was used for creating each trendline. Each point represents the average of a 20x20 μm area with 25 contact points.

As seen from the figure above, the gradient now extends towards two directions the width and the length of the material. The softer region of the fiber ranges from 23 to 62 kPa whereas the stiffer one from 37 to 137 kPa. This new type of gradient broadens the stiffness range and the capabilities of the substrate for future cell culture studies. For example, mesenchymal stem cells could be placed on the surface of the 2-D stiffness gradient fiber to investigate their differentiation over time for obtaining valuable information on cellular interactions at the transitional region of bone and cartilage tissue. In addition, the interaction between the different

cell phenotypes would be of great interest especially for the cases such as the osteochondral interface, that was previously mentioned in the literature review.^[4] In this case substrate stiffness could strongly influence the differentiation of stem cells as they form cartilage tissue usually between the region of 20-30 kPa and bone tissue on harder substrates (over 30 kPa).^[292]

The capabilities of the microfluidic device and the phenomenon of thermophoresis were previously investigated to demonstrate an effective control over the mechanical properties of GG fibers. Furthermore, this novel technique is not limited to GG or NaAlg hydrogels as the microfluidic manipulation platform is independent from the polymerization part which potentially expands its applicability to multiple hydrogel systems. In conclusion, the three main pillars of this research project were established, namely the innovative microfluidic device, the applicability to any biocompatible hydrogel and the tunability of several mechanical properties of the material. Though, the main research goal is to accurately mimic the tissue microenvironment and study the cellular interactions on the gradient substrates. For that reason a series of biological experiments were conducted to investigate the bio-functionality and the biocompatibility of the gradient GG fibers.

Biological experiments

The establishment of the microfluidic manipulation technique placed the foundations for further exploring potential applications for the newly fabricated gradient biocompatible hydrogels. The objective of controlling the mechanical and structural properties of biomaterials through the phenomenon of thermophoresis could possibly be expanded to the regulation of cell activity. This novel method could be proven to be beneficial not only for fabricating 3-D scaffolds with certain mechanical specifications but also for influencing cell behaviour. Such

an achievement could provide us with crucial information and insights on cell-substrate and cell-cell interactions that could potentially lead to the design of more advanced 3-D scaffolds in the future. Therefore, the impact of the stiffness and the porosity gradient of the biomaterials in the cellular activity over time was further examined as it is considered a matter of great importance especially for future tissue engineering applications.

The first step towards this direction was cell cultures and the selection of the appropriate cell type. All the biological experiments were carried out at either the biochemical engineering department or the healthcare technologies institute of the University of Birmingham, as cell culture research must be conducted under a completely sterile environment. One of the main requirements of a cell culture laboratory is the presence of a laminar flow hood which blocks the entry of micro-organisms (such as bacteria, fungi etc.) and dust into the main cabinet, thus creating an isolated and sterile environment.

The selection of the suitable cell type depends on several factors. The first one is the tissue type that we want to investigate. For this study, the bone-cartilage interface was selected as the main area of focus. Therefore, cell types that stem from bone tissues should be selected. Another factor that needed to be considered is the environment that cells prefer in order to exhibit cell activity such as proliferation, differentiation, mineralization etc.^[9, 293, 294] In this case, the term environment refers to the substrate stiffness range in which the cells will be functional,^[294] as this is the main parameter we control effectively using thermophoresis. Bone and cartilage cells can be cultured around the stiffness range of the gradient GG fibers that were previously fabricated, making them a suitable candidate.^[295, 296] Yet, there are plenty of cell lines associated with these type of skeletal tissues.^[297] One of the lines that is commonly used in cell culture studies are osteoblasts.^[298] Osteoblasts proliferate and form groups of connected cells to build bone tissues.^[299] They derive from differentiated mesenchymal stem cells (MSCs) when cultured at a substrate stiffness range from 25 to 40 kPa.^[56] All of the above,

make osteoblasts a suitable candidate for the upcoming cell culture studies that were performed on the gradient GG fibers.

The experimental planning involved the seeding of osteoblasts (cell line MC3T3) derived from mouse calvaria onto the stiffness gradient hydrogels and the monitoring of their activity over time. At first, the term activity related to parameters such as cell viability, migration, density and spreading. Cell viability was the first step towards investigating the biocompatibility of the gels, whereas migration, density and spreading are more associated with the influence of the stiffness gradient on cell behaviour.^[9] The expected outcomes are related with the observation of osteoblasts migrating, spreading and eventually forming tissues towards the stiffer region of the biomaterials. A further quantification of cell spreading, density and viability will further support their “preference” of stiffer substrates.

On the other hand, a major drawback of this study is the incorporation of cells in the material. As GG fibers are prepared at a relatively high temperature (average 60-70 °C) for a long period of time (20-30 minutes), cells could not be added in the GG mixture and subsequently embedded within the fibers, as they will be either damaged or stressed. For that reason, osteoblasts will have to be seeded at a later stage on top of the biomaterials. Consequently, monitoring cell activity over time on the stiffness gradient substrates was carried out as a 2-dimensional study, due to the fact that osteoblasts were only found at the surface of the 3-dimensional GG fibers. Though, this study could serve as an initial proof concept, setting the protocols and laying the foundations for future studies on gradient 3-D scaffolds. As mentioned before the microfluidic platform could potentially be converted for manipulating the mechanical properties of other type of biomaterials such as gelatin methacrylate, collagen etc., which can potentially embed cells during the fabrication process and thus making the biological assessment a 3-D study.

1. Material sterilization

The first step towards cell culture experiments, was to identify the parameters that influence cell growth such as sterilization and cell seeding density. One of the major prerequisites in cell cultures is the presence of a sterile environment, as previously mentioned. As GG fibers were prepared and assessed at a non-sterile environment, they most probably contained several micro-organisms such as bacteria which will inhibit cell growth and proliferation. Therefore, the biomaterials needed to be sterilized before depositing cells across their surface.

There are multiple ways to sterilize a sample or a surface some of which include, autoclave, UV irradiation and ethanol spraying.^[300] These are the three most popular techniques that are widely used due to the fact that they usually do not damage the specimen or the material to be sterilized.^[300] However, the micron sized GG fibers can easily be affected by those factors, damaging their substrate or even altering the gradient.^[301, 302] For example, ethanol immersion will result (as previously mentioned in the SEM section) in the shrinkage of the material but also it might leave traces of EtOH within the material which might prove to be toxic for the cells.^[302, 303] In terms of autoclave, GG is a thermally reversible material which might partially transition back to liquid state or alter its mechanical properties (such as the stiffness gradient previously formed) once high temperatures and pressures apply.^[304] The UV treatment technique though has not been fully investigated and often researchers debate whether it is altering or degrading the surface modified 3-D scaffolds when applied for a long period of time.^[301, 305] Though in comparison with the previous methods, it offers a short processing time at a low temperature with a minimal cost of operation, making it a suitable and promising candidate for sterilization applications in biocompatible scaffolds.^[300]

A series of tests were conducted to establish a sterilization protocol which will ensure a nontoxic environment for cells whilst maintaining the integrity of the stiffness gradient across the GG fibers. At first materials were placed under the UV lamp of cell culture hoods for 2 hours immersed in deionized water onto sealed plastic petri dishes. Still, that method was ineffective as UV light does not penetrate through the plastic (polystyrene) dishes which led to the removal of the lid and the placement of the samples as close as possible towards the UV light. An improvement on the biocompatibility was achieved, though almost half of the samples were contaminated over time which raised some concerns on the sterilization method.

For that reason, the UV irradiation method was further optimised. The level of deionized water in the petri dish was lowered down to the amount required to keep the material hydrated throughout the process. Also, a UV chamber was used instead of the cell culture hoods with a UV lamp of 254 nm of wavelength and 13 Watts being positioned right above the samples. To ensure sterility and prevent the open-air samples from getting infected once the UV lamp was turned off, polyethylene airtight bags were used to enclose the open lid petri dishes. The bags were previously tested for their permeability in UV light using a radiometer which revealed that UV was not blocked by the plastic bag. The bags containing the samples were UV sterilized for 5 minutes directly under the lamp for preventing any shadowing effects from the dishes' walls and were subsequently sprayed with ethanol before placed and opened in the cell culture hood.

The GG fibers were then transferred in 6 well plates as an extra safety precaution against contaminants. This updated method greatly improved the sterility of samples and minimized the contamination incidents. Although, the only question remained was the effect of UV light on the stiffness gradient of the materials. As energy is emitted from the UV lamp to the sample, it slowly heats up which might potentially damage its microstructure. Hence, a simple AFM test before and after the application of UV irradiation would answer the question of the UV

effect (Figure 46). The tests were performed on a 1% GG fiber that was kept for 30 minutes in a temperature gradient of 4.5 °C/mm. The fiber was force mapped before and after the UV treatment on the same spots locally at 4 points across the 600 μm wide fiber.

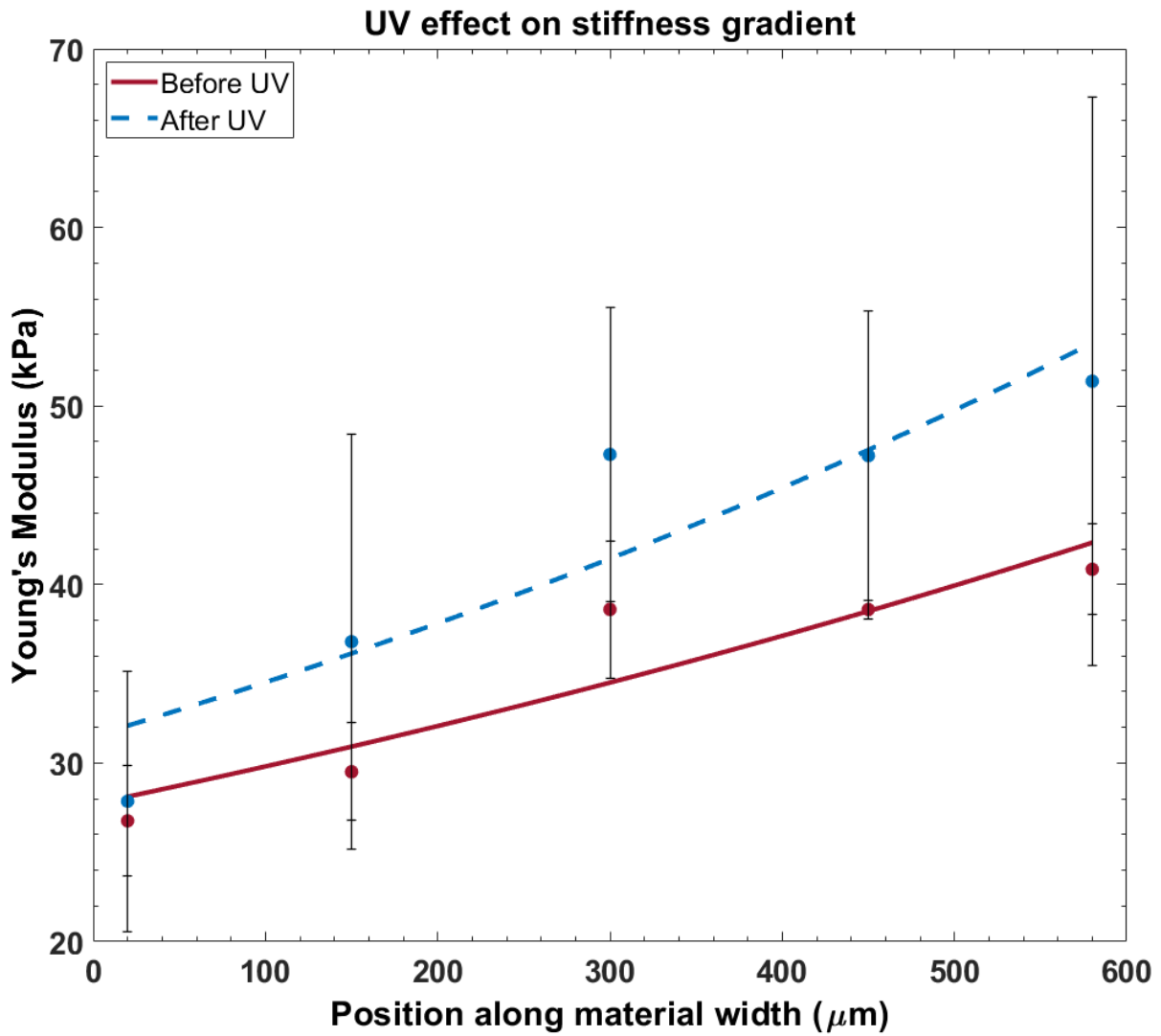


Figure 46: UV effect on the stiffness gradient of 1% GG fibers before and after its application. Error bars represent standard error. Exponential fit was used for creating each trendline. Each point is the average of 3 areas on the same width position across the length of the same fiber.

We can observe that the stiffness gradient is slightly affected and the YM values are within a certain range of stiffness. The difference between those two curves could be attributed to the fact that the AFM is a delicate method that can measure an area of a few microns (20x20

μm) which of course generates an acceptable and minor experimental error. In addition, the standard error bars overlap each other which confirms the acceptable experimental error. To conclude, a method to ensure the sterility of the biomaterials was established and further optimized before proceeding to the cell culture experiments.

2. Biocompatibility optimization

To further optimize the biocompatibility and in extend the viability of the substrates, we considered the incorporation of cell nutrients and proteins in the material. The simplest solution to this issue was to replace a portion of the solvent (in this case deionized water) with cell culture medium, which contains proteins, antibiotics and other substances that are considered beneficial for the cells. Nonetheless, such a vast change to the initial solution might affect the overall gradient and at the same time it might create a nutrients gradient which could potentially influence cells, for or against the stiffness gradient. The first problem was easily solved by simply testing the material made with cell culture medium, under the AFM and comparing the YM values with the past results. As seen on the Figure 47 below, a 1% GG fiber supplemented with a-MEM cell culture medium was tested under the AFM to investigate any alterations to the stiffness gradient. It can be observed that the stiffness gradient is maintained but the overall stiffness is slightly increased which could be attributed to the additives of the cell culture medium.

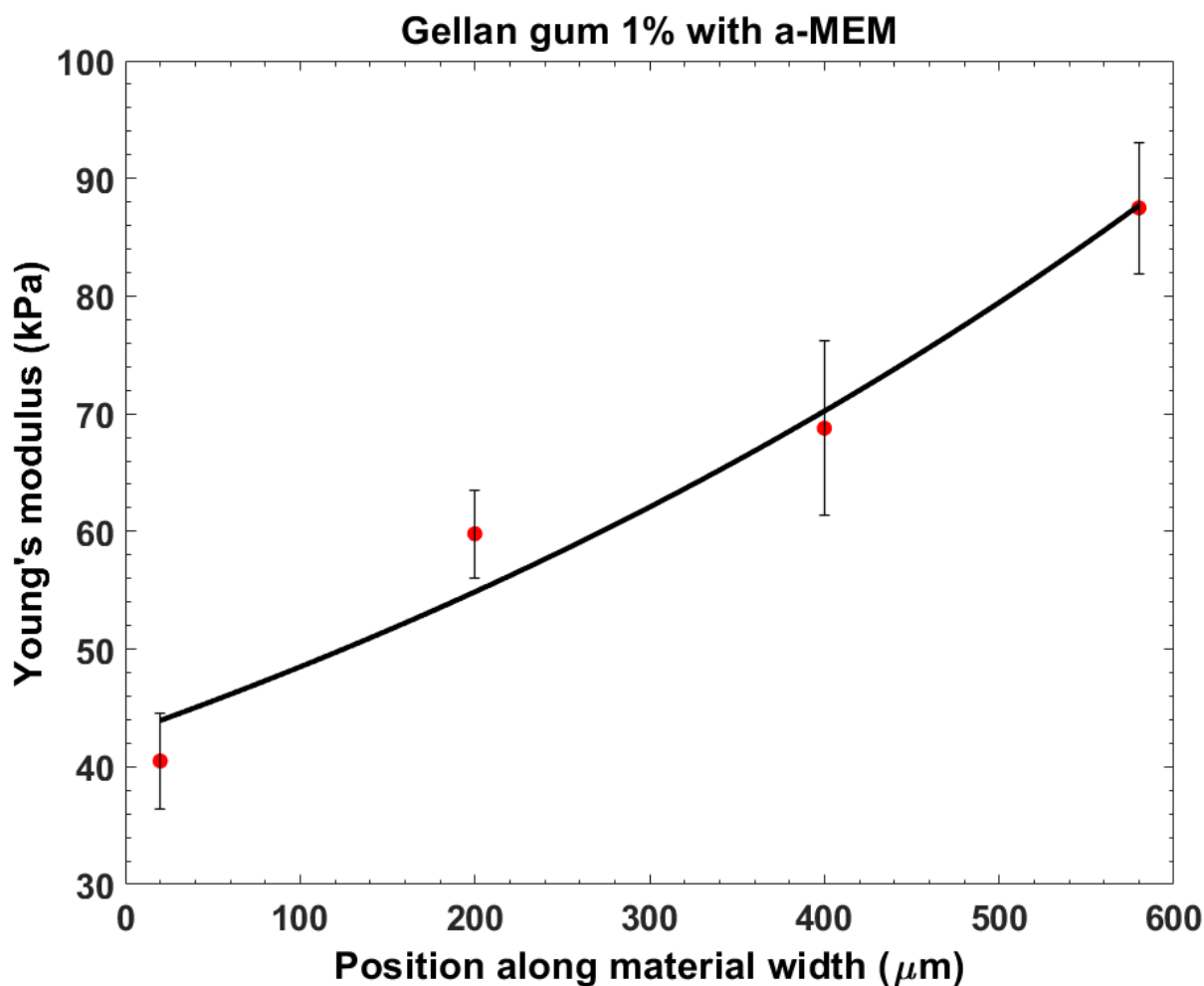


Figure 47: GG 1% w/v supplemented with a-MEM stiffness gradient. Error bars represent standard error. Exponential fit was used for creating each trendline. Each point is the average of 3 areas on the same width position across the length of the same fiber.

Cell culture medium contains inorganic salts, amino acids, vitamins, and other substances. To promote cell activity, it needs to be supplemented with antibiotics (penicillin/streptomycin), L-glutamine and proteins (FBS).^[306] The later (FBS) is the main growth factor essential for the maintenance and growth of cultured cells. As the main driving force, it could be easily be responsible for the formation of a biological cue gradient that could affect the stiffness one. However, FBS is pre-mixed at the GG solution which experiences temperatures over 70 °C for over 30 minutes, resulting at the denaturation of the protein, thus

inhibiting its action.^[307] It is known that FBS is denatured when heated above 56 °C for approximately 30 minutes.

Another technique that was used to improve the biocompatibility of the substrate was the application of an FBS coating on top of the material. That would require the immersion of the sterilized gg fibers in FBS solution overnight, followed by a subsequent thorough washing with PBS before depositing the cells on the surface of the material. However, the main drawbacks of this method are both the protein gradient that could potentially form due to the increase in binding spots towards the stiffer side which would influence cell activity and also the obstructed vision under the confocal microscope. The latter is caused by the amine-groups of the FBS coating which bind to the amino-reactive fluorescent dyes, producing a lot of background noise when excited by the laser of the confocal microscope.^[308] As for the protein gradient, it is known that cell activity is mainly influenced by two major factors, substrate elasticity and biological cues such as focal adhesions.^[309] Subsequently, by applying an FBS coating on the material it would make it extremely difficult for us to distinguish if cell activity is regulated due to the stiffness gradient induced by thermophoresis or due to the protein binding sites across the surface of the material generated by the coating. For all the reasons mentioned above, this technique was quickly abandoned.

Below, in Figure 48, we can observe the live dead confocal images from 3 different biocompatibility improvement techniques on GG fibers:

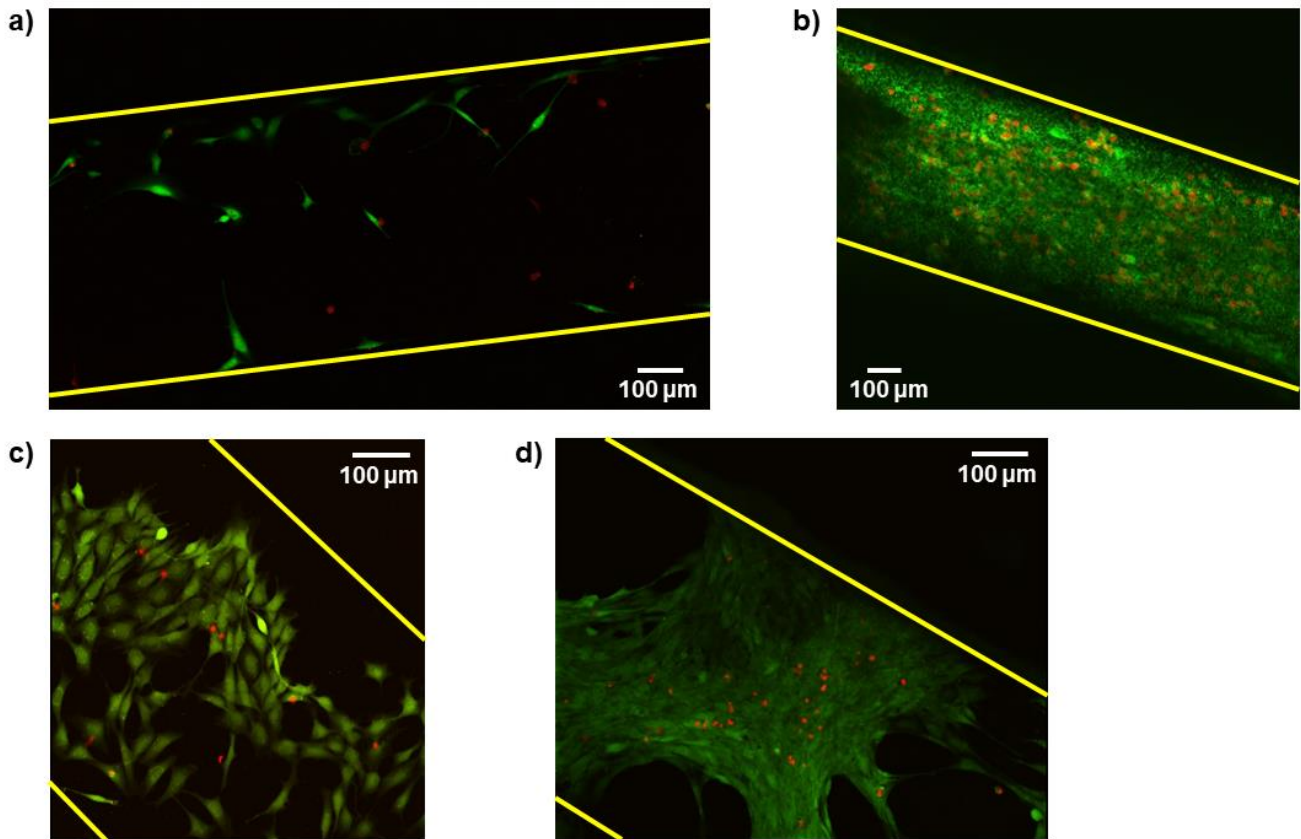


Figure 48: Visual inspection for the determination of the biocompatibility of different substrates seeded with MC3T3s and stained with calcein AM and propidium iodide on day 3. The substrates exhibit uniform stiffness. a) Material made with deionized water, b) Material with FBS coating, c) Material made with a-MEM on day 1, d) Material made with a-MEM. Yellow lines highlight the boundaries of the uniform GG fibers.

A visual inspection of pictures a-c on Figure 48 provides us with the information about the optimal method to improve cell viability and attachment to the surface. All the materials were loaded with a high cell seeding density of 2×10^4 cells/mm² and left for 24 hours in the incubator. Only a few cells can be spotted across the surface of the DIW material which indicates the lack of adhesion on the fiber as well as the preference of cells towards the supportive glass slide that lies underneath. The number of seeded cells was the same in all of the experiments, which means that the ones deposited on top of the DIW material were easily washed away, probably due to the weak adhesion between the osteoblasts and the substrate.

On the other hand the FBS coated material is full of healthy and well spread osteoblasts, though our vision is obstructed by the interference of the fluorescent signal of FBS. A green signal seems to overlay the confocal live dead image of osteoblasts on the material and that is mainly the reason why an FBS coating was not applied to the material. Fig 15c, d demonstrates the 1% GG fiber that was supplemented with a-MEM mixture beforehand which greatly improved the cell attachment and biocompatibility of the substrate. At day 1 we can observe a large population of healthy osteoblasts well-spread across its surface, and after 2 more days (on day 3) we are able to see the network of healthy cells that has developed on the fiber.

We can therefore draw the conclusion that replacing a portion of the deionized water that acts as a solvent with cell culture medium (a-MEM) has a great impact on cell attachment and viability on the substrate. Consequently, this technique was utilized for all the materials that were fabricated and used at any cell culture experiment.

3. MC3T3 cell cultures *in vitro*.

At first, cell populations were obtained from the liquid nitrogen storage tank, following a subsequent thawing of the cell-medium-DMSO mixture. Subsequently, they were immediately placed into cell culture flasks for further expansion upon the removal of the DMSO-medium solution that was previously used for freezing purposes. The cell culture medium (a-MEM supplemented) was refreshed every 2-3 days and cells were passaged each time they covered approximately 70% of the culture flask. After a week of expansion there was a sufficient number of healthy MC3T3 cells that could be used later for depositing on the GG fibers.

The first few sets of experiments were performed to obtain preliminary data and feedback from the cell-material environment, in order to carefully plan and execute the following live dead assays. The parameters that needed to be set were primarily the duration of the cell culture on the gradient GG fibers and in accordance the initial cell seeding density so as to ensure that a sufficient number of cells is found on the surface of the material after several days of culture. Initially, the live/dead assay experiments were set to 7 days of culture for allowing cells to adhere to the substrate and then migrate and proliferate across the surface of the materials.^[310] In addition, a confocal microscopy of the cultures on the days 1, 3 and 7 was carried out to further investigate cell behavior over time.

However, the density of the cells across the substrate at the initial seeding process, should be both sufficient and at the same time not excessive so as to have a reasonable number of cells after 7 days of culture. The substrate after 7 days, should have enough cells to carry out a live dead assay and study the different cell spreading or densities locally but it should not be entirely covered by osteoblasts as that will impede all of the studies that were previously mentioned. For that reason, the optimal initial cell seeding density had to be established. A series of trial and error tests as well as an approximate calculation based on the cell size and growth rate were made to determine the optimal cell density on the surface of the fibers.

A. Cell seeding density

The procedure that was followed to deposit the cells on top of the scaffolds was previously described in detail at the protocols section. Briefly, a cell suspension was prepared by extracting, centrifuging, and re-suspending MC3T3s from the culture flasks. Subsequently, the cells were deposited on top of the fibers and they were left for 3 h in the incubator, prior to

the filling of the wells with a-MEM, for allowing them to adhere to the substrate and prevent them to be washed away during the cell culture medium addition. The wells were later filled with 3-4 mL of cell culture medium which was replenished every 3-4 days depending on the cell population. After 7 days the cells were stained using fluorescent dyes such as Calcein AM and Propidium Iodide to visualize the live and dead cells respectively under the confocal laser microscope.

At first, three initial suspension of 2×10^5 , 1×10^6 and 2×10^6 cells/mL were prepared and 1 μL per mm^2 of surface area were placed on the biomaterials for each of the 3 cell suspensions, to evaluate the coverage of the fiber's surface by osteoblasts after 7 days of culture. Although, the suspension quantity was low and evaporated quickly after 3 h which led cells to die in the lack of nutrients. For that reason, the suspension quantity that was deposited on the materials was increased to 20 $\mu\text{L}/\text{mm}^2$. As seen on Figure 49 both 1000 and 2000 cells/ mm^2 samples were observed with an excessive number of cells across their surface, whereas the low concentration one did not present a sufficient number of cells. The latter could be attributed to the fact that the amount of cell suspension deposited on the materials was excessive, often spilling at the supportive glass slide below the fiber, which led cells to sediment at a preferably stiffer substrate (glass). Regarding the higher concentration samples, the amount of cells found on the material surface after 7 days was excessive therefore a lower concentration needed to be used, though in accordance with the reduction of the suspension quantity.

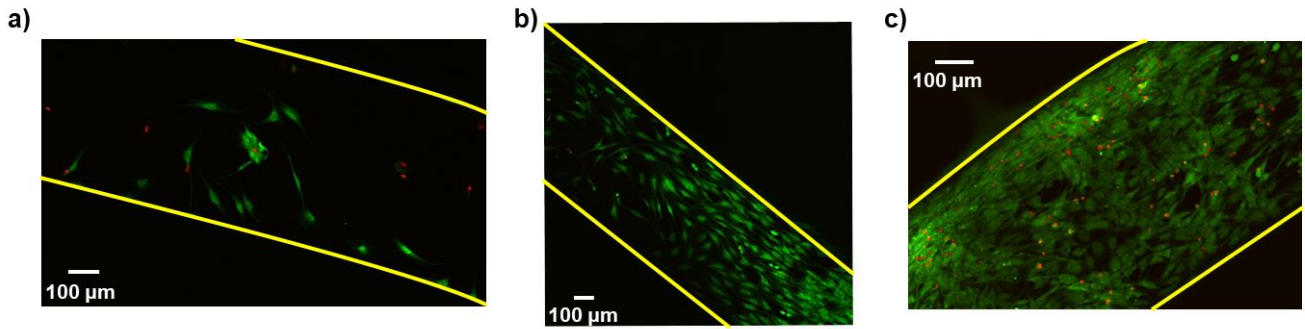


Figure 49: Different cell seeding densities of MC3T3s across the GG fibers exhibiting uniform stiffness with a seeding density of: a) 200 b) 1000 and c) 2000 cells/mm². Calcein AM and propidium iodide were the selected cell stains. Yellow lines highlight the boundaries of the uniform GG fibers.

For that reason, the optimal cell suspension concentration was established at 500.000 cells/mL, with a quantity of 1.7 µL/mm² to be deposited on top of the material, ensuring that both the right amount of cells are seeded and also there is plenty of cell culture medium to keep them alive during the 3 h incubation period. As seen on Figure 50, the material seeded with the optimal concentration (around 850 cells/mm²) seems to be covered with the right amount of osteoblasts across its surface on day 7, allowing us to distinguish individual cells and grouped cell populations clearly, without overlapping each other.

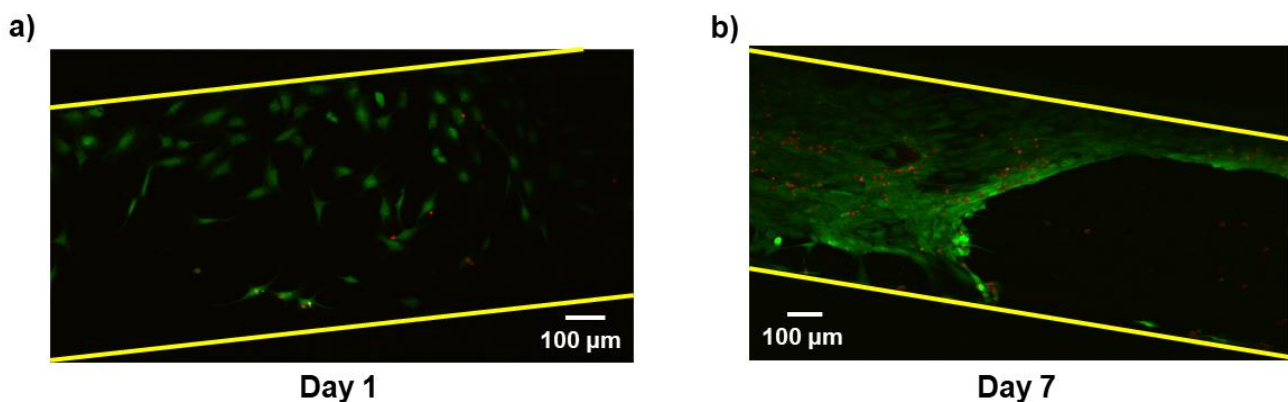


Figure 50: Optimal cell seeding density of 850 cells/mm² deposited on the surface of the uniform stiffness GG fibers after a) 1 and b) 7 days. Calcein AM and propidium iodide were the selected cell stains. Yellow lines highlight the boundaries of the GG fibers.

B. Live/dead staining

Since the optimal cell density was established and the biocompatibility of the material was previously improved, a series of cell culture and live/dead experiments were carried out to investigate cell activity over 1, 3 and 7 days of incubation. The cells were deposited on top of the gradient GG fibers in random positions across their surface to potentially observe migration as well as improved proliferation, locally towards the stiffer side of the material. A series of gradient GG fibers were loaded with the same number of cells and left to incubate for 1,3 or 7 days. Each sample was then removed from the incubator on the specific day of interest, its cells were dyed with Calcein AM and PI and it was imaged using a confocal microscope. Each sample was only used once, meaning that we observed 3 different days of culture (1, 3, 7) on 3 different samples which exhibit the same stiffness gradient as well as initial cell seeding density. In Figure 51, it can be seen that at day 1 the cells are initially clustered or randomly scattered across the surface of the fibers exhibiting a round morphology which indicates a weaker adhesion and a premature stage in terms of cell proliferation and elongation. As we move to day 3 the cells slowly migrate towards the stiffer side of the substrate, where more elongated cells are found in comparison with the rounder ones at the softer side. At day 7, osteoblasts have established across the stiffer part of the fiber and it can be observed that cell spreading is improved as we move towards the stiffer end.

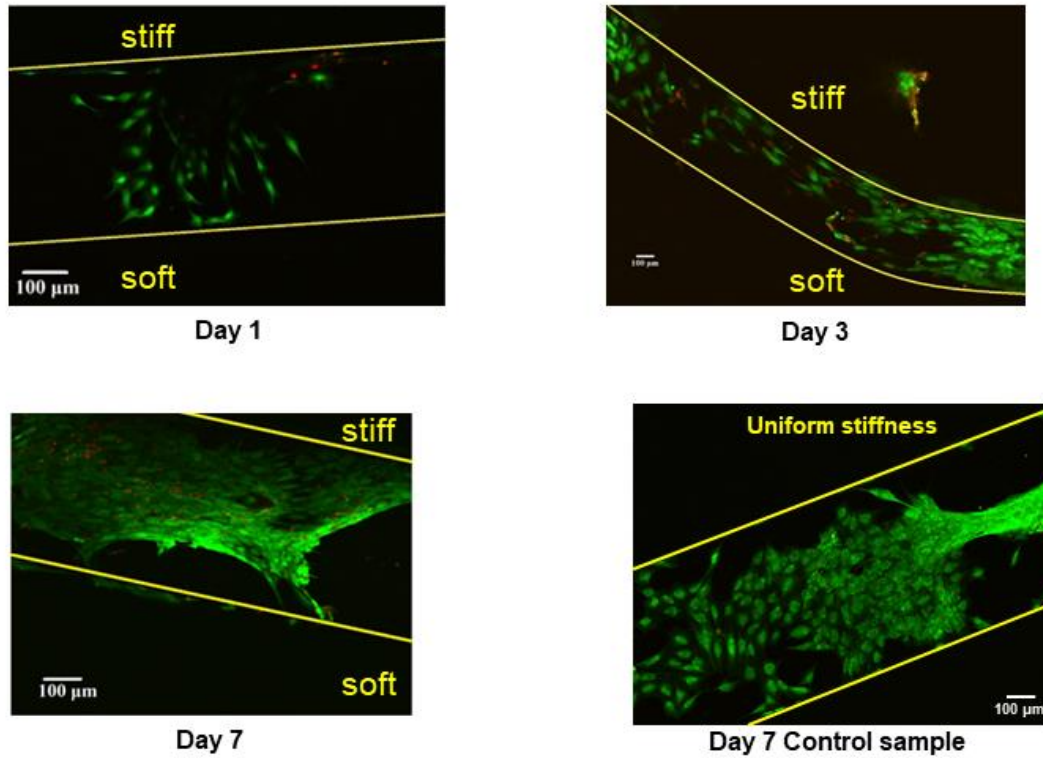


Figure 51: Migration and proliferation of osteoblasts (MC3T3) over 7 days of culture onto the stiffness gradient 1% GG fibers. Day 7 control sample is exhibiting uniform stiffness. Day 1, 3 and 7 were selected as the time markers for confocal imaging. Calcein AM and propidium iodide were the selected cell stains. Yellow lines highlight the boundaries of the GG fibers.

From Figure 51 we can visually observe the difference in the cell populations between the stiffer and the softer area of the fibers as well as improved cell migration and proliferation towards the stiffer side. These claims are further supported upon the image processing of the pictures above using ImageJ software. The table below (Table 2) summarizes the data generated from the images above, regarding cell density for both stiff and soft sides which exhibit the improved proliferation and migration of the cells. The experiment was repeated 3 times with different fibers that exhibit the same stiffness gradient, to validate the differences observed between the two stiffness areas (soft and stiff). Though, the cell number attached on each material varies, potentially due to the different material and cell batch used, resulting at

different cell densities observed between the repetitions of the experiment. However, the difference in the cell density between the 2 areas is similar throughout the 3 repetitions and an average of that difference is demonstrated below with a standard error added next to each value.

Table 2: Cell density difference of MC3T3s (expressed in %) between the soft and the stiff area of 3 independent stiffness gradient fibers that were incubated for 1,3 or 7 days. Control sample is a uniform stiffness fiber cultured for 7 days. The average difference is calculated from 3 independent samples that were prepared for each day of culture (3 data sets of images similar to Figure 51), with the errors reported as standard error.

Sample	Cell density (cells/mm ²)	
	Avg. Difference (%)	Standard error
Day 1	48	± 12.2
Day 3	65	± 24.4
Day 7	303	± 96.5
Control	4	± 12.7

From the generated data above, we can deduct that over time the difference between the soft and the stiff area of the fibers is augmented as cells tend to migrate towards the stiffer end and even proliferate at a higher rate on that area. Negligible difference (<10%) is observed for the control substrate where a uniform stiffness exists across the surface of the fiber. On day 7 we can see from Figure 51 a lot of free space close to the softer end which is further supported by the data analysis of Table 2 where we observe a huge difference in the cell density between the 2 areas.

In addition to the live dead experiments, another set of tests was planned in parallel to investigate cell migration in a more controlled way. The previous set of experiments was conducted to investigate cell viability and to observe a potential cell settling and proliferation towards the stiffer side, as the confocal pictures were taken from different materials that were discarded once the cells were dyed and exposed to ambient. Cell migration cannot be observed directly as the initial position of the cells for the day 3 and 7 samples was unknown. Hence, a

different technique was used to image single cells and track during the 7 days of culture. The materials were seeded and incubated as previously but instead glass petri dishes were used to be able to image the cells without exposing them in ambient (contaminants) and at the same time to prevent laser interference from the dish's lid.

C. Cell migration

Moreover, a different type of fluorescent dye was used. PKH67 Green fluorescent cell linker was employed, as it is a non-toxic dye that is incorporated to the cell membrane and lasts for up to 4 generations upon cell mitosis. The cells were dyed before being deposited on the surface of the biomaterials, and upon overnight incubation they were imaged using a confocal microscope. The same material could now be placed back to the incubator and re-examined the next day at the same position, making cell tracking a feasible process.

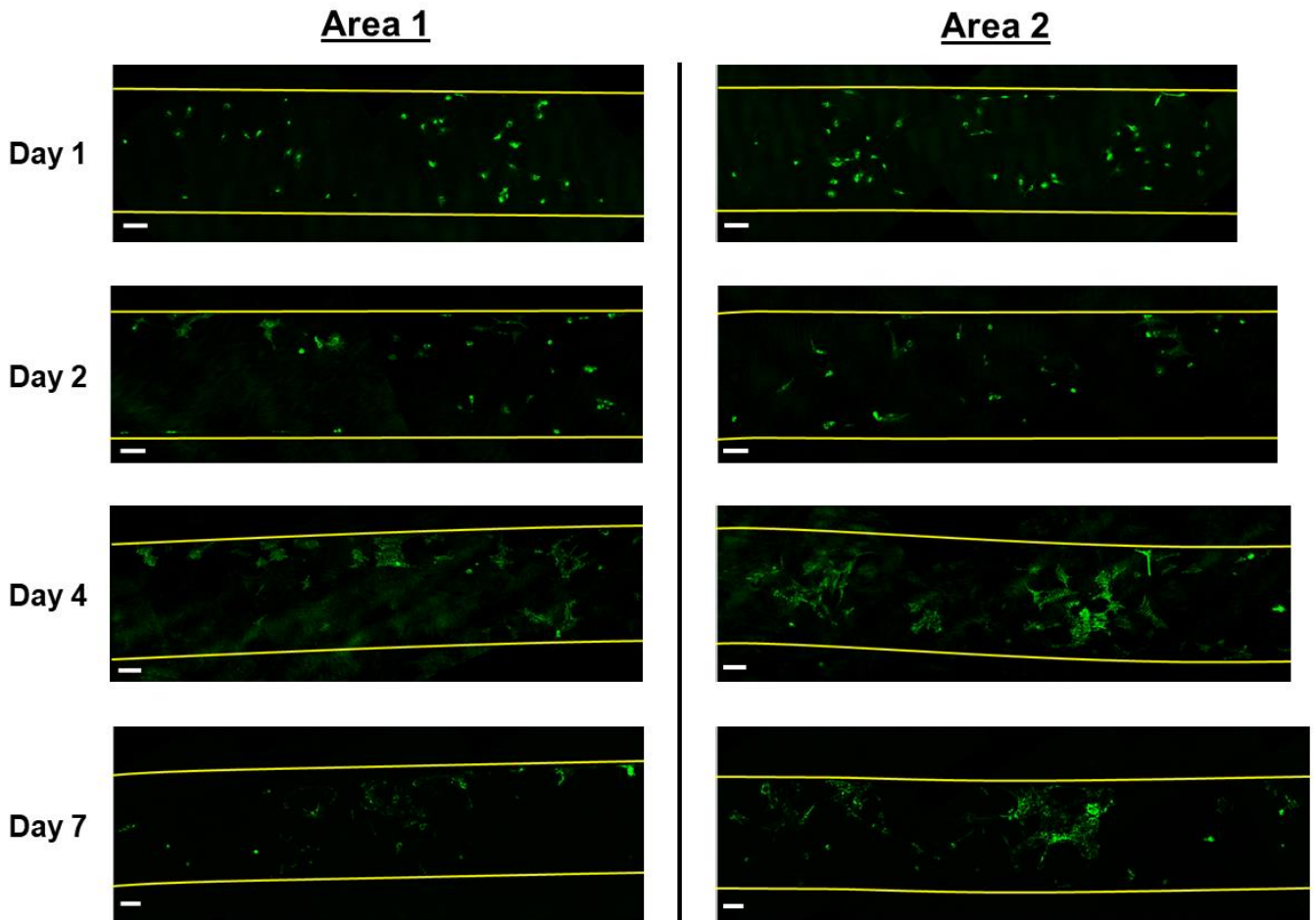


Figure 52: Migration and proliferation of osteoblasts (MC3T3) on the stiffness gradient 1% GG fibers. Confocal images of the PKH stained MC3T3 cells were captured at different time markers up to 7 days of culture. Scale bars represent 100 μm . Stiffer side at the top and softer one at the bottom of each picture. Yellow lines highlight the boundaries of the GG fibers.

As observed on Figure 52 two different areas of the same cell loaded GG gradient fiber on days 1, 2, 4 and 7 were imaged. The PKH membrane stain was maintained throughout the whole week of the experiments, though a significant quantity was released from dead and other cells which generated a lot of background noise especially on days 4 and 7. The cells were at first round shaped indicating a weak cell adhesion with the substrate initially but over time we can observe that osteoblasts spread and proliferate especially towards the top (stiffer) part of the material. From day 2 we can clearly see the spreading and elongation of the cells to adhere

better to the substrate and potentially migrate towards the stiffer regions of the fibers. Unfortunately, a significant number of cells has been washed away during the medium refreshing especially in the softer side which can be attributed to the poor cell attachment with the (soft) substrate. On days 4 and 7 we observe the formation of an osteoblastic network which comprises out of several cells and especially on area 1 this network is formed closer to the top (stiff) side of the fibers. Also, on days 1 and 2 the osteoblasts that were found at the bottom part have later either disappeared (washed away or migrated) or remained idle at a round shape due to the lack of adhesive points on the stiffer substrate. We can therefore deduct the fact that cell migration, proliferation and adhesion is improved towards the stiffer side by simply observing Figure 52 which gives us an overview of the cell behavior over time across the stiffness gradient biomaterials.

D. Cell behavior over time

However, a more quantitative approach needed to be made in order to support the visual claims about improved cell activity on the stiffer side of the material. Parameters such as cell density, spreading and viability could help us understand the impact that the stiffness gradient has on cell activity over 7 days of culture. For that reason, several pictures of the same material were obtained and then recombined to give us an overview of the GG fiber which could be later used for further image analysis. In addition, the bigger area of interest from a single fiber, containing a higher number of cells statistically improves the accuracy of the results in comparison to a single image or multiple images each obtained from different fibers.

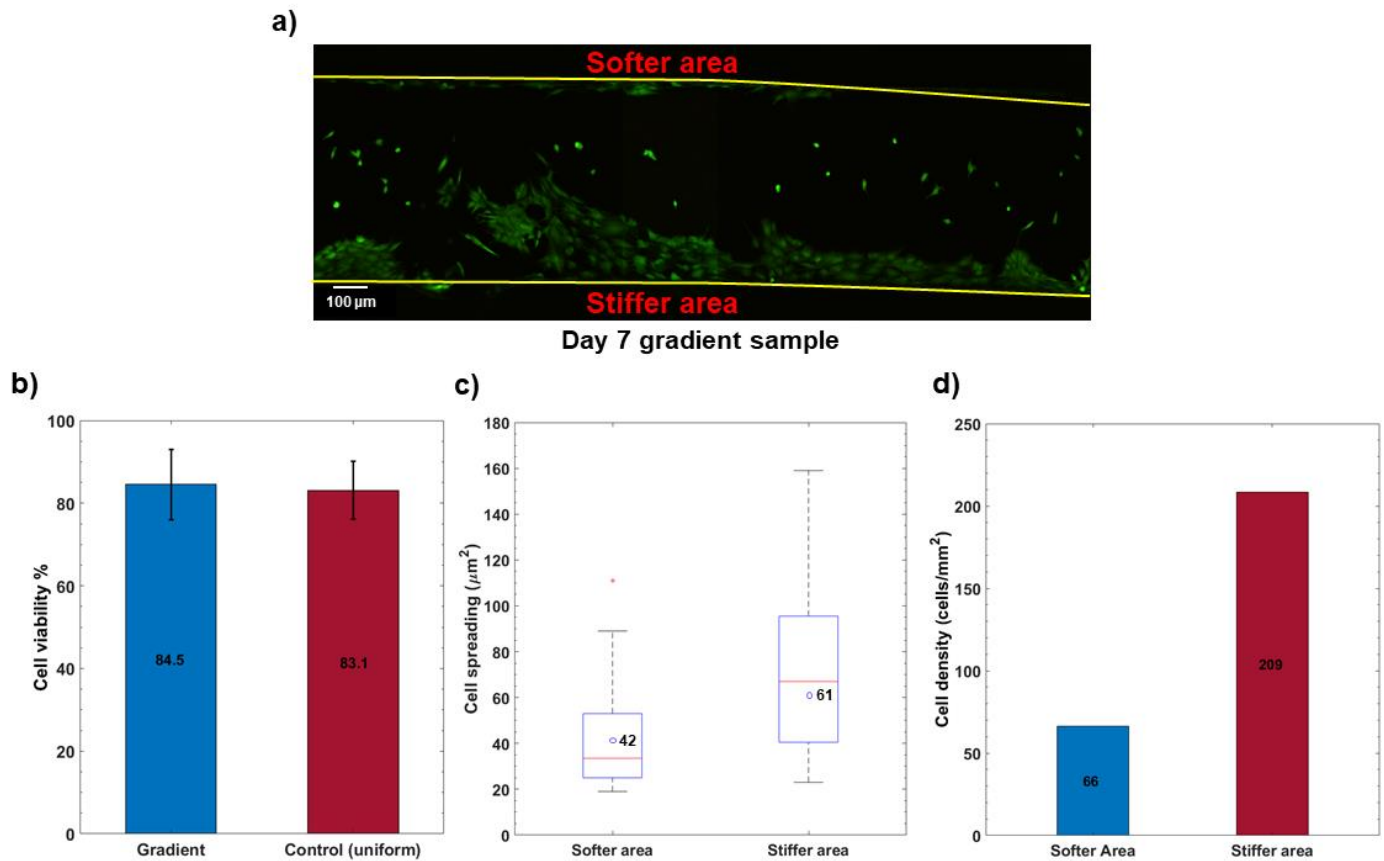


Figure 53: a) Live/dead staining of MC3T3 osteoblasts, on the surface of 1% GG stiffness gradient fibers after 7 days of culture, b) cell viability, c) cell spreading and d) cell density for the 2 different stiffness areas of the material. Error bars represent standard error. Each plot is generated from the extracted data of picture (a) and corresponds to a single stiffness gradient fiber loaded with MC3T3s. Calcein AM and propidium iodide were the selected cell stains. Yellow lines highlight the boundaries of the uniform GG fibers.

In Figure 53 we can observe such an image obtained from a single fiber which exhibits numerous MC3T3 cells across its surface. Using ImageJ software, the confocal pictures were processed to extract quantitative data towards a better understanding of cell behavior on the stiffness gradient GG fibers. The material was split into two parts the higher and lower stiffness areas, which were analyzed to obtain valuable information on osteoblast spreading, density and viability after 7 days of culture. Figure 53c highlights the improved cell activity of MC3T3s on the stiffer side of the material, as cell spreading is improved by 50 % which indicates a better adhesion of the osteoblasts on the stiffer region. A large difference between cell

populations on each area is also observed on the cell density plot (fig. 56d) where the softer side is almost 3 times less populated than the stiffer one, which suggests a better proliferation on that end. In addition, cell viability (fig. 56b) is more than 80% for both control and gradient material which demonstrates that the GG fibers are non-toxic and bio-compatible with the MC3T3 osteoblasts. The difference in cell behavior can be visually observed in comparison with the control sample, where osteoblasts are found randomly spread across the surface of the material as a result of the uniform substrate. Therefore, we can confirm that stiffness is a factor that stimulates osteoblasts to migrate and proliferate towards higher Young's Modulus values which can be used in stiffness gradient systems to control and direct cell activity at specific regions of interest.

Bio-functionality of MC3T3s

The live/dead and cell tracking experiments have provided us with valuable information regarding the influence of the stiffness gradient in osteoblasts over one week of culture. The next goal was to further explore the capabilities of the gradient and investigate other parameters that might be affected by it. The bio-functionality of the MC3T3s was a factor of great interest especially in comparison between two different stiffness regions on the same substrate. Osteoblasts are bone cells that belong to the cell group of fibroblasts and develop from differentiated mesenchymal precursors.^[311] Osteoblastic differentiation though can be split into 3 stages: a) proliferation, b) maturation and c) mineralization.^[311] During proliferation stage ECM proteins are secreted from the cells including fibronectin, collagen I and TGF- β ,^[312] whereas the maturation stage is characterized by the alkaline phosphatase (ALP) expression.^[313] Throughout the last stage of mineralization, genes such as osteocalcin,

osteopontin and bone sialoprotein are expressed, together with a continuous deposition of calcium minerals until the stage is complete.^[312] Stage 1 has been extensively studied so far, with the proliferation of cells being visualized using live dead or PKH staining over 7 days of culture, followed by a quantification of the imaging data using image processing software.

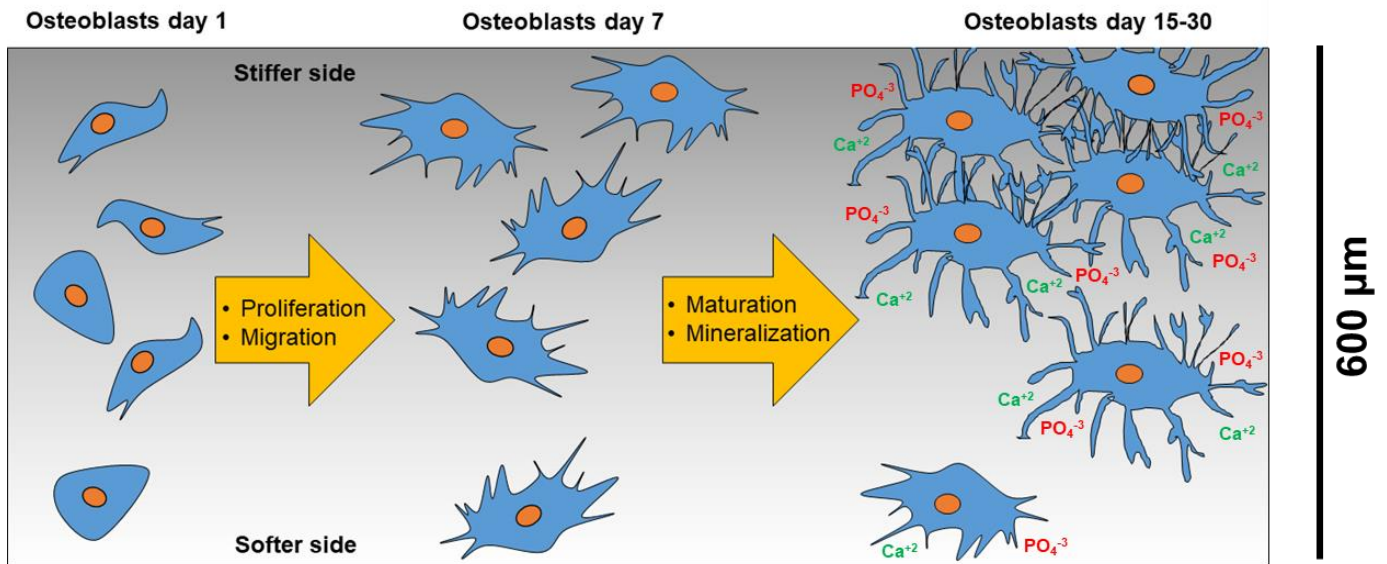


Figure 54: Schematic representation of osteoblast activity on the substrate over time.

Nevertheless, to investigate the effect of the gradient GG fibers on the maturation and mineralization stage of osteoblasts it requires advanced staining or imaging methods in order to detect genes/minerals that are expressed/deposited by the cells. Genes can be detected by using immunofluorescent stains to image each protein with a different colour directly on the substrate, using a confocal laser microscope.^[312] Though, alkaline phosphatase cannot be detected using immunofluorescent techniques and one of the most common approaches is the application of alizarin red, a stain which is visible with an optical microscope.^[313] The main drawback of imaging techniques is the qualitative nature of the results rather than the quantitative one which is one of the main goals of this research project as we move towards the investigation of the bio-functionality of the osteoblasts. Confocal images with different

stains can only be quantified using image processing software by looking at different intensity profiles across the fiber, which would of course generate an estimation rather than accurate data.

For that reason, we further investigated the available imaging techniques that would allow us to accurately calculate both ALP and calcium data to detect how maturation and mineralization are affected by the gradient substrate. The optimal technique was found to be X-Ray Fluorescence (XRF), as it can detect elements and their quantities on surfaces up to a few microns deep.^[314] We would be able to access the phosphorus and calcium quantities that cells produced over time as they transitioned from the proliferation to the maturation and mineralization stage. Therefore, the cell loaded GG fibers were incubated for a longer time to ensure the deposition of both minerals on the matrix, before imaging their surface under the XRF.

1. XRF experiments

The time markers that were established were the 15 and the 30 days for studying the incubated cell loaded materials under the XRF. It was expected that a 30-day cell culture would yield much clearer results than the 15-day one as cells will have more time to migrate, proliferate, undergo their maturation stage, and most importantly mineralize the substrate. The gradient GG fibers were now loaded with cells as previously, with the same number of cells per surface area and the medium was refreshed every 3-4 days for up to 30 days of culture. As the XRF requires the material to be exposed at a non-sterile environment for a period of time each sample that was examined was later discarded so as to prevent a potential contamination within the incubator. In addition, control (uniform stiffness) samples were also cultured for 15 and 30 days to compare the activity of the gradient fibers with a reference substrate. Also, we

introduced the use of osteogenic medium to promote growth and mineralization rate of the osteoblasts for using as a positive control experiment and yield clearer results on the influence of the gradient on cell activity. Osteogenic medium is a mixture of normal (alpha MEM) cell culture medium supplemented as before but with the addition of ascorbic acid and glycerol 2-phosphate.^[313] In this way, osteogenic activity was promoted, and osteoblasts would proliferate, mature and mineralize the substrate at a higher rate. To summarize, 8 simultaneous experiments were conducted, for control and uniform gradient, at 15 or 30 days of culture, with normal and osteogenic medium (Table 3).

Table 3: XRF experiments on 1% GG fibers loaded with MC3T3 osteoblasts.

Count	1	2	3	4	5	6	7	8
Medium	Normal	Osteogenic	Normal	Osteogenic	Normal	Osteogenic	Normal	Osteogenic
Time (days)	15	15	30	30	15	15	30	30
Sample	Control	Control	Control	Control	Gradient	Gradient	Gradient	Gradient

The samples were initially seeded with osteoblasts (MC3T3) and then placed on 6-well petri dishes which were carefully filled with 3-4 mL of the appropriate cell culture medium (normal or osteogenic) before placing them for 15 or 30 days of incubation. Once the materials were ready for the XRF study, they were thoroughly washed several times with PBS and deionized water to remove any medium content as it contains traces of phosphorus and other minerals which could influence the final results. The washing stage was also performed in a careful manner so as to avoid washing away cells or minerals deposited on the surface of the substrate. The XRF was previously calibrated to detect and filter calcium and phosphorus elements found on the substrate. The X-ray tube and generator were set to 50 kV and 400 mA

respectively, the pixel time was set to 10 ms and 5 cycles of imaging were performed to obtain good resolution images.

A. 15 days of culture

The images obtained from the first 4 sets on the 15 days of incubation are displayed on Figure 55.

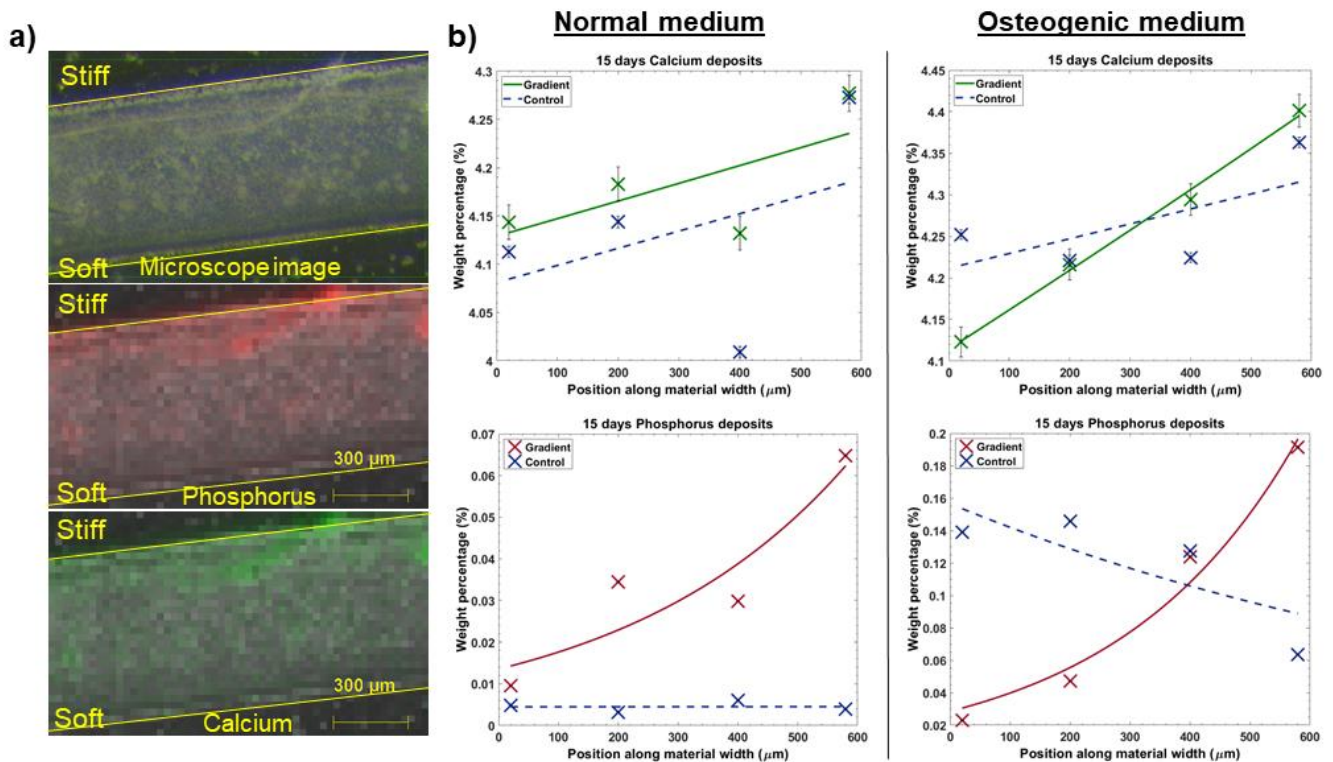


Figure 55: a) Microscope image as well as calcium and phosphorus XRF pictures of stiffness gradient gellan gum fibers loaded with MC3T3 cells across their surface, b) Calcium and phosphorus deposits after 15 days of culture in normal and osteogenic medium. Yellow lines highlight the boundaries of the uniform GG fibers. Each point is the average of 3 areas located at the same width position for 3 different samples exhibiting similar stiffness gradient.

As seen little to no progress was made on the regular cell culture medium as cells were found on their maturation stage where they still express alkaline phosphatase activity,^[315] whereas on the osteogenic medium where mineralization was promoted, we can observe a clear augmentation on both Ca and P deposits values compared to the normal one. Moreover, we cannot distinguish a clear difference on calcium deposits between the control and the gradient samples for the 15 days normal medium, due to the fact that osteoblasts are still on their maturation phase, a fact that can be presumed by looking at the corresponding phosphorus deposits plot where a gradient of P mineral is apparent. The use of osteogenic medium has proven to be a good decision as we can clearly see from the plots that we obtained clear differences between the 2 samples and a gradient trend is noticeable on both Ca and P deposits. This first set of experiments was quite promising and encouraging towards obtaining quantitative data in relation to the mineralization and maturation stage of osteoblasts and how that was regulated by the gradient GG fibers.

The images were quantified using the XRF Bruker Tornado software which processed the set of peaks obtained using a standard spectrum elements quantification method. Each peak detected corresponds to a certain element and the intensity of the peak is depicted as light intensity on the pictures (Figure 56). The X-axis represents the element-specific fluorescent energies while Y-axis is an arbitrary unit of counts per second per eV which represents the detected events registered every second per electron-volt. Each element of the periodic table, emits a specific energy which is detected by the equipment and subsequently each peak is associated to the corresponding element.^[236] The higher the peak the more fluorescent energy is emitted from that element which can be converted to a mass percentage and overall we obtain the complete picture of the elemental analysis for each specimen. For that reason, no image processing software was used, as these intensities are relative depending on the sample maximum and minimum values. Instead we have used the raw data obtained from the

equipment which converted the counts per eV into weight percentage with a standard error given.

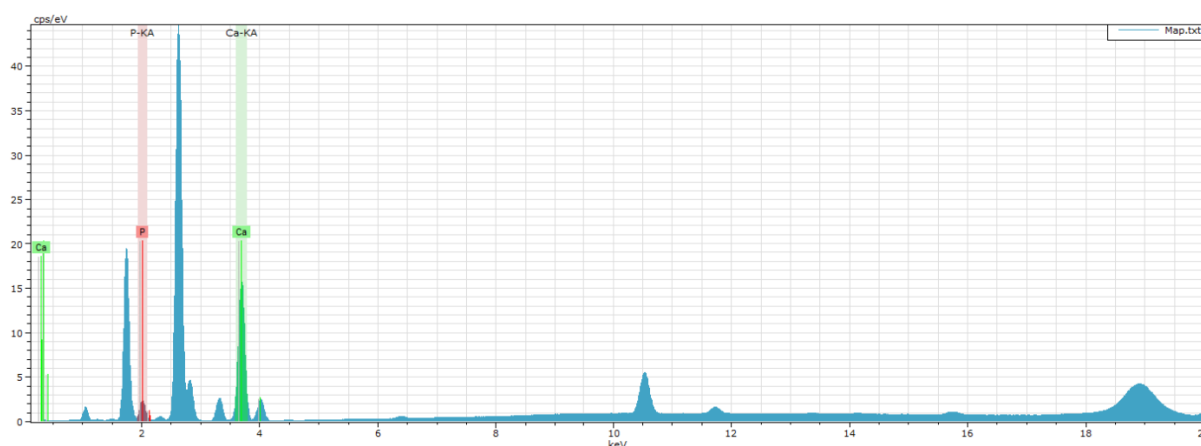


Figure 56: Example of the spectrum of elements obtained upon the X-Ray scanning of the sample.

Similar to the AFM data processing method, each picture was splitted into 4 different areas to measure locally the average weight percentage of each mineral. These areas contained the same number of pixels, with each pixel corresponding to a certain value for both Ca and P elements (Figure 57). In addition, each pixel represents an area of $27 \times 27 \mu\text{m}$ with a total of 16 pixels comprising each area ($11,664 \mu\text{m}^2$ in total). In this way, the weight percentage of each mineral was calculated locally across the 1% GG gradient fibers, which gave us an overview of the distribution of Ca and P across the width of the material. Furthermore, we took into account the fact that the matrix contains calcium ions that were previously used for the cross-linking of gellan gum. For that reason, a plain gradient material of similar stiffness range was XRF imaged to create a calcium mineral distribution across the width of the fiber, in order to be used as a baseline and be subtracted from the cell loaded materials. In this way, the results were uninfluenced by the calcium content of the material and only the cell deposits were considered.

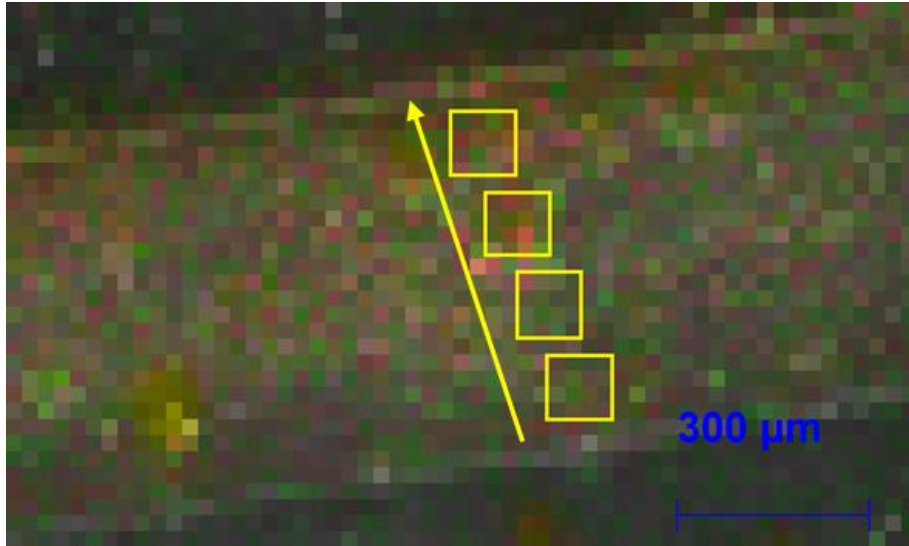


Figure 57: Schematic of the different areas measured across the MC3T3 cell loaded and gradient GG fibers used for the quantification of each element across the width of the material from the XRF images. Averages of each area were later plotted in a similar way as the AFM plots.

B. 30 days of culture

Following the 15 days experiments, the batch of 30 days was XRF imaged and processed using the method mentioned above for consistency purposes. It was expected from this set of experiments to obtain much clearer data regarding the gradient of minerals across the width of the GG fibers for both normal and osteogenic medium. The results are presented below in Figure 58.

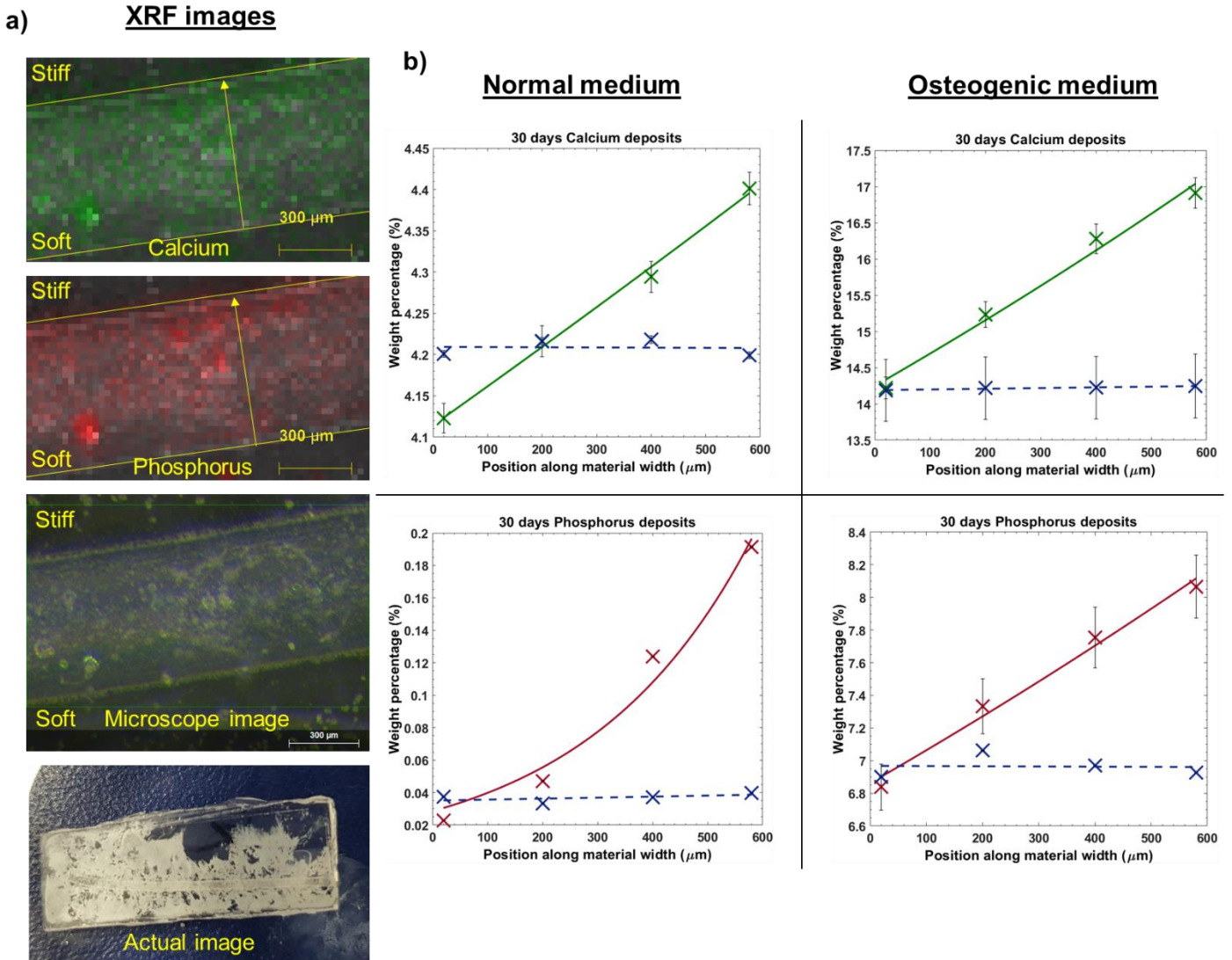


Figure 58: a) Microscope, actual, calcium and phosphorus XRF pictures of 1% stiffness gradient gellan gum fibers loaded with MC3T3 cells across their surface, b) Calcium and phosphorus deposits after 30 days of culture in both normal and osteogenic medium. Yellow lines highlight the boundaries of the uniform GG fibers. Each point is the average of 3 areas located at the same width position for 3 different samples exhibiting similar stiffness gradient.

As expected, based on the preliminary (15 days) results (presented at fig. 60), both minerals showed a gradient deposition which corresponded to the stiffness gradient of the material and indicated the promotion of bone formation towards the stiffer side of the biomaterial. These 30 days XRF results are much clearer and give us a better picture of osteoblast activity compared to the 15 days ones, which was anticipated as cells had more time

to differentiate and mineralize the substrate. In addition, from both the microscope and the actual image we can see that the material was fully covered with osteoblasts in their early stage of bone tissue formation. The surface of the material and a part of the supportive glass slide were covered with a thick layer of fully grown cells that were depositing minerals as seen on the actual image. Though, the cells did not mineralize the substrate at the same rate, with the layer of osteoblasts being at the softer part of the matrix to have a lower deposition rate according to the plots. This crucially highlighted the biological process of bone tissue formation in the osteotendinous interface where osteoblasts are guided by the ECM properties to gradually mineralize the substrate. We can therefore conclude that, by carefully engineering the profile of the stiffness gradient it is thus possible to guide cell functionality and promote bone formation towards the specified areas of interest.

Conclusions

One of today's main challenges is to mimic the tissue microenvironment accurately and regulate cell activity on the matrix especially on the micro-scale. As seen from the literature, extensive progress has been made on the identification of cell types and their activity but also several 3-D scaffolds or substrates have been developed with the vast majority exhibiting good biocompatibility and some of them are being used as implants for repairing damaged tissues. However, most of the studies demonstrated the cell-matrix interactions but lack the cell-cell interactions when the cells are being found on different conditions in the same matrix.

To address these issues, we developed a novel microfluidic technique to fabricate biomaterials that exhibit a gradient of mechanical properties for accurately mimicking the tissue microenvironment and regulating cell behaviour. The technique is based on the application of temperature gradients in microfluidic devices and the subsequent exploitation of the phenomenon of thermophoresis to carefully fine-tune and effectively control the material's mechanical properties such as stiffness and porosity. The ease of operation and the low cost as disposable microfluidic chips that are being used are some of the advantages that this method has to offer. In addition, the technique was applied to two types of biomaterials, sodium alginate and gellan gum, thus demonstrating the capability of controlling the mechanical properties of the hydrogels independently from the polymerization process. It can therefore be employed into different types of biomaterials depending on the application for addressing several tissue engineering problems. Furthermore, the technique is considered to be cell friendly as it lacks the use of methods such as UV treatment, photoinitiators or other toxic residues that could prove harmful for cell cultures in the long run.

The mechanism behind this microfluidic technique is based on imposing and controlling temperature gradients on hydrogels at the liquid state which triggers the phenomenon on thermophoresis. Subsequently, the hydrogel's monomers are experiencing the thermophoretic force which induces a concentration gradient to the solution that is later "translated" into a gradient of mechanical properties, upon the gelation stage. In steady state the liquid phase of the hydrogel exhibits a concentration gradient and once the material is rapidly cross-linked, it is maintained and transformed onto a stiffness and porosity gradient across the material's width.

Primarily, the existence of the stiffness gradient on the ECM was probed using atomic force microscopy. Indentation tests locally across the 600 μm width fibers, using an 8 μm borosilicate spherical tip have revealed the magnitude of the stiffness gradient which typically ranges from 20 to 80 kPa depending on several factors. Later, we investigated in depth all the factors that could potentially influence the gradient to demonstrate an effective control over the biomaterial's properties and the ability to select the desired range of Young's modulus values across the substrate. At first by altering the concentration of the hydrogel we were able to shift the entire gradient upwards or downwards in terms of YM values so that it can be applied for different types of cells. Also, the steepness of the gradient was controlled by changing the magnitude of the applied temperature gradient, with an increased ∇T yielding a more profound exponential gradient compared to the less steep and linear one generated by a lower ∇T . In addition, the residence time of the material in the main microchannel seemed to have an impact on the stiffness gradient as well. A greater residence time produced slightly steeper stiffness gradients with higher YM values on both ends (stiffer and softer) compared to a lower time. By controlling all three major parameters we were able to fabricate biomaterials that exhibited stiffness gradients with the desired YM values across their surface.

Moreover, we demonstrated the ability to further expand the stiffness range and manipulate the materials mechanical properties in 2 axes. Upon the generation of a biomaterial with a certain stiffness gradient across its width we were able to partially de-swell and dehydrate the fiber across its length to generate a secondary gradient along that direction. In this way, the structure of the material was shrunk to some extent due to the removal of water molecules that held together the firm polymeric network previously created, generating a stiffer substrate due to the packing GG coils in a more confined structure. One side of the material was less hydrated than the other one with a gradual increase between them, resulting at a stiffness gradient along that axis.

Furthermore, we demonstrated the excellent biocompatibility of the biomaterials by conducting a live/dead assay on seeded osteoblasts (cell line MC3T3) at the surface of the fibers, which yielded an 83-85% of cell viability across the substrate. We also carried out migration and proliferation studies throughout the material's surface for up to 7 days by staining the cells with a membrane fluorescent ink and capturing pictures daily to observe the position and the population of osteoblasts. The latter combined with the previous study have revealed the differences in cell activity between the high and low stiffness areas on the fibers. Migration was observed towards the stiffer area of the fiber with cells remaining idle and round on the softer part. We were also able to identify cell density and spreading by processing the fluorescent images with ImageJ software. We noticed that the elongation of the osteoblasts on the stiffer substrate was significantly better up to 50% more than the ones at the softer one and that cell population is denser on higher YM values. These results have shown us that MC3T3s prefer the stiffer substrate for settling and proliferating as it offers a firm substrate with multiple binding spots for focal adhesions to develop.

Additionally, the effect of the material's gradient of mechanical properties on the bio-functionality of osteoblasts was investigated by conducting an XRF imaging on the substrate.

Upon the deposition of MC3T3s on the biomaterial we allowed cells to proliferate and undergo a maturation stage for 15 and 30 days both in normal and osteogenic medium. Cells were expected to express ALP during their maturation followed by the mineralization of the substrate where calcium was deposited. The XRF images clearly demonstrate a gradient of cell maturation and mineralization which follows the gradient of mechanical properties (stiffness and porosity) that was previously generated by the microfluidic technique. Increased, phosphorus deposits on the stiffer side indicated an improved ALP expression from the osteoblasts which meant that cells matured much faster than the ones at the softer side. Also, the gradient of calcium deposits which goes along the stiffness and porosity gradient confirms the improved biofunctionality of the MC3T3s as we move from the soft to the stiff side of the fibers. Therefore, we were able to control cell activity and regulate the biofunctionality of osteoblasts by creating a gradient of mechanical properties on biomaterials exploiting the phenomenon of thermophoresis.

All the above, nominate this novel microfluidic technique as a powerful tool that can be used to mimic the tissue microenvironment and induce improved cell activity towards specified areas of interest. The manipulation of cell behavior stems from the gradient of mechanical properties which was generated by imposing temperature gradients on biomaterials inside a microfluidic setup and triggering the phenomenon of thermophoresis. The application of thermophoretic force on the molecules of the selected biomaterial forms a concentration gradient which is later transformed into a gradient of mechanical properties that is used to influence cell behavior.

Herein, we demonstrate the mimicking of bone tissue microenvironment and the effective manipulation of both substrate and cell activity through a simple and non-toxic microfluidic technique. This technique can potentially be extrapolated in the future to generate gradients locally across the substrate to create patterns where cell activity is promoted.

Future work

Firstly, it is possible to further explore the capabilities of the two-dimensional stiffness gradient material that was reported in the “exploring a new type of gradient” section of the results chapter. This type of material could be “stretched” to achieve a wide range of stiffness across its surface from low Young’s modulus values around 10 kPa up to higher ones around 300 kPa. In this way, we can potentially investigate multiple cell types that situate within the broader range of the material and observe how stiffness influences their behavior, namely differentiation, migration, proliferation, and functionality.

Secondly, a different type of cells could be potentially seeded and studied on the surface of the fibers, such as mesenchymal stem cells (MSCs).^[32] MSCs would probably differentiate into different cell types according to the substrate stiffness they are situated.^[58, 59] Bone and cartilage cells in the osteochondral tissue are differentiated MSC precursors, though the transitional interface between those two cell types is hard to be replicated.^[316] Using the stiffness gradient fibers it would be possible to differentiate MSCs into these two different cell types (osteoblasts and chondrocytes) based on the substrate stiffness, softer for cartilage tissue and stiffer for bone one.^[58, 316] The potential of such a scaffold could then further expand into implants for repairing damaged cartilage or into a platform to study the cellular interactions at the osteochondral interface in the microscale.^[316] In a similar way, we could theoretically also investigate the osteotendinous interface and the interactions between tendon and bone cells at the micro-scale which remains one of the major challenges in tissue engineering.^[317] In addition, the MSCs could be deposited onto the two-dimensional stiffness gradient scaffold mentioned above which would allow us to study their differentiation into a wider stiffness and porosity range with a less steep gradient between the different areas.

Moreover, different types of materials could be employed as the manipulation technique is independent of the polymerization/cross-linking stage of the material, as demonstrated on the “biomaterial fabrication process” section of the results chapter where both NaAlg and GG fibers were fabricated. The purpose of using a different material type is to explore different tissues that might require certain substrate characteristics and properties. For example, collagen scaffolds are employed in skin tissue engineering as 70% to 80% of the dermis dry weight is consisted of collagen type I.^[318] These types of scaffolds exhibit great biocompatibility, promote cell proliferation and infiltration of fibroblasts from surrounding tissues.^[319] They are suitable candidates for the development of patches applied for dermal repair and the addition of a gradient of mechanical properties could prove useful especially at interface tissue engineering problems.^[320]

Furthermore, by using other types of materials we can potentially embed the cells inside the material’s structure in order to establish a novel 3-D scaffold that can manipulate cell behaviour in all 3 axes (x,y,z). Using gellan gum we were unable to achieve that due to the high temperatures that were required in order to keep the material at a liquid state. Biomaterials such as collagen or Poly-lactic-co-glycolic acid (PLGA) could potentially serve as the building blocks for composite 3-D scaffolds or implants loaded with stem cells that would later differentiate according to the ECM characteristics.^[313, 321-324] For example a study by Dai et al. demonstrated the design of a collagen type I based scaffold, loaded with MSCs across its network for restoring infarcted myocardium and reducing the relocation of transplanted cells to non-infarcted tissue and other remote organs.^[325]

Another potential application of the method, it could be extrapolated into a different system involving infrared laser technology, to generate patterns of local gradients which might direct cells to specific areas of interest. Specifically, by aligning an infrared laser with the main microchannel of the microfluidic device and using of a photomask we could illuminate locally

in a specific pattern the liquid hydrogel to create local temperature gradients that would trigger the phenomenon of thermophoresis and induce local concentration gradients. Following, a similar procedure established in this project local stiffness and porosity gradients can be generated across various types of biomaterials that would drive cells towards the patterned areas. Such a scaffold could have the ability to repair on demand, certain regions of the damaged tissue or organ, by retaining the transplanted cells of the infarcted areas which remains to this day a great limitation in wound healing and organ repair applications.^[325]

Finally, the findings of the present study establish the foundations for the further development of this novel microfluidic technique and provide us with insights that could potentially be applied in the design of future 3-D scaffolds, with the aim of addressing challenging tissue engineering problems.

References

- [1] B. Chevallay, D. Herbage, *Med Biol Eng Comput* **2000**, *38*, 211.
- [2] T. J. Keane, S. F. Badylak, *Semin Pediatr Surg* **2014**, *23*, 112.
- [3] L. Sandell, D. Sakai, *Current Protocols Essential Laboratory Techniques* **2011**, *5*, 4.3.1.
- [4] S. Ansari, S. Khorshidi, A. Karkhaneh, *Acta Biomater* **2019**, *87*, 41.
- [5] G. M. Whitesides, *Nature* **2006**, *442*, 368.
- [6] E. K. Sackmann, A. L. Fulton, D. J. Beebe, *Nature* **2014**, *507*, 181.
- [7] J. A. Burdick, A. Khademhosseini, R. Langer, *Langmuir* **2004**, *20*, 5153.
- [8] A. Folch, A. Ayon, O. Hurtado, M. A. Schmidt, M. Toner, *J Biomech Eng-T Asme* **1999**, *121*, 28.
- [9] D. E. Discher, P. Janmey, Y. L. Wang, *Science* **2005**, *310*, 1139.
- [10] I. Hopp, A. Michelmore, L. E. Smith, D. E. Robinson, A. Bachhuka, A. Mierczynska, K. Vasilev, *Biomaterials* **2013**, *34*, 5070.
- [11] R. Sunyer, A. J. Jin, R. Nossal, D. L. Sackett, *Plos One* **2012**, *7*.
- [12] R. Langer, J. Vacanti, *Science* **1993**, *260*, 920.
- [13] C. Frantz, K. M. Stewart, V. M. Weaver, *Journal of Cell Science* **2010**, *123*, 4195.
- [14] R. L. Juliano, S. Haskill, *J Cell Biol* **1993**, *120*, 577.
- [15] V. P. Ivanova, A. I. Krivchenko, *J Evol Biochem Phys+* **2012**, *48*, 375.
- [16] F. M. Watt, W. T. S. Huck, *Nat Rev Mol Cell Bio* **2013**, *14*, 467.
- [17] F. M. Watt, H. Fujiwara, *Csh Perspect Biol* **2011**, *3*.
- [18] F. Gattazzo, A. Urciuolo, P. Bonaldo, *Bba-Gen Subjects* **2014**, *1840*, 2506.
- [19] L. G. Griffith, G. Naughton, *Science* **2002**, *295*, 1009.
- [20] L. G. Griffith, *Acta Mater* **2000**, *48*, 263.
- [21] L. Meinel, R. Fajardo, S. Hofmann, R. Langer, J. Chen, B. Snyder, G. Vunjak-Novakovic, D. Kaplan, *Bone* **2005**, *37*, 688.
- [22] M. J. Lysaght, J. Reyes, *Tissue Eng* **2001**, *7*, 485.
- [23] N. Landa, L. Miller, M. S. Feinberg, R. Holbova, M. Shachar, I. Freeman, S. Cohen, J. Leor, *Circulation* **2008**, *117*, 1388.
- [24] S. F. Badylak, R. M. Nerem, *P Natl Acad Sci USA* **2010**, *107*, 3285.
- [25] D. W. Huttmacher, *Biomaterials* **2000**, *21*, 2529.
- [26] P. Bruin, J. Smedinga, A. J. Pennings, M. F. Jonkman, *Biomaterials* **1990**, *11*, 291.
- [27] R. Langer, J. P. Vacanti, *Sci Am* **1995**, *273*, 130.
- [28] T. Subbiah, G. S. Bhat, R. W. Tock, S. Parameswaran, S. S. Ramkumar, *Journal of Applied Polymer Science* **2005**, *96*, 557.
- [29] J. N. Mansbridge, *Curr Opin Biotech* **2009**, *20*, 563.
- [30] C. J. Flaim, S. Chien, S. N. Bhatia, *Nat Methods* **2005**, *2*, 119.
- [31] T. Reya, S. J. Morrison, M. F. Clarke, I. L. Weissman, *Nature* **2001**, *414*, 105.
- [32] A. I. Caplan, *Journal of orthopaedic research* **1991**, *9*, 641.
- [33] G. M. Keller, *Current opinion in cell biology* **1995**, *7*, 862.
- [34] K. Le Blanc, *Cytotherapy* **2006**, *8*, 559.
- [35] W. Zakrzewski, M. Dobrzyński, M. Szymonowicz, Z. Rybak, *Stem Cell Res Ther* **2019**, *10*, 68.
- [36] P. Bianco, M. Riminucci, S. Gronthos, P. G. Robey, *STEM CELLS* **2001**, *19*, 180.

- [37] M. A. C. Stuart, W. T. S. Huck, J. Genzer, M. Muller, C. Ober, M. Stamm, G. B. Sukhorukov, I. Szleifer, V. V. Tsukruk, M. Urban, F. Winnik, S. Zauscher, I. Luzinov, S. Minko, *Nat Mater* **2010**, *9*, 101.
- [38] J. M. Anderson, A. Rodriguez, D. T. Chang, *Semin Immunol* **2008**, *20*, 86.
- [39] D. B. Kolesky, R. L. Truby, A. S. Gladman, T. A. Busbee, K. A. Homan, J. A. Lewis, *Adv Mater* **2014**, *26*, 3124.
- [40] A. Bartholomew, C. Sturgeon, M. Siatskas, K. Ferrer, K. McIntosh, S. Patil, W. Hardy, S. Devine, D. Ucker, R. Deans, A. Moseley, R. Hoffman, *Exp Hematol* **2002**, *30*, 42.
- [41] H. C. Ott, T. S. Matthiesen, S. K. Goh, L. D. Black, S. M. Kren, T. I. Netoff, D. A. Taylor, *Nat Med* **2008**, *14*, 213.
- [42] S. V. Murphy, A. Atala, *Nat Biotechnol* **2014**, *32*, 773.
- [43] A. K. Gupta, M. Gupta, *Biomaterials* **2005**, *26*, 3995.
- [44] R. A. Pagliarini, T. Xu, *Science* **2003**, *302*, 1227.
- [45] Y. A. Jodat, M. G. Kang, K. Kiaee, G. J. Kim, A. F. H. Martinez, A. Rosenkranz, H. Bae, S. R. Shin, *Curr Pharm Des* **2018**, *24*, 5471.
- [46] F. M. Chen, M. Zhang, Z. F. Wu, *Biomaterials* **2010**, *31*, 6279.
- [47] F. Rosso, A. Giordano, M. Barbarisi, A. Barbarisi, *J Cell Physiol* **2004**, *199*, 174.
- [48] L. Wang, Y. H. Li, G. Y. Huang, X. H. Zhang, B. Pingguan-Murphy, B. Gao, T. J. Lu, F. Xu, *Crit Rev Biotechnol* **2016**, *36*, 553.
- [49] V. E. Santo, P. Babo, M. Amador, C. Correia, B. Cunha, D. F. Coutinho, N. M. Neves, J. F. Mano, R. L. Reis, M. E. Gomes, *Biomacromolecules* **2016**, *17*, 1985.
- [50] S. Sart, S. N. Agathos, *Mol Biotechnol* **2018**, *60*, 843.
- [51] J. Y. Wong, A. Velasco, P. Rajagopalan, Q. Pham, *Langmuir* **2003**, *19*, 1908.
- [52] R. G. Wells, *Hepatology* **2008**, *47*, 1394.
- [53] R. J. Pelham, Y. L. Wang, *P Natl Acad Sci USA* **1997**, *94*, 13661.
- [54] P. Moreo, J. M. Garcia-Aznar, M. Doblare, *Acta Biomater* **2008**, *4*, 613.
- [55] C. Gaudet, W. A. Marganski, S. Kim, C. T. Brown, V. Gunderia, M. Dembo, J. Y. Wong, *Biophys J* **2003**, *85*, 3329.
- [56] A. J. Engler, S. Sen, H. L. Sweeney, D. E. Discher, *Cell* **2006**, *126*, 677.
- [57] D. Brindley, K. Moorthy, J. H. Lee, C. Mason, H. W. Kim, I. Wall, *J Tissue Eng* **2011**, *2011*, 620247.
- [58] T. Assis-Ribas, M. F. Forni, S. M. B. Winnischofer, M. C. Sogayar, M. Trombetta-Lima, *Developmental Biology* **2018**, *437*, 63.
- [59] S. G. Almalki, D. K. Agrawal, *Differentiation* **2016**, *92*, 41.
- [60] A. Buxboim, K. Rajagopal, A. E. X. Brown, D. E. Discher, *J Phys-Condens Mat* **2010**, *22*.
- [61] C. Franck, S. A. Maskarinec, D. A. Tirrell, G. Ravichandran, *Plos One* **2011**, *6*.
- [62] M. Bahram, N. Mohseni, M. Moghtader, in *Emerging concepts in analysis and applications of hydrogels*, IntechOpen, **2016**.
- [63] M. S. Jhon, J. D. Andrade, *J Biomed Mater Res* **1973**, *7*, 509.
- [64] J. D. Ferry, *Viscoelastic properties of polymers*, John Wiley & Sons, **1980**.
- [65] O. Wichterle, D. Lim, *Nature* **1960**, *185*, 117.
- [66] E. M. Ahmed, *Journal of Advanced Research* **2015**, *6*, 105.
- [67] B. Jeong, S. W. Kim, Y. H. Bae, *Adv Drug Deliver Rev* **2002**, *54*, 37.
- [68] A. M. Rosales, K. S. Anseth, *Nature Reviews Materials* **2016**, *1*, 15012.
- [69] G. Leone, R. Barbucci, in *Hydrogels: Biological Properties and Applications*, Springer Milan, Milano **2009**, 25.
- [70] S. Van Vlierberghe, P. Dubruel, E. Schacht, *Biomacromolecules* **2011**, *12*, 1387.
- [71] G. S. Hussey, J. L. Dziki, S. F. Badylak, *Nature Reviews Materials* **2018**, *3*, 159.

- [72] A. S. Hoffman, *Adv Drug Deliver Rev* **2012**, *64*, 18.
- [73] Q. Chai, Y. Jiao, X. Yu, *Gels* **2017**, *3*.
- [74] R. Stadler, *Macromolecules* **1988**, *21*, 121.
- [75] R. Stadler, L. D. Freitas, *Colloid Polym Sci* **1986**, *264*, 773.
- [76] O. Smidsrød, H. Grasdalen, *Carbohydr Polym* **1982**, *2*, 270.
- [77] L. Z. Rogovina, *Slonimsk.Gl, Usp Khim+* **1974**, *43*, 1102.
- [78] L. Z. Rogovina, V. G. Vasil'ev, E. E. Braudo, *Polym Sci Ser C+* **2008**, *50*, 85.
- [79] S. Papkov, Moscow: Khimiya **1971**.
- [80] L. Rogovina, O. Tchegolihina, V. Vasiliev, V. Y. Levin, A. Zhdanov, "The reversible network formation in polydimethyl-siloxanes with side carboxyl groups", presented at *Makromolekulare Chemie. Macromolecular Symposia*, **1991**.
- [81] O. I. Shchegolikhina, V. G. Vasilev, L. Z. Rogovina, V. Y. Levin, A. A. Zhdanov, G. L. Slonimskii, *Vysokomol Soedin a+* **1991**, *33*, 2370.
- [82] Z. Q. Liu, M. A. Meyers, Z. F. Zhang, R. O. Ritchie, *Prog Mater Sci* **2017**, *88*, 467.
- [83] C. Li, L. Ouyang, I. J. Pence, A. C. Moore, Y. Lin, C. W. Winter, J. P. K. Armstrong, M. M. Stevens, *Adv Mater* **2019**, *31*, 1900291.
- [84] J. Aizenberg, A. J. Black, G. M. Whitesides, *Nature* **1999**, *398*, 495.
- [85] L. V. Dekker, A. W. Segal, *Science* **2000**, *287*, 982.
- [86] C. A. Parent, P. N. Devreotes, *Science* **1999**, *284*, 765.
- [87] O. D. Weiner, G. Servant, M. D. Welch, T. J. Mitchison, J. W. Sedat, H. R. Bourne, *Nat Cell Biol* **1999**, *1*, 75.
- [88] P. C. Wilkinson, *J Immunol Methods* **1998**, *216*, 139.
- [89] D. A. Lauffenburger, A. F. Horwitz, *Cell* **1996**, *84*, 359.
- [90] L. M. Machesky, *Febs Lett* **2008**, *582*, 2102.
- [91] M. A. Wozniak, K. Modzelewska, L. Kwong, P. J. Keely, *Bba-Mol Cell Res* **2004**, *1692*, 103.
- [92] C. T. Mierke, D. Rosel, B. Fabry, J. Brabek, *Eur J Cell Biol* **2008**, *87*, 669.
- [93] T. M. Skerry, L. Bitensky, J. Chayen, L. E. Lanyon, *J Bone Miner Res* **1989**, *4*, 783.
- [94] Helmut Fischer GmbH, "X-Ray Fluorescence Spectroscopy (XRF) – Basics", can be found under <https://xrf-spectroscopy.com/>, **2018**.
- [95] S. Lehoux, A. Tedgui, *Hypertension* **1998**, *32*, 338.
- [96] I. A. Janson, A. J. Putnam, *Journal of biomedical materials research. Part A* **2015**, *103*, 1246.
- [97] C. M. Lo, H. B. Wang, M. Dembo, Y. L. Wang, *Biophys J* **2000**, *79*, 144.
- [98] H. Ebata, K. Moriyama, T. Kuboki, S. Kidoaki, *Biomaterials* **2020**, *230*, 119647.
- [99] C. Cha, W. B. Liechty, A. Khademhosseini, N. A. Peppas, *Acs Nano* **2012**, *6*, 9353.
- [100] Kshitiz, J. Park, P. Kim, W. Helen, A. J. Engler, A. Levchenko, D.-H. Kim, *Integrative Biology* **2012**, *4*, 1008.
- [101] C. H. R. Kuo, J. Xian, J. D. Brenton, K. Franze, E. Sivaniah, *Adv Mater* **2012**, *24*, 6059.
- [102] X. R. Li, J. W. Xie, J. Lipner, X. Y. Yuan, S. Thomopoulos, Y. N. Xia, *Nano Lett* **2009**, *9*, 2763.
- [103] W. E. Teo, S. Ramakrishna, *Nanotechnology* **2006**, *17*, R89.
- [104] H. R. Park, M. S. Kim, S. J. Kim, M. Park, K. H. Kong, H. S. Kim, S. J. Kwack, T. S. Kang, S. H. Kim, H. S. Kim, J. Lee, *Toxicol Lett* **2010**, *193*, 86.
- [105] C. G. Williams, A. N. Malik, T. K. Kim, P. N. Manson, J. H. Elisseeff, *Biomaterials* **2005**, *26*, 1211.
- [106] S. J. Bryant, K. S. Anseth, *J Biomed Mater Res* **2002**, *59*, 63.
- [107] G. Eng, B. W. Lee, H. Parsa, C. D. Chin, J. Schneider, G. Linkov, S. K. Sia, G. Vunjak-Novakovic, *P Natl Acad Sci USA* **2013**, *110*, 4551.

- [108] R. K. Willits, S. L. Skornia, *J Biomat Sci-Polym E* **2004**, *15*, 1521.
- [109] R. Wieduwild, M. Howarth, *Biomaterials* **2018**, *180*, 253.
- [110] A. Schneider, G. Francius, R. Obeid, P. Schwinte, J. Hemmerle, B. Frisch, P. Schaaf, J. C. Voegel, B. Senger, C. Picart, *Langmuir* **2006**, *22*, 1193.
- [111] P. E. Jansson, B. Lindberg, P. A. Sandford, *Carbohyd Res* **1983**, *124*, 135.
- [112] X. H. Shi, J. N. BeMiller, *Carbohyd Polym* **2002**, *50*, 7.
- [113] P. B. Deasy, K. J. Quigley, *Int J Pharm* **1991**, *73*, 117.
- [114] A. M. Smith, R. M. Shelton, Y. Perrie, J. J. Harris, *J Biomater Appl* **2007**, *22*, 241.
- [115] I. Giavasis, L. M. Harvey, B. McNeil, *Crit Rev Biotechnol* **2000**, *20*, 177.
- [116] G. Sworn, in *Handbook of Hydrocolloids (Second Edition)*, (Eds: G. O. Phillips, P. A. Williams), Woodhead Publishing, **2009**, 204.
- [117] H. Grasdalen, O. Smidsrod, *Carbohyd Polym* **1987**, *7*, 371.
- [118] L. R. Stevens, K. J. Gilmore, G. G. Wallace, M. I. H. Panhuis, *Biomater Sci-Uk* **2016**, *4*, 1276.
- [119] H. Y. Jeon, E. Y. Shin, J. H. Choi, J. E. Song, R. L. Reis, G. Khang, *Macromol Res* **2018**, *26*, 724.
- [120] S. Vieira, A. da Silva Morais, E. Garet, J. Silva-Correia, R. L. Reis, Á. González-Fernández, J. Miguel Oliveira, *Acta Biomater* **2019**.
- [121] H. H. Tonnesen, J. Karlsen, *Drug Dev Ind Pharm* **2002**, *28*, 621.
- [122] B. D. Kevadiya, G. V. Joshi, H. A. Patel, P. G. Ingole, H. M. Mody, H. C. Bajaj, *J Biomater Appl* **2010**, *25*, 161.
- [123] M. Chaplin, "Water structure and science: Alginate", can be found under <http://www1.lsbu.ac.uk/water/alginate.html>, **2018**.
- [124] M. D. Guiry, "The Seaweed Site: information on marine algae: Alginates", can be found under http://www.seaweed.ie/uses_general/alginate.php, **2000**.
- [125] T. M. Valentin, S. E. Leggett, P. Y. Chen, J. K. Sodhi, L. H. Stephens, H. D. McClintock, J. Y. Sim, I. Y. Wong, *Lab Chip* **2017**, *17*, 3474.
- [126] S. J. Florczyk, M. Leung, S. Jana, Z. S. Li, N. Bhattarai, J. I. Huang, R. A. Hopper, M. Q. Zhang, *J Biomed Mater Res A* **2012**, *100a*, 3408.
- [127] M. Y. Liu, Z. Z. Zhou, Y. C. Chai, S. Zhang, X. M. Wu, S. P. Huang, J. Q. Su, J. H. Jiang, *Biofabrication* **2017**, *9*.
- [128] J. Genzer, R. R. Bhat, *Langmuir* **2008**, *24*, 2294.
- [129] T. M. Keenan, A. Folch, *Lab Chip* **2008**, *8*, 34.
- [130] S. Nemir, H. N. Hayenga, J. L. West, *Biotechnol Bioeng* **2010**, *105*, 636.
- [131] N. A. Peppas, Y. Huang, M. Torres-Lugo, J. H. Ward, J. Zhang, *Annu Rev Biomed Eng* **2000**, *2*, 9.
- [132] J. C. Meredith, *Journal of Materials Chemistry* **2009**, *19*, 34.
- [133] A. L. Hook, D. G. Anderson, R. Langer, P. Williams, M. C. Davies, M. R. Alexander, *Biomaterials* **2010**, *31*, 187.
- [134] Y. Yang, D. Bolikal, M. L. Becker, J. Kohn, D. N. Zeiger, C. G. Simon Jr, *Adv Mater* **2008**, *20*, 2037.
- [135] N. W. Choi, M. Cabodi, B. Held, J. P. Gleghorn, L. J. Bonassar, A. D. Stroock, *Nat Mater* **2007**, *6*, 908.
- [136] J. W. Hong, S. R. Quake, *Nat Biotechnol* **2003**, *21*, 1179.
- [137] N. T. Nguyen, Z. G. Wu, *J Micromech Microeng* **2005**, *15*, R1.
- [138] T. J. Johnson, D. Ross, L. E. Locascio, *Analytical chemistry* **2002**, *74*, 45.
- [139] L.-H. Lu, K. S. Ryu, C. Liu, "A novel microstirrer and arrays for microfluidic mixing", presented at *Micro Total Analysis Systems 2001*, **2001**.
- [140] X. Wang, C. Cheng, S. Wang, S. Liu, *Microfluidics and Nanofluidics* **2009**, *6*, 145.

- [141] H. Mao, T. Yang, P. S. Cremer, *J Am Chem Soc* **2002**, *124*, 4432.
- [142] K. Ward, Z. H. Fan, *J Micromech Microeng* **2015**, *25*.
- [143] T. Frommelt, M. Kostur, M. Wenzel-Schäfer, P. Talkner, P. Hänggi, A. Wixforth, *Phys Rev Lett* **2008**, *100*, 034502.
- [144] D. T. Chiu, N. L. Jeon, S. Huang, R. S. Kane, C. J. Wargo, I. S. Choi, D. E. Ingber, G. M. Whitesides, *P Natl Acad Sci USA* **2000**, *97*, 2408.
- [145] J. He, Y. Du, Y. Guo, M. J. Hancock, B. Wang, H. Shin, J. Wu, D. Li, A. Khademhosseini, *Biotechnol Bioeng* **2011**, *108*, 175.
- [146] B. Deng, J. de Ruiter, K. Schroën, *Foods* **2019**, *8*, 476.
- [147] G. M. Whitesides, A. D. Stroock, *Phys Today* **2001**, *54*, 42.
- [148] B. Yilmaz, F. Yilmaz, in *Omics Technologies and Bio-Engineering*, (Eds: D. Barh, V. Azevedo), Academic Press, **2018**, 145.
- [149] A. Manz, D. J. Harrison, E. M. J. Verpoorte, J. C. Fettinger, A. Paulus, H. Ludi, H. M. Widmer, *J Chromatogr* **1992**, *593*, 253.
- [150] F. Nito, T. Shiozaki, R. Nagura, T. Tsuji, K. Doi, C. Hosokawa, S. Kawano, *The Journal of Physical Chemistry C* **2018**, *122*, 17963.
- [151] V. Berejnov, N. Djilali, D. Sinton, *Lab Chip* **2008**, *8*, 689.
- [152] J. N. Lee, C. Park, G. M. Whitesides, *Anal Chem* **2003**, *75*, 6544.
- [153] T. C. Merkel, V. I. Bondar, K. Nagai, B. D. Freeman, I. Pinnau, *Journal of Polymer Science Part B: Polymer Physics* **2000**, *38*, 415.
- [154] R. H. W. Lam, M.-C. Kim, T. Thorsen, *Analytical Chemistry* **2009**, *81*, 5918.
- [155] E. Delamarche, A. Bernard, H. Schmid, A. Bietsch, B. Michel, H. Biebuyck, *J Am Chem Soc* **1998**, *120*, 500.
- [156] E. Delamarche, H. Schmid, B. Michel, H. Biebuyck, *Adv Mater* **1997**, *9*, 741.
- [157] M. Chau, M. Abolhasani, H. Therien-Aubin, Y. Li, Y. H. Wang, D. Velasco, E. Tumarkin, A. Ramachandran, E. Kumacheva, *Biomacromolecules* **2014**, *15*, 2419.
- [158] D. J. Sikorski, N. J. Caron, M. VanInsberghe, H. Zahn, C. J. Eaves, J. M. Piret, C. L. Hansen, *Biotechnol J* **2015**, *10*, 1546.
- [159] Z. Hesari, M. Soleimani, F. Atyabi, M. Sharifdini, S. Nadri, M. E. Warkiani, M. Zare, R. Dinarvand, *J Biomed Mater Res A* **2016**, *104*, 1534.
- [160] N. L. Jeon, S. K. W. Dertinger, D. T. Chiu, I. S. Choi, A. D. Stroock, G. M. Whitesides, *Langmuir* **2000**, *16*, 8311.
- [161] D. Vigolo, R. Rusconi, H. A. Stone, R. Piazza, *Soft Matter* **2010**, *6*, 3489.
- [162] J. V. Tyrrell, *Diffusion and heat flow in liquids*, **1961**.
- [163] C. Ludwig, *Sitz. Ber. Akad. Wiss. Wien* **20**, 539 **1859**.
- [164] E. Bouty, *J. Phys. Theor. Appl.* **1880**, *9*, 331.
- [165] J. Tyndall, *Nature* **1870**, *1*, 339.
- [166] P. A. E. Schoen, J. H. Walther, S. Arcidiacono, D. Poulikakos, P. Koumoutsakos, *Nano Lett* **2006**, *6*, 1910.
- [167] P. A. E. Schoen, J. H. Walther, D. Poulikakos, P. Koumoutsakos, *Appl Phys Lett* **2007**, *90*.
- [168] A. Barreiro, R. Rurali, E. R. Hernandez, J. Moser, T. Pichler, L. Forro, A. Bachtold, *Science* **2008**, *320*, 775.
- [169] R. Piazza, A. Parola, *J Phys-Condens Mat* **2008**, *20*.
- [170] P. S. Epstein, *Physical Review* **1924**, *23*, 710.
- [171] J. R. Brock, *Journal of Colloid Science* **1962**, *17*, 768.
- [172] W. C. Hinds, *New York* **1982**, 424.
- [173] L. Waldmann, K. Schmitt, Academic Press New York, 1966, 137.

- [174] C. Soret, *Sur l'état d'équilibre que prend, au point de vue de sa concentration, une dissolution saline primitivement homogène dont deux parties sont portées à des températures différentes*, Vol. 2, Arch. Sci. Phys. Nat., 2, pp. 48–61 **1879**.
- [175] D. Vigolo, J. G. Zhao, S. Handschin, X. B. Cao, A. J. Demello, R. Mezzenga, *Sci Rep-Uk* **2017**, 7.
- [176] L. H. Lin, X. L. Peng, M. S. Wang, L. Scarabelli, Z. M. Mao, L. M. Liz-Marzan, M. F. Becker, Y. B. Zheng, *Acs Nano* **2016**, 10, 9659.
- [177] E. E. Michaelides, *International Journal of Heat and Mass Transfer* **2015**, 81, 179.
- [178] G. McNab, A. Meisen, *Journal of Colloid and Interface Science* **1973**, 44, 339.
- [179] J. M. K. Ng, I. Gitlin, A. D. Stroock, G. M. Whitesides, *Electrophoresis* **2002**, 23, 3461.
- [180] D. J. Campbell, K. J. Beckman, C. E. Calderon, P. W. Doolan, R. M. Ottosen, A. B. Ellis, G. C. Lisensky, *J Chem Educ* **1999**, 76, 537.
- [181] J. D. Mackenzie, Q. Huang, T. Iwamoto, *Journal of Sol-Gel Science and Technology* **1996**, 7, 151.
- [182] A. Gokaltun, Y. B. A. Kang, M. L. Yarmush, O. B. Usta, A. Asatekin, *Sci Rep* **2019**, 9, 7377.
- [183] B. H. Jo, L. M. Van Lerberghe, K. M. Motsegood, D. J. Beebe, *J Microelectromech S* **2000**, 9, 76.
- [184] J. Friend, L. Yeo, *Biomicrofluidics* **2010**, 4.
- [185] C. C. Liu, D. F. Cui, H. Y. Cai, X. Chen, Z. X. Geng, *Electrophoresis* **2006**, 27, 2917.
- [186] Y. Bae, S. Jin, I. Kim, K. Y. Shin, *Journal of Nanomaterials* **2015**, 2015, 1.
- [187] S. H. Tan, N. T. Nguyen, Y. C. Chua, T. G. Kang, *Biomicrofluidics* **2010**, 4, 32204.
- [188] S. H. Tan, N. T. Nguyen, Y. C. Chua, T. G. Kang, *Biomicrofluidics* **2010**, 4.
- [189] L. J. Waters, C. V. Finch, A. K. M. M. H. Bhuiyan, K. Hemming, J. C. Mitchell, *J Pharm Anal* **2017**, 7, 338.
- [190] D. Bodas, C. Khan-Malek, *Sensor Actuat B-Chem* **2007**, 123, 368.
- [191] K. Haubert, T. Drier, D. Beebe, *Lab Chip* **2006**, 6, 1548.
- [192] E. Lepore, P. Faraldi, D. Bongini, L. Boarino, N. Pugno, *Compos Part B-Eng* **2012**, 43, 681.
- [193] L. Ereku, R. Mackay, W. Balachandran, K. Ajayi, *Sensors & Transducers* **2016**, 202, 1.
- [194] G. Maltezos, M. Johnston, A. Scherer, *Appl Phys Lett* **2005**, 87, 154105.
- [195] R. A. Taylor, G. L. Solbrekken, *IEEE Transactions on Components and Packaging Technologies* **2008**, 31, 23.
- [196] G. Min, D. M. Rowe, *Energy Conversion and Management* **2000**, 41, 163.
- [197] N. Maekawa, T. Komatsu, S. Murase, M. Tsuzaki, H. Iwamoto, H. Okada, M. Sagawa, H. Inoue, "Peltier module for commercial use", presented at *International Conference on Thermoelectrics, ICT, Proceedings*, **1998**.
- [198] Y. G. Gurevich, J. Velazquez-Perez, *Wiley Encyclopedia of Electrical and Electronics Engineering* **1999**, 1.
- [199] G. Binnig, H. Rohrer, *Helv Phys Acta* **1982**, 55, 726.
- [200] G. Binnig, C. F. Quate, C. Gerber, *Phys Rev Lett* **1986**, 56, 930.
- [201] Y. Martin, C. C. Williams, H. K. Wickramasinghe, *J Appl Phys* **1987**, 61, 4723.
- [202] D. Anselmetti, R. Luthi, E. Meyer, T. Richmond, M. Dreier, J. E. Frommer, H. J. Guntherodt, *Nanotechnology* **1994**, 5, 87.
- [203] G. Reiter, G. Castelein, P. Hoerner, G. Riess, J. U. Sommer, G. Floudas, *Eur Phys J E* **2000**, 2, 319.
- [204] F. J. Giessibl, *Science* **1995**, 267, 68.
- [205] Y. Sugawara, M. Ohta, H. Ueyama, S. Morita, *Science* **1995**, 270, 1646.

- [206] T. R. Albrecht, P. Grutter, D. Horne, D. Rugar, *J Appl Phys* **1991**, *69*, 668.
- [207] Q. Zhong, D. Inniss, K. Kjoller, V. B. Elings, *Surf Sci* **1993**, *290*, L688.
- [208] C. Zeng, C. Vitale-Sullivan, X. Ma, *Minerals* **2017**, *7*, 158.
- [209] S. A. C. Gould, B. Drake, C. B. Prater, A. L. Weisenhorn, S. Manne, G. L. Kelderman, H. J. Butt, H. Hansma, P. K. Hansma, S. Magonov, H. J. Cantow, *Ultramicroscopy* **1990**, *33*, 93.
- [210] P. J. Eaton, P. West, *Atomic force microscopy*, **2010**.
- [211] E. Meyer, *Progress in Surface Science* **1992**, *41*, 3.
- [212] A. Weisenhorn, P. Hansma, T. Albrecht, C. Quate, *Appl Phys Lett* **1989**, *54*, 2651.
- [213] J. H. Hoh, J. P. Revel, P. K. Hansma, *Nanotechnology* **1991**, *2*, 119.
- [214] L. Zitzler, S. Herminghaus, F. Mugele, *Physical Review B* **2002**, *66*, 155436.
- [215] E. Ruska, *Z Phys* **1933**, *83*, 492.
- [216] D. McMullan, *Scanning* **1995**, *17*, 175.
- [217] D. McMullan, J. Thewlis, A. W. Agar, D. Gabor, M. E. Haine, H. G. Lubszynski, R. Feinberg, D. McMullan, *P I Electr Eng* **1953**, *100*, 245.
- [218] J. I. Goldstein, D. E. Newbury, P. Echlin, *Scanning electron microscopy and X-ray microanalysis*, **1981**.
- [219] K. C. A. Smith, C. W. Oatley, *Brit J Appl Phys* **1955**, *6*, 391.
- [220] M. Walock, 2012.
- [221] M. J. Adams, M. A. Mullier, J. P. K. Seville, *Powder Technol* **1994**, *78*, 5.
- [222] Y. S. Cheong, M. J. Adams, A. E. Routh, M. J. Hounslow, A. D. Salman, *Chem Eng Sci* **2005**, *60*, 4045.
- [223] A. Samimi, A. Hassanpour, A. Ghadiri, *Chem Eng Sci* **2005**, *60*, 3993.
- [224] Z. Zhang, M. A. Ferenczi, A. C. Lush, C. R. Thomas, *Appl Microbiol Biot* **1991**, *36*, 208.
- [225] Z. Zhang, M. A. Ferenczi, C. R. Thomas, *Chem Eng Sci* **1992**, *47*, 1347.
- [226] C. Shiu, Z. Zhang, C. R. Thomas, *Biotechnol Tech* **1999**, *13*, 707.
- [227] G. Sun, Z. Zhang, *J Microencapsul* **2001**, *18*, 593.
- [228] Y. Yan, Z. B. Zhang, J. R. Stokes, Q. Z. Zhou, G. H. Ma, M. J. Adams, *Powder Technol* **2009**, *192*, 122.
- [229] M. Minsky, *Scanning* **1988**, *10*, 128.
- [230] Macklin J. J., T. J. K., T. D. Harris, B. L. E., *Science* **1996**, 272.
- [231] M. Ghafoor, *Synthesis of high refractive index materials for manufacturing apochromatic lens by 3D printing*, Doctorial dissertation, Department of Physics and Mathematics, University of Eastern Finland **2017**.
- [232] C. D. Lawrence, in *Lea's Chemistry of Cement and Concrete (Fourth Edition)*, (Ed: P. C. Hewlett), Butterworth-Heinemann, Oxford **1998**, 131.
- [233] C. Strel, P. Wobrauschek, P. Kregsamer, in *Encyclopedia of Spectroscopy and Spectrometry*, (Ed: J. C. Lindon), Elsevier, Oxford **1999**, 2478.
- [234] P. A. Pella, *X-Ray Spectrometry* **1989**, *18*, 187.
- [235] M. A. Short, *X-Ray Spectrometry* **1982**, *11*, vii.
- [236] G. F. Knoll, *Journal of Radioanalytical and Nuclear Chemistry* **2000**, *243*, 125.
- [237] L. de Viguerie, V. A. Sole, P. Walter, *Anal Bioanal Chem* **2009**, 395, 2015.
- [238] R. Behling, *Modern Diagnostic X-Ray Sources: Technology, Manufacturing, Reliability*, **2015**.
- [239] D. J. Kalnicky, R. Singhvi, *J Hazard Mater* **2001**, *83*, 93.
- [240] F. De Vleeschouwer, V. Renson, P. Claeys, K. Nys, R. Bindler, *Geoarchaeology* **2011**, *26*, 440.

- [241] S. Gorodzha, T. E. L. Douglas, S. K. Samal, R. Detsch, K. Cholewa-Kowalska, K. Braeckmans, A. R. Boccaccini, A. G. Skirtach, V. Weinhardt, T. Baumbach, M. A. Surmeneva, R. A. Surmenev, *J Biomed Mater Res A* **2016**, *104*, 1194.
- [242] E. Mornet, E. Stura, A. S. Lia-Baldini, T. Stigbrand, A. Menez, M. H. Le Du, *J Biol Chem* **2001**, *276*, 31171.
- [243] M. H. Le Du, T. Stigbrand, M. J. Taussig, A. Menez, E. A. Stura, *J Biol Chem* **2001**, *276*, 9158.
- [244] A. Mata, A. J. Fleischman, S. Roy, *Biomed Microdevices* **2005**, *7*, 281.
- [245] P. Linderholm, P. Åsberg, Project Report **2000**.
- [246] D. Vigolo, S. N. Ramakrishna, A. J. deMello, *Sci Rep-Uk* **2019**, *9*.
- [247] "GELRITE® Gellan Gum For Microbiological Applications™", can be found under https://www.carlroth.com/downloads/ba/en/0/BA_0039_EN.pdf, **2007**.
- [248] E. Amici, G. Tetradis-Meris, C. P. de Torres, F. Jousse, *Food Hydrocolloid* **2008**, *22*, 97.
- [249] R. Russo, M. Malinconico, G. Santagata, *Biomacromolecules* **2007**, *8*, 3193.
- [250] A. D. Cook, J. S. Hrkach, N. N. Gao, I. M. Johnson, U. B. Pajvani, S. M. Cannizzaro, R. Langer, *J Biomed Mater Res* **1997**, *35*, 513.
- [251] D. A. Haydon, *Biochimica Et Biophysica Acta* **1961**, *50*, 450.
- [252] W. D. Zhang, P. Soman, K. Meggs, X. Qu, S. C. Chen, *Adv Funct Mater* **2013**, *23*, 3226.
- [253] D. L. Vawter, *Journal of Biomechanical Engineering* **1983**, *105*, 194.
- [254] K. L. Johnson, *Contact Mechanics*, Cambridge University Press, Cambridge **1985**.
- [255] M. T. Huber, *Ann Phys-Berlin* **1904**, *14*, 153.
- [256] H. Hertz, *Verhandlungen des Vereins zur Beförderung des Gewerbefleisses* **1882**.
- [257] D. C. Lin, E. K. Dimitriadis, F. Horkay, *J Biomech Eng-T Asme* **2007**, *129*, 430.
- [258] J. Fricke, A. Emmerling, in *Chemistry, Spectroscopy and Applications of Sol-Gel Glasses*, (Eds: R. Reisfeld, C. K. Jørgensen), Springer Berlin Heidelberg, Berlin, Heidelberg **1992**, 37.
- [259] T. Yamamoto, T. Nishimura, T. Suzuki, H. Tamon, *J Non-Cryst Solids* **2001**, *288*, 46.
- [260] L. Hu, R. He, Z. Lu, K. Zhang, X. Bai, *RSC Advances* **2019**, *9*, 9931.
- [261] T. Błaszczyszki, A. Ślosarczyk, M. Morawski, *Procedia Engineering* **2013**, *57*, 200.
- [262] P. Sarawade, J. Kim, J.-K. Park, H.-K. Kim, *Aerosol and Air Quality Research* **2006**, *6*.
- [263] H.-a. Kodama, Y. Amagai, H. Sudo, S. Kasai, S. Yamamoto, *Japanese Journal of Oral Biology* **1981**, *23*, 899.
- [264] W. Kühne, *Febs Lett* **1976**, *62*, E8.
- [265] C. M. ChangLiu, G. E. Woloschak, *Cancer Lett* **1997**, *113*, 77.
- [266] K. P. Chennazhy, L. K. Krishnan, *Biomaterials* **2005**, *26*, 5658.
- [267] M. J. BriskeAnderson, J. W. Finley, S. M. Newman, *P Soc Exp Biol Med* **1997**, *214*, 248.
- [268] H. S. Yu, T. J. Cook, P. J. Sinko, *Pharmaceut Res* **1997**, *14*, 757.
- [269] W. Jin, C. J. Penington, S. W. Mccue, M. J. Simpson, *Plos One* **2017**, *12*.
- [270] "MC3T3-E1 Subclone 4 ATCC ® CRL-2593™ Mus musculus bone/calv", can be found under http://www.lgcstandards-atcc.org/products/all/CRL-2593.aspx?geo_country=gb, **2019**.
- [271] M. Absher, in *Tissue Culture*, (Eds: P. F. Kruse, M. K. Patterson), Academic Press, **1973**, 395.
- [272] A. Bejan, *Convection Heat Transfer: Fourth Edition*, **2013**.
- [273] D. Vigolo, G. Brambilla, R. Piazza, *Phys Rev E* **2007**, *75*, 040401.

- [274] E. Gomaa, *Science and Technology* **2012**, *2*, 51.
- [275] C. Zhao, J. Fu, A. Oztekin, X. Cheng, *J Nanopart Res* **2014**, *16*, 2625.
- [276] I. Machida-Sano, M. Hirakawa, H. Matsumoto, M. Kamada, S. Ogawa, N. Satoh, H. Namiki, *Biomed Mater* **2014**, *9*, 025007.
- [277] K. Nishinari, *Physical chemistry and industrial application of gellan gum, Vol. 114*, Springer, **2003**.
- [278] I. Gadjanski, *F1000Res* **2017**, *6*.
- [279] J. N. Agar, C. Y. Mou, J. L. Lin, *J Phys Chem-Us* **1989**, *93*, 2079.
- [280] V. M. Gun'ko, I. N. Savina, S. V. Mikhalovsky, *Gels* **2017**, *3*, 37.
- [281] Z. D. Shao, X. Y. He, Z. W. Niu, T. Huang, X. Cheng, Y. Zhang, *Mater Chem Phys* **2015**, *162*, 346.
- [282] J. Nemoto, T. Saito, A. Isogai, *Acs Appl Mater Inter* **2015**, *7*, 19809.
- [283] M. J. Vanbommel, A. B. Dehaan, *J Non-Cryst Solids* **1995**, *186*, 78.
- [284] C. Simon-Herrero, S. Caminero-Huertas, A. Romero, J. L. Valverde, L. Sanchez-Silva, *J Mater Sci* **2016**, *51*, 8977.
- [285] K. Tajiri, K. Igarashi, T. Nishio, *J Non-Cryst Solids* **1995**, *186*, 83.
- [286] S. Boral, A. N. Gupta, H. B. Bohidar, *Int J Biol Macromol* **2006**, *39*, 240.
- [287] M. Cassanelli, I. Norton, T. Mills, *Food Struct-Neth* **2017**, *14*, 112.
- [288] Y. Shen, G. Nystrom, R. Mezzenga, *Adv Funct Mater* **2017**, *27*.
- [289] R. Piazza, *Soft Matter* **2008**, *4*, 1740.
- [290] D. F. Coutinho, S. V. Sant, H. Shin, J. T. Oliveira, M. E. Gomes, N. M. Neves, A. Khademhosseini, R. L. Reis, *Biomaterials* **2010**, *31*, 7494.
- [291] M. Cassanelli, V. Prosapio, I. Norton, T. Mills, *Food Bioprocess Tech* **2019**, *12*, 313.
- [292] L. R. Smith, S. Cho, D. E. Discher, *Physiology* **2018**, *33*, 16.
- [293] R. J. Pelham, Jr., Y. Wang, *Proc Natl Acad Sci U S A* **1997**, *94*, 13661.
- [294] M. Sun, G. Chi, P. Li, S. Lv, J. Xu, Z. Xu, Y. Xia, Y. Tan, J. Xu, L. Li, Y. Li, *Int J Med Sci* **2018**, *15*, 257.
- [295] Q. Y. Zhang, Y. Yu, H. C. Zhao, *Acta Bioch Bioph Sin* **2016**, *48*, 958.
- [296] C. A. Mullen, M. G. Haugh, M. B. Schaffler, R. J. Majeska, L. M. McNamara, *J Mech Behav Biomed* **2013**, *28*, 183.
- [297] B. Alberts, A. Johnson, J. Lewis, M. Raff, K. Roberts, P. Walter, in *Molecular Biology of the Cell. 4th edition*, Garland Science, **2002**.
- [298] M. F. Pittenger, A. M. Mackay, S. C. Beck, R. K. Jaiswal, R. Douglas, J. D. Mosca, M. A. Moorman, D. W. Simonetti, S. Craig, D. R. Marshak, *Science* **1999**, *284*, 143.
- [299] J. Caetano-Lopes, H. Canhao, J. E. Fonseca, *Acta Reumatol Port* **2007**, *32*, 103.
- [300] Z. Dai, J. Ronholm, Y. P. Tian, B. Sethi, X. D. Cao, *Journal of Tissue Engineering* **2016**, *7*.
- [301] C. Fischbach, J. Tessmar, A. Lucke, E. Schnell, G. Schmeer, T. Blunk, A. Göpferich, *Surf Sci* **2001**, *491*, 333.
- [302] H. Shearer, M. J. Ellis, S. P. Perera, J. B. Chaudhuri, *Tissue Eng* **2006**, *12*, 2717.
- [303] Y. Ali, M. Dolan, E. Fendler, E. Larson, Lippincott Williams & Wilkins: Philadelphia, PA, USA, 2001.
- [304] S. Gogolewski, P. MainilVarlet, *Biomaterials* **1996**, *17*, 523.
- [305] D. Yixiang, T. Yong, S. Liao, C. K. Chan, S. Ramakrishna, *Tissue Engineering Part A* **2008**, *14*, 1321.
- [306] Z. Yang, H.-R. Xiong, *Biomedical Tissue Culture* **2012**, *1*, 3.
- [307] E. J. Robertson, E. J. Robertson, *Teratocarcinomas and embryonic stem cells : a practical approach*, **1987**.
- [308] R. Begbie, *Biochimica et Biophysica Acta (BBA)-Protein Structure* **1974**, *371*, 549.

- [309] M. A. Wozniak, K. Modzelewska, L. Kwong, P. J. Keely, *Biochimica et Biophysica Acta (BBA) - Molecular Cell Research* **2004**, *1692*, 103.
- [310] S. I. Lee, Y. Ko, J. B. Park, *Exp Ther Med* **2017**, *13*, 3467.
- [311] G. S. Stein, J. B. Lian, *Endocrine Reviews* **1993**, *14*, 424.
- [312] A. Rutkovskiy, K.-O. Stensløkken, I. J. Vaage, *Med Sci Monit Basic Res* **2016**, *22*, 95.
- [313] H. Hanna, L. M. Mir, F. M. Andre, *Stem Cell Res Ther* **2018**, *9*, 203.
- [314] R. Jenkins, *X-ray fluorescence spectrometry, Vol. 2*, Wiley New York, **1999**.
- [315] R. Olivares-Navarrete, A. L. Raines, S. L. Hyzy, J. H. Park, D. L. Hutton, D. L. Cochran, B. D. Boyan, Z. Schwartz, *Journal of bone and mineral research : the official journal of the American Society for Bone and Mineral Research* **2012**, *27*, 1773.
- [316] J. Ng, J. Bernhard, G. Vunjak-Novakovic, *Methods Mol Biol* **2016**, *1416*, 35.
- [317] S. Shahab-Osterloh, F. Witte, A. Hoffmann, A. Winkel, S. Laggies, B. Neumann, V. Seiffart, W. Lindenmaier, A. D. Gruber, J. Ringe, T. Haupl, F. Thorey, E. Willbold, P. Corbeau, G. Gross, *Stem Cells* **2010**, *28*, 1590.
- [318] L. Cen, W. Liu, L. Cui, W. Zhang, Y. Cao, *Pediatr Res* **2008**, *63*, 492.
- [319] L. Ma, C. Gao, Z. Mao, J. Zhou, J. Shen, X. Hu, C. Han, *Biomaterials* **2003**, *24*, 4833.
- [320] K. S. Rho, L. Jeong, G. Lee, B. M. Seo, Y. J. Park, S. D. Hong, S. Roh, J. J. Cho, W. H. Park, B. M. Min, *Biomaterials* **2006**, *27*, 1452.
- [321] T. Matsumoto, K. Hattori, A. Matsushima, M. Tadokoro, T. Yagyuu, M. Kodama, J. Sato, H. Ohgushi, *Tissue Eng Part A* **2011**, *17*, 171.
- [322] S. R. Caliarì, B. A. C. Harley, *Adv Healthc Mater* **2014**, *3*, 1086.
- [323] K. Yue, G. Trujillo-de Santiago, M. M. Alvarez, A. Tamayol, N. Annabi, A. Khademhosseini, *Biomaterials* **2015**, *73*, 254.
- [324] G. Gao, A. F. Schilling, K. Hubbell, T. Yonezawa, D. Truong, Y. Hong, G. Dai, X. Cui, *Biotechnology Letters* **2015**, *37*, 2349.
- [325] W. Dai, S. L. Hale, G. L. Kay, A. J. Jyrala, R. A. Kloner, *Regenerative medicine* **2009**, *4*, 387.